Liquid Crystal Networks for Smart Biomimetic Micro/Nano Structured Adhesives

by

Hamed Shahsavan

A thesis

presented to the University of Waterloo

in fulfillment of the

thesis requirement for the degree of

Doctor of Philosophy

in

Chemical Engineering (Nanotechnology)

Waterloo, Ontario, Canada, 2017

Examining Committee Membership

The following served on the Examining Committee for this thesis. The decision of the Examining Committee is by majority vote.

External Examiner   Prof. Benjamin D. Hatton
                     Materials Science & Engineering, University of Toronto

Supervisor   Prof. Boxin Zhao
                     Chemical Engineering, University of Waterloo

Internal Member   Prof. Mark W. Matsen
                     Chemical Engineering, University of Waterloo

Internal Member   Prof. Nasser M. Abukhdeir
                     Chemical Engineering, University of Waterloo

Internal-external Member   Prof. Bo Cui
                            Electrical and Computer Engineering, University of Waterloo

Author's Declaration

This thesis consists of material all of which I authored or co-authored: see Statement of Contributions included in the thesis. This is a true copy of the thesis, including any required final revisions, as accepted by my examiners.

I understand that my thesis may be made electronically available to the public.

Statement of Contributions

This dissertation is directly related to some of my work that I published during my PhD studies. Chapter 3 of this dissertation is partially reproduced from:

- <u>Hamed Shahsavan</u> and Boxin Zhao, "Bioinspired Functionally Graded Adhesive Materials: Synergetic Interplay of Top Viscous–Elastic Layers with Base Micropillars", *Macromolecules*, 47, no. 1 (2014), 353-364. (DOI: 10.1021/ma4018718)

Chapter 4 of this dissertation is partially reproduced from:

- <u>Hamed Shahsavan</u>, Seyyed Muhammad Salili, Antal Jákli, and Boxin Zhao, "Smart Muscle-Driven Self-Cleaning of Biomimetic Microstructures from Liquid Crystal Elastomers", *Advanced Materials*, 27, no. 43 (2015), 6828-6833. (DOI:10.1002/adma.201503203)

Chapter 5 of this dissertation is partially reproduced from:

- <u>Hamed Shahsavan</u>, Seyyed Muhammad Salili, Antal Jákli, and Boxin Zhao, "Thermally Active Liquid Crystal Network Gripper Mimicking the Self-Peeling of Gecko Toe Pads", *Advanced Materials,* 29, no. 3 (2017), 1604021. (DOI:10.1002/adma.201604021)

I had the major contribution in designing and performing experiments, collecting experimental data and analyzing them in all three papers. I wrote all papers.

Abstract

As modern technology demands for miniaturized structures with higher surface area to the volume ratio, the design and synthesis of materials with tailored surfaces is becoming more important. Moreover, some emerging technologies require materials with smart surface properties that can be controlled remotely, and work adaptively in "on" and "off" states when stimulated externally. Fascinating surface structures and adaptive functionalities that can be found in biological systems have provided great inspirations to researchers for fabrication of synthetic biomimetic assemblies. While the fabrication of materials with non-smart bio-inspired surface structures has been greatly accomplished, the mimicking of adaptive functionalities of the living systems is less investigated. Thus, there is a great zeal in developing materials with smart and adaptive biomimetic structured surfaces. The objective of this dissertation is to design and develop materials with smart biomimetic micro/nanostructured surfaces that can show desirable responses when remotely stimulated.

First, an experimental study on the integration of a dissipative material (resembling the dissipative and wet nature of the tree frog toe pads) to an elastic fibrillar interface (resembling the dry and fibrillar nature of the gecko foot pads) is carried out. Accordingly, a new type of functionally graded adhesive is developed, which is composed of an array of elastic micropillars at the base, a thin elastic intermediate layer and a viscoelastic top layer. The results showed that the new proposed graded structure has remarkable adhesive properties in terms of pull-off force, work of adhesion, and structural integrity (i.e., inhibited cohesive failure). Second, muscle-driven actuation of biomimetic microfibrillar structures is achieved using integrative soft-lithography on a backing splayed liquid crystal elastomer or networks (LCEs/LCNs). Variation in the backing LCE layer thickness yields different modes of thermal deformation from a pure bend to a twist-bend. The muscular motion and dynamic self-cleaning of gecko toe pads are mimicked via this mechanism. Finally, the self-peeling of gecko toes is mimicked by the integration of film-terminated fibrillar adhesives to hybrid nematic LCN cantilevers. A soft gripper is developed based on the gecko-inspired attachment/detachment mechanism. Performance of the fabricated gripper for transportation of thin delicate objects is evaluated by the optimum mechanical strength of the LCN and the maximum size of the adhesive patch.

Acknowledgements

I would like to express my gratitude to my research supervisor, Professor Boxin Zhao, for his persistent inspiration, guidance, and support. On the one hand, his honest, kind, and flexible personality allowed me to work without any tension and learn without constraint. On the other hand, his disciplined working style and elucidatory advices taught me professional working attitude. I would like to thank him for giving me the opportunity to work on a multidisciplinary and cutting-edge research project, which is crucial for my career endeavors.

I would like to thank Professor Antal Jákli for the opportunity to work in his laboratory at Kent State University and providing many experimental instruments. He taught me precious concepts and broadened my insights about the field of liquid crystals. I learned a lot from his joyful personality, brilliant scientific ideas and meticulous views and inputs at every step of my research.

I cordially thank my friends Dr. Mohammad Javad Shafiee, Dr. Mohammad Mohammadi and Dr. Kaveh Sarikhani. With their presence, I never felt alone neither in sadness nor in joy.

Finally, I would like to thank all my lab mates and colleagues in Waterloo and Kent for their help, useful suggestions, and cheer during the period I was working with them. Particularly, I greatly appreciate helps by Dr. Seyyed Muhammad Salili and Mr. Kelvin Liew during my PhD period.

Dedication

I dedicate this dissertation to my family for their endless love, patience, and care.

Table of Contents

List of Figures

xiii

List of Tables

List of Nomenclatures

γ	Surface free energy		κ	Curvature
E	Free energy		S_d	Distortional strain
W	Work of adhesion		λ	Wavelength of the light
θ	Contact angle		$\overline{W}$	Output energy density
F	Pull-off (adhesion) force		ε	Strain
R_i	Radius of probe and substrates in an indentation test		E_b	Bending energy
ρ	Roughness factor		μ'	Adhesion coefficient
f	Surface ratio		p	Maxwell stress
a	Contact radius		ϵ	Dielectric permittivity
K	Reduced Young's modulus		$|\vec{E}|$	Intensity of the electrical field
σ	Poisson ratio		C	Compliance
Y	Young's modulus			
δ	Displacement			
$\mathcal{G}, \mathcal{G}_0$	Overall and critical energy release rate			
φ	Energy dissipation factor			
υ	Crack propagation rate			
$n, \Delta n$	Refractive index and birefringence of a material			
Q	Order parameter			
ϑ	Tilt angle of the mesogens from director			
T_g	Glass transition temperature			
R_g	Radius of gyration			
T_{NI}, T_K	Clearing and crystallization temperatures			
G	Shear modulus			
t^*	Relaxation time			
U	Adhesion hysteresis			
δ_{max}	Displacement at preload			
A	Contact area			
S	Stiffness			

Chapter 1
Introduction

Recent progress in micro/nanotechnology has created experimental platforms and materials with higher surface to volume ratio. As a result, the role of surfaces and interfaces in both science and technology is becoming progressively important. Adhesion of materials is one of their key surface properties. Therefore, the understanding and manipulation of adhesion is a pivotal task for the development and manufacturing of advanced materials at smaller scales. Particularly, functional adhesive systems, i.e. adhesives with both desired adhesion strength and structural integrity, which can serve desired purposes in different environmental conditions are becoming integral in such emerging technologies as biomedical, energy, electronic, and optical devices. On the other hand, some technologies require "smart" adhesives. So-called "smart" adhesives are adhesives which their properties can be controlled remotely when stimulated externally by electrical, magnetic, thermal, and chemical cues and so forth. Ideally, these adhesives can reversibly bond ("on" state) and de-bond ("off" state) from an adherent upon exposure to a certain external stimulating input. For instance, besides permanent structural adhesive bonding, smart functional adhesive materials are in high demand for many applications such as consumer products, medical bandage and the assembly, packaging, and transportation of delicate electronic components and devices [1].

A plethora of biological systems have fascinating micro/nanostructures on their skin giving them functional adhesive properties that can be mimicked to develop novel synthetic systems with tailored adhesion and surface topography. The locomotive organs of geckos and tree frogs are outstanding examples of such functional biological adhesive systems. While hair-like structure of the gecko toes and micro-textured surface of the tree frog toes generate strong attachment force to mating surfaces, the muscle-driven back-scrolling motion of their toes facilitates detachment in a self-peeling mechanism [2]. Accordingly, these animals can attach and detach their toes repeatedly by countless switching them between adhesive, "on", and non-adhesive, "off", states. This amazing aptitude of these creatures has attracted extensive research interests for development and application of the biomimetic structures [1]. During the last two decades, biomimicry has greatly accomplished fabrication of the biomimetic structures and manipulation of their surface properties. While much desired, mimicking the switchable functionalities of these living adhesive systems is less investigated. Thus, there is great potential

in the development of materials with functional biomimetic structured adhesives that can work adaptively in a smart fashion to switch the adhesion "on" or "off" as needed.

The fabrication of biomimetic patterned adhesives acting in "on" and "off" states still remains a challenge. Herein, the aim is to integrate biomimetic structures with known responsive materials in order to induce the smartness of switchable adhesion. Among all candidates such as conductive polymers, hydrogels, piezoelectric ceramics and others, liquid crystalline (LC) materials are chosen. LCs undergo different conformational and phase changes upon exposure to different external stimuli such as temperature, light, concentration, electrical and magnetic fields [3–10]. In contrast to the low molecular weight LCs that are frequently used in display and optics technologies, LC polymers (LCP), elastomers (LCE) and networks (LCN) have not been exploited to the same degree. The elasticity and contractility of LCEs and LCNs make them attractive candidates as active materials for artificial muscles that can be used in a variety of technologies. Besides, there is great potential for these materials as their incorporation into biomimetic micro/nano-structures is an emerging field of study with very few published reports in literature [11–17].

The overall objectives of this project are to study, design, and fabricate smart and functional biomimetic structured surfaces based on LCEs and LCNs which are capable of a desired response to external stimulation. These structures are aimed to deliver desirable properties such as self-cleaning and switchable adhesion and will be used in certain applications such as transportation of 2D fragile light objects. As can be seen in the Figure 1-1, three key steps were identified at the beginning of this project to achieve the project objectives:

1) Design and fabrication of biomimetic structured surfaces with functional adhesive properties

2) Fabrication of biomimetic micro-textured LCEs/LCNs with dynamic self-cleaning properties

3) Integration of the biomimetic functional adhesives to LCEs/LCNs cantilevers and development of gecko-inspired grippers

The content of this dissertation is arranged in six chapters. Aside from the current chapter, a brief background and literature review on biological and biomimetic adhesive systems, and responsive liquid crystal networks is presented in *chapter two*. In *chapter three*, inspired by the amazing adhesion abilities of the toe pads of geckos and tree frogs, we report an experimental

2

study on the integration of a dissipative material (resembling the dissipative and wet nature of the tree frog toe pads) to an elastic fibrillar interface (resembling the dry and fibrillar nature of the gecko foot pads). Accordingly, a new type of functionally graded adhesive is introduced, which is composed of an array of elastic micropillars at the base, a thin elastic intermediate layer and a viscoelastic top layer. A systematic investigation of this bioinspired graded adhesive structure was performed. The results showed that this graded structure has remarkable adhesive properties in terms of pull-off force, work of adhesion, and structural integrity (i.e., inhibited cohesive failure)[1]. In *chapter four*, muscle-driven actuation of biomimetic microfibrillar structures is achieved using integrative soft-lithography on a backing splayed liquid crystal elastomer (LCE). Variation in the backing LCE layer thickness yields different modes of thermal deformation from a pure bend to a twist-bend. Muscular motion and dynamic self-cleaning of gecko toe pads are mimicked via this mechanism [18]. In *chapter five*, self-peeling of gecko toes is mimicked by integration of film-terminated fibrillar adhesives to hybrid nematic liquid crystal network (LCN) cantilevers. A soft gripper is developed based on the gecko-inspired attachment/detachment mechanism. Performance of the fabricated gripper for transportation of thin delicate objects is evaluated by the optimum mechanical strength of the LCN and the maximum size of the adhesive patch [19]. Concluding remarks, current challenges for further development and future potential solutions are provided in *chapter six*.
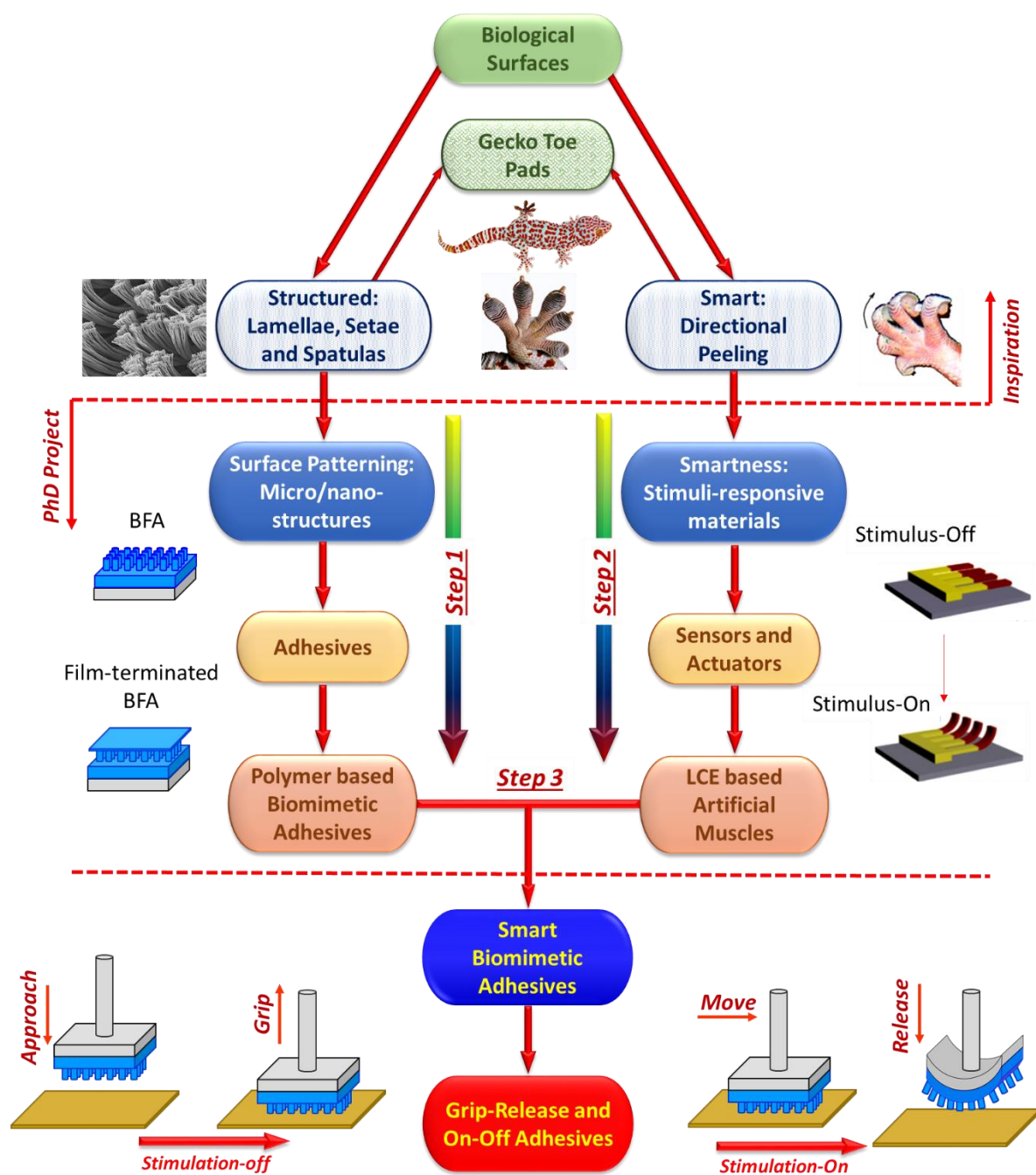
Figure 1-1. Key steps to achieve the research project objectives as illustrated in the original proposal. (BFA: Biomimetic Fibrillar Adhesive, LCE: Liquid Crystal Elastomer)

Chapter 2
Literature Review and Background

2.1 Adhesion, Biological and Biomimetic Adhesive Systems

2.1.1 Principles of adhesion and wetting

2.1.1.1 Ideal contacts

Ideality of the contact between a liquid and a solid or two solid materials necessitates perfect smoothness, extreme rigidity, incompressibility, and chemical homogeneity of the solid surface. There are several common terms that have been used to describe the contact between materials including, surface free energy, surface tension, interfacial energy, and work of adhesion. Surface free energy is the energy required to create a unit area of surface of a material ($\gamma_i = \frac{\partial E}{\partial A}$) with the dimensional unit of J/m². The term surface tension is commonly used for liquids with the unit of N/m. Interfacial energy, γ_{ij} is defined as the change in the free energy of a system when two materials are brought into contact and create a unit area of interface. The work required to rupture this interface and separate the two materials in the vacuum or air is called the work of adhesion (W_{ij}^A). The relationship between the work of adhesion, surface free energy, and interfacial energy is given by the Dupre equation [20,21]:

$$W_{ij}^A = \gamma_i + \gamma_j - \gamma_{ij} \qquad \text{2-1}$$

The energy required to break apart a unit area of a single material is defined as the work of cohesion ($W_{ii}^C = 2\gamma_i$). For a system with a solid and a liquid in contact and within a third medium e.g. gas, vapor, or vacuum (denoted by subscript v), Young's theory is typically used to quantify the equilibrium state by relating the surface/interfacial tensions to the contact angle as:

$$\gamma_{sv} = \gamma_{sl} + \gamma_{lv}\,cos\theta \qquad \text{2-2}$$

where γ_{sv} and γ_{lv} represent free energy of the solid and the liquid in vacuum, respectively; and γ_{sl} is the interfacial energy of the solid/liquid interface (Figure 2-1) [22].
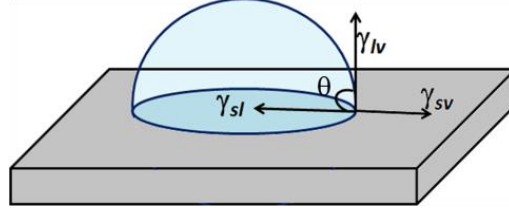
Figure 2-1. Schematic of three phase contact line for a liquid drop on a solid surface in vapor medium

Dupre equation can be related to Young's equation as follow:

$$W_{sl}^A = \gamma_{lv}(1 + cos\theta) \qquad \qquad 2\text{-}3$$

The above mentioned equations are valid for ideal contact between materials and they lead to a single, unique contact angle [20,23].

The solid/solid contact can also be used to determine the work of adhesion and free energy of the materials by measuring the adhesion force required to pull off the adhered surfaces. For this, the Derjaguin approximation for the contact between two *microscopic* spherical particles, solid 1 and solid 2, could be used to relate the adhesion force $F_{pull-off}$ to the work of adhesion between two ideally rigid (incompressible), smooth, and homogeneous spherical solids as [23]:

$$F_{pull-off} = 2\pi \left(\frac{R_1 R_2}{R_1 + R_2} \right) W^A{}_{12} \qquad \qquad 2\text{-}4$$

where R_1 and R_2 are the radii of two non-identical spherical particles, and R is the radius of two identical spheres in contact where $R = R_1 = R_2$ and $W^A{}_{12} = 2\gamma_{sv}$.

2.1.1.2 Non-ideal contacts

In reality, interfacial events are irreversible, especially for the solids, which often include unfavorable energy dissipation processes [23]. Thus, the equations mentioned in the previous section need modifications. For liquid/solid contact, the measured contact angle of the liquid is often different from the value that is derived from the thermodynamic correlations of Young's theory [20]. There are two well-known models to account for the observed contact angle of a liquid in a non-ideal contact with a solid (Figure 2-2). The first model is based on a work done by Wenzel which assumes an intimate contact between the liquid and solid [21]:

$$cos\,\theta^W = \rho\,cos\,\theta \qquad \qquad 2\text{-}5$$

where θ^W is the Wenzel equilibrium contact angle and θ is the intrinsic contact angle or Young's contact angle. ρ is the roughness factor defined as the ratio of the real contact area to the apparent contact area and it is always larger than one ($\rho > 1$) [24]. The second model is Cassie and Baxter model which is based on a non-conformal contact between a liquid and a solid and it predicts the equilibrium contact angle θ^{CB} of a liquid on heterogeneous solid surfaces [25,26].

$$cos\,\theta^{CB} = \sum_i f_i \cos \theta_i \qquad \qquad 2\text{-}6$$

f_i is the area fraction of a portion with a certain surface free energy to the whole surface area. θ_i is the intrinsic equilibrium contact angle corresponding to each portion.
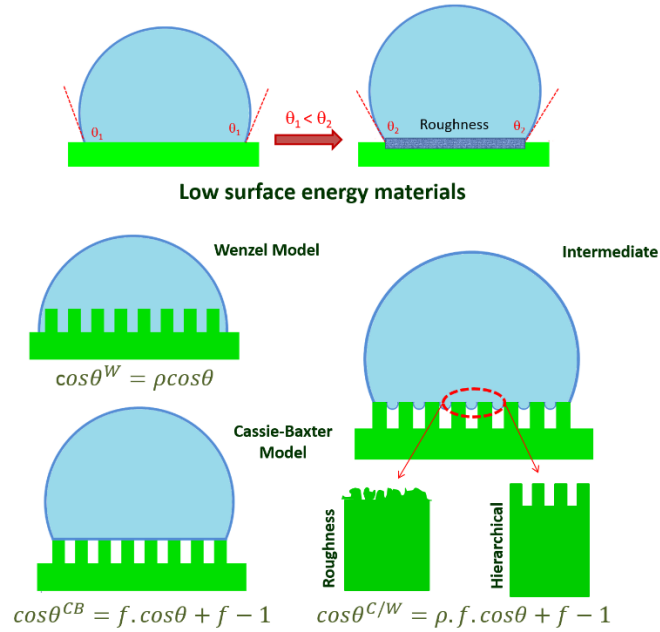
Figure 2-2. Deviation of the apparent contact area from the actual value through surface roughness, Wenzel and Cassie-Baxter models of the contact angle, and transient state of the contact angle

There are some complex conditions related to chemically heterogeneous and rough, and fractal rough materials. In such cases, the mode of contact of liquid with the mating solid could not be considered either conformal or non-conformal. The combination of Wenzel and Cassie-Baxter models has been proposed to predict the equilibrium contact angle $\theta^{C/W}$ of the liquid on such surfaces [26]:

$$cos\,\theta^{C/w} = \rho(f_1 \cos \theta_1 - f_2) \qquad \qquad 2\text{-}7$$

f_1 and f_2 are the area fraction of the air and solid surface. It is worth noting that hysteresis is common in the measurement of contact angles; measured advancing contact angle θ_A is often larger than receding contact angle θ_R [23,27]. Similar to the liquid/solid contact, the interfacial energy and the adhesion of solid/solid contacts are also affected by hysteresis [28,29].

Contact mechanics models usually describe the behavior of contact between solids. Hertz model is the oldest contact mechanics model describing the contact between two rigid and perfectly smooth solids. It is based on the correlation between the area of the Newton rings and the applied normal force, i.e. preload, observed during approaching of two glass lenses [27,30–32]:

$$F = \frac{Ka^3}{R'}$$
2-8

, where F is the applied load on the spheres, a is the radius of contact area, and R' is the combined radius of two spheres defined as: $R' = R_1 R_2/(R_1 + R_2)$. K is the reduced Young's modulus of two solid bodies with Young's modulus Y and Poisson ratio of σ and defined as:

$$\frac{1}{K} = \frac{3}{4}\left[\left(\frac{1 - \sigma_1^2}{Y_1}\right) + \left(\frac{1 - \sigma_2^2}{Y_2}\right)\right]$$
2-9

Hertz, however, does not consider the effect of intermolecular interactions on the surface of two solids and only accounts for compressive forces. The Hertz model assumes that loading and unloading of the solids experiences no hysteresis. The most important contribution of this theory, however, was the acknowledgement that even extremely rigid solids will experience deformation when in contact, which is not in agreement with the ideality of contact. As a result, the vertical elastic deformation δ and the contact area can be correlated as $\delta = \frac{a^2}{R'}$.

According to Derjaguin, the Hertz model is insufficient even in zero normal loads, as solid materials in the proximity of contact experience deformation. Thus, in the DMT (Derjaguin-Muller-Toporov) model, the influence of intermolecular interactions in deformation of rigid bodies in contact under zero load has been taken into account; and the Hertz equation is modified to:

$$F = \frac{Ka^3}{R'} - 2\pi R' W_{12}^A$$
2-10

where W_{12}^A is the thermodynamic work of adhesion between two solids in the vacuum under ideal conditions. Vertical deformation is related to the contact area in the same way as Hertz

theory. Short-range and intermolecular interactions are manifested in DMT theory as a tensile stress inside the contact area. This model assumes that elastic deformation does not affect the total adhesion remarkably. Adhesion hysteresis is also not considered in this theory.

Later on, Johnson, Kendall, and Roberts showed that the real contact area is practically greater than that predicted by DMT because the DMT model does not take into account the load distribution within the contact area. Resolving this issue, they developed a modified theory which involves the adhesive forces between two solids, the so-called JKR theory [31,33].

$$F = \frac{Ka^3}{R'} - \sqrt{6\pi W_{12v}^A Ka^3} \qquad\qquad 2\text{-}11$$

In the JKR theory, the vertical deformation δ and the work of adhesion between two solids are correlated as $\delta = \frac{a^2}{R'} - \frac{2}{3}\sqrt{\frac{6\pi W_{12v}^A a}{K}}$.

Deviation from the thermodynamic work of adhesion (or ideal adhesion) leads to the concept of practical adhesion, which is the experimentally determined adhesion energy. To elucidate the relationship between ideal adhesion and practical adhesion a series of adhesion and peeling experiments were implemented by Gent, Andrews, and Kinloch [34–36]. They concluded that the practical adhesion in terms of mechanical work of separation includes the ideal work of adhesion (or critical energy release rate) and the temperature and rate depended dissipative mechanisms:

$$\mathcal{g} = \mathcal{g}_0\big(1 + \varphi(T, v)\big) \qquad\qquad 2\text{-}12$$

where $\mathcal{g}$ is the energy release rate defined as the energy required for decreasing the interfacial area through crack propagation process, $\mathcal{g}_0$ is the critical release rate as crack propagation rate, v, approaches zero, and φ is energy dissipation factor [37]. In this correlation, viscoelastic dissipative mechanisms are present during the separation.

2.1.2 Biological and biomimetic adhesives

A myriad of natural surfaces, e.g. outermost organs of animals and plants, show functional adhesive properties, including both the adhesive strength and cohesive strength. The properties of such adhesive systems are usually rooted in surface topography and sometimes complex geometry of their toes skin. Anisotropic and hierarchical hair-like micro/nanostructures on the gecko feet and micro-channels of tree frog toes are famous examples of such biological

adhesive systems [38,39]. The structure of a tree frog toe pad, shown in **Figure 2-3**, is based on hexagonal arrays of epithelial cells separated by large grooves which are filled with a secreted watery mucus. The exact mechanism of adhesion of tree frogs is not fully understood, but it is believed that combination of different mechanisms contribute to the total adhesion [40]. For instance, some researchers believe that micro-scale hexagonal grooves and channels regulate the capillary forces associated with secreted liquids [41]. Some postulate that water drainage from micro-grooves during the contact regulates the adhesion in wet condition [40].
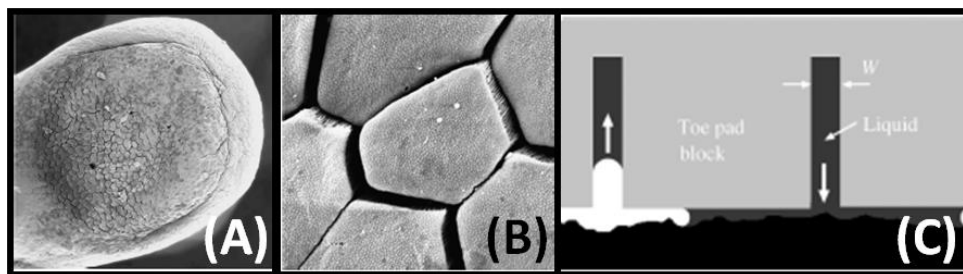
Figure 2-3: (A and B) SEM image of toe of a three frog, (C) capillarity assisted mechanism of adhesion utilized by tree frogs [38].

Gecko toe pad, shown in **Figure 2-4**, has an intricate multilevel hierarchical hair-like structure which is composed of tens of lamellar scansors that are branched to thousands of curvy and angled stalks known as setae. Every seta is further branched to numerous spatulae which are terminated by a thin triangular flap. These hierarchical micro/nanostructures on the gecko toe pads maximizes the compliance and contact area; thus gecko can utilize van der Waals and other intermolecular forces to generate sufficient adhesion to the mating surfaces [38,42–45]. Note that the surface structures of gecko toe pad are anisotropic, which facilitates gecko's locomotion (attachment and detachment) on vertical or even inverted surfaces. It was postulated that geckos can generate normal adhesion only in combination with the shear force and their attachment is along with very high coefficient of friction. Experiments by Autumn and coworkers proved this hypothesis by measuring the adhesion force of a living gecko toe and an isolated seta under different shearing conditions. It was revealed that geckos adhere to vertical and inverted surfaces by generating friction in their opposing feet. In a mechanism so-called "frictional adhesion", adhesion force increases as a function of shear force when geckos attempt to grip their toes and extremely anisotropic setae to a mating surface. In contrast, releasing takes place by gradual decreasing the normal load through peeling the toes or tilting the setal array which is dictated

by the conventional Coulomb friction mechanism, where the friction force is a function of normal load [46,47].

Theoretical calculations based on the shear and normal adhesion force of a single setae show that a normal Tokay gecko with average weight of 50gr can withstand loads up to 130Kg [45]. Considering such a large adhesion strength, it is surprising that geckos can detach their toe pads easily to walk or run. It is known that this detachment is the result of peeling of the toes toward the animal body (Figure 2-5). In fact, the gecko peels off the toes from the mating surface instead of pulling them off vertically. Hence, the hybrid nature of the toe pad, i.e. soft deformable muscle plus anisotropic surface protrusions, create a functional platform for manipulation of their adhesive system that act in "on" and "off" states. The functional adhesion system of gecko toe pads is the main inspiration behind this research project for the fabrication of a smart assembly with functional adhesion. Note that the terms smart, adaptive, and stimuli-responsive may be used interchangeably throughout this dissertation.
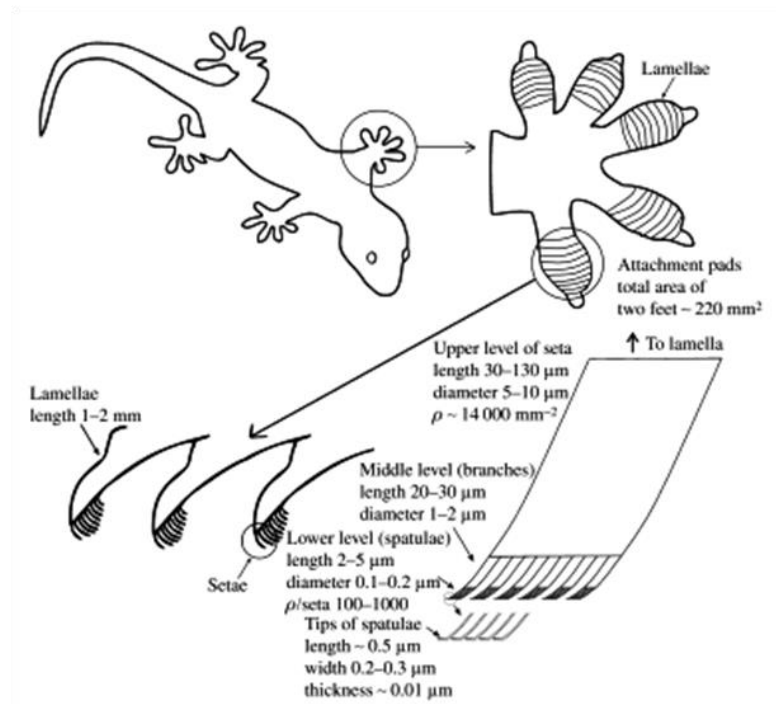
Figure 2-4: Schematic view of the gecko toe pad scaling and hierarchy [48]
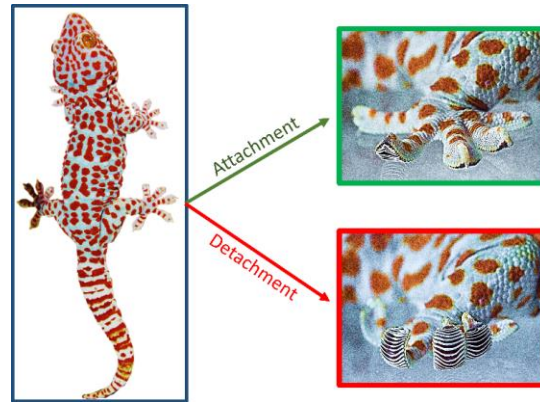
Figure 2-5. Gecko attachment-detachment cycle in which gecko maximizes the contact for attachment and rolls back the toes for detachment.

2.1.2.1 Synthetic biomimetic patterned surfaces

During the last two decades, synthetic biomimetic fibrillar adhesives with a variety of geometries and materials have been fabricated. The first class of these structures is based on simple surface protrusions such as pillars or posts [49–51], some of which have different tip shapes, e.g. mushroom-shaped pillars [46,52]. These structures have been fabricated in either single or multiple levels from nano- to micro-scales [53,54]. Another class of biomimetic structures is based on incisions underneath the free surface of a material. Film-terminated micro-fibrils [55,56], bridged micro-fibrils [57], and capped micro-fluidic channels have been fabricated in single or multiple levels of hierarchy [58] (Figure 2-6). Thus far, mushroom-shaped, film-terminated, and bridged pillars are introduced as the most effective prototypes. These synthetic structures effectively increase adhesion of a flat control by combination of different mechanisms such as contact splitting [59], enhanced compliance [60], and crack trapping [55].
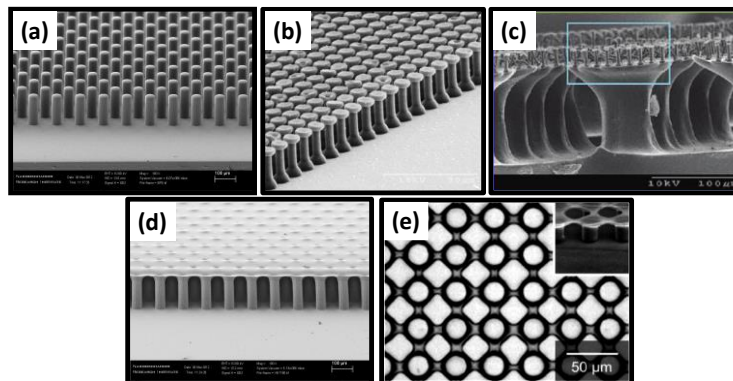
Figure 2-6. Synthetic biomimetic fibrillar adhesives with (a) simple [56], (b) mushroom-shaped [61], (c) hierarchical mushroom-shaped [53], (d) thin film-terminated [56], and (e) bridged micropillars [57]

Surface splitting theory quantitatively explicates the effective role of splitting up a contact into finer sub-contacts in overall adhesion enhancement using the basic principles of contact mechanics. This theory uses proportionality of the adhesion force to linear dimension of the contact in JKR theory ($F_{pull-off} = \frac{3}{2}\pi R'\gamma$). It suggests that splitting of a contact (with radius of R') to n sub-surfaces (setae structure in insects and animals) would increase the length over which adhesive force is defined to $R'/\sqrt{n}$. Thus, the total adhesion force would increase to $F'_{pull-off} = (R'/n).F_{pull-off}$[59,62,63]. In another mechanism, compliance of a surface and accordingly its adhesion can be increased by texturing it with fibrillar structures. In this mechanism, deformation of the fibers in different directions compensate for the surface roughness [38,41,42]. The hierarchical structure of the gecko toe pads has been modeled as a spring foundation composed of several parallel springs in one level connected in series to other levels. This arrangement is capable of reducing the spring stiffness effectively leading to higher surface adaptability [48,64–66]. As a result, adhesion enhancement is achieved through maximization of the contact area [67–69].

Crack trapping mechanism of adhesion enhancement is rooted in fracture mechanics models. In brief, the amount of energy required for crack propagation along an interface is deemed to be higher for fibrillar surfaces comparing to their non-textured smooth counterparts when they are in contact with a solid probe. During separation, the elastic energy stored in adhesive during loading is being recovered and this energy facilitates the crack propagation in a continuous fashion for smooth surfaces. However, the elastic energy stored inside the fibrils of a textured surface can facilitate the crack propagation in a non-continuous fashion. This is postulated as the spatial path for the energy transfer to crack is obstructed by inter-fibrillar space. As a result the energy will choose the further distance in the bulk of the backing material requiring more energy dissipation [68,70]. Glassmaker et al. experimentally validated the crack trapping phenomenon in thin film-terminated micropillar structures. According to their observation, the crack front is bulged and intermittently trapped between the fibrils and propagates on top of the fibrils. This phenomenon can be observed through bottom-view images of a contact during the formation (Figure 2-7) and separation along with zigzag patterns on the unloading portion of a load-displacement curve of an indentation cycle [55]. The experimental details of this mechanism is described in chapter 3 of this dissertation.
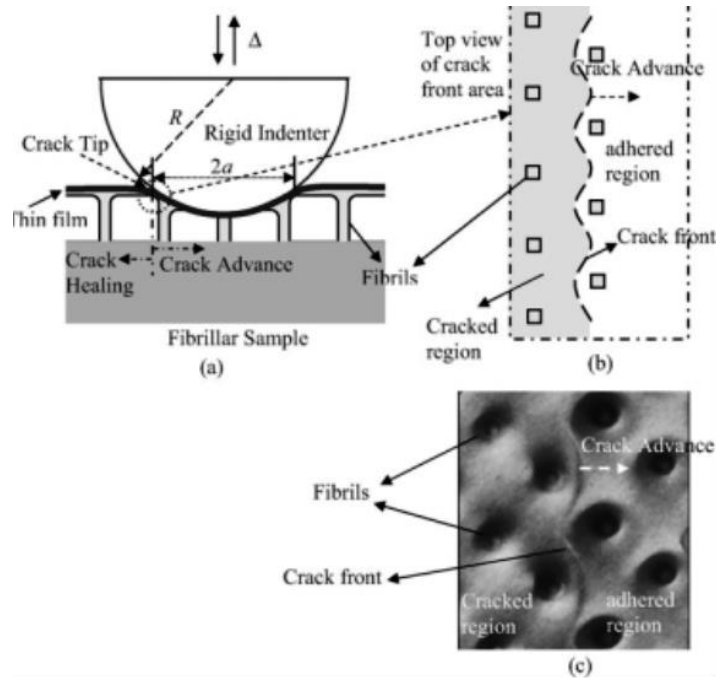
Figure 2-7: Schematics of a spherical indentation probe on a film-terminated fibrillar adhesive (a), hypothetical schematics (b) and actual view (c) of crack bulging and trapping during an indentation test reported by ref [55]

Above mentioned mechanisms are usually used to describe adhesion enhancement in fibrillar interfaces. For the case of continuous confined elastic/viscoelastic adhesives (where the adhesive layer thickness is much lower than the adherent probe radius), the adhesion enhancement is usually rooted in energy dissipation during the debonding processes. The debonding process can take place either at the interface between the adhesive and adherent (interfacial and adhesive failure) or in the bulk of the adhesive material (cohesive failure). These debonding processes happen along with complex deformation patterns in form of short or long fibrils, air fingers that nucleate and propagate from the edge of adhesives, and cavities and air bubbles either at the interface or in the bulk of the adhesive. *Interfacial failure* usually happens fast with the formation and propagation of cavities at the interface. The adhesive layer undergoes trivial deformation and no adhesive residue would be left on the adherent. *Adhesive failure* occurs along with nucleation of the cavities and fingers at the interface in a mechanism called fibrillation. The adhesive layer undergoes extensive strain and deformation inside the fibrils but the fibrils detach from the adherent without leaving any residue. The fibrillation occurs along with strain hardening of the adhesive material inside the stretched fibrils. *Cohesive failure* is

14

along with formation of air cavities and fingers inside the bulk of the adhesive and fibrillation and extensive deformation of the adhesive layer. Detachment is along with the breaking of fibrils in the middle and leaving residue on the adherent. Propensity of a confined soft adhesive to experience one of these debonding mechanisms depends on the ratio between the critical energy release rate (g_0) and the elastic modulus of the adhesive layer (Y). Higher g_0/Y leads to adhesive and cohesive failure, while the lower g_0/Y leads to interfacial failure [56]. The visual description of all these mechanisms are elaborated in chapter 3.

A relatively newer class of biomimetic fibrillar adhesives utilize the above-mentioned adhesion enhancement mechanisms; it is a hybrid adhesive structure consisting of an array of elastic biomimetic micropillars terminated with a thin viscoelastic film (confined and continuous soft adhesive) [1,56]. The hybrid structure of this system was similar to the adhesive organs of the tree frogs. It was showed that the localized separation instabilities along with the more dissipative nature of the top layer in the hybrid structure remarkably enhances the adhesion force [1,56,71]. The observed adhesion enhancement of the viscoelastic film on top of the elastic micropillars suggested a significant synergetic interaction between the deformation of the top layer and sub-surface micropillars [1,56,71].

Besides this work, a few other publications report the integration of a dissipative material (like the "wet" nature of the tree frog toe pads) to both elastic flat and fibrillar interfaces (like the fibrillar nature of gecko foot pads). In these reports, the effect of chemical, mechanical, and geometrical gradient on the adhesion properties of such structures has been studied. For instance, Cheung et al. demonstrated a simple method to enhance adhesion by deposition of a thin layer of silicon oil on an array of a biomimetic fibrillar interface. The enhanced adhesion was attributed mainly to the viscous and induced capillary forces during the debonding [72]. In a similar attempt, Patil and coworkers coated a layer of liquid PDMS solution with a low content of cross-linker on an array of micro-posts and found enhanced adhesion with limited magnitude of deformation and less cohesive separation [73]. In both of these works the fibrillar interface is immersed in a viscous liquid. In addition, Carelli et al studied the effect of composition gradient in a viscoelastic bilayer during a debonding process. They found that the effect of gradient in composition of viscoelastic layers on adhesion and the mode of failure is complex, depending on the nature of probe [74]. Similar to this work, Patil and coworkers used an elastic PDMS skin to coat a viscoelastic layer of the same material to improve reusability and adhesive fracture [75].

The possible synergetic effect of the bioinspired fibrillar interfaces and their viscoelastic counterpart on the adhesive properties in a singular graded material have not been studied. The latest progress in this regard has been published in ref [1] and shown in the third chapter of this proposal. Other than the scientific insights obtained from this complex system, introduction of the functionally graded materials to the biomimetic adhesives may provide constructive solutions for the development of soft temporary adhesive materials. Recently, this type of adhesives have found their applications in technologies like micro-manipulation of miniature electronic devices [1,57,76].

2.1.2.2 Stimulus-responsive and smart biomimetic patterned surfaces

Although the emulation of biological structures with different levels of complexity has been accomplished, making such micro/nanostructured adhesives adaptive to external stimuli still remains a challenge [13]. To date, three general approaches have been reported in the literature to attain a particular response and function by external stimulation of biomimetic micro/nanostructured surfaces. None of these studies are aimed for fabrication of "smart adhesives" and only the undulation of the surface micro/nanostructures or their directional or anisotropic response were desired.

The first approach is based on anisotropic or asymmetric shape and arrangement of the bioinspired structures in order to derive a desired response to external stimulation. As can be seen in Figure 2-8, slanted micropillars and asymmetric arranged micro-posts are used to encourage directional adhesion, friction, and wetting [46,77–80]. Due to the stationary nature of the surface micro-textures, the desired function depends solely on the stimulation technique rather than a dynamic (and perhaps smart) response of the micro-structures. For instance, adhesion of slanted micropillars can be turned "on" and "off" only if they are positioned in a predetermined angle. Such structures can be used for emulation of frictional adhesion mechanism of geckos and their "on"/"off" functionality comes from an auxiliary means other than the dynamic shape change of the micropillars themselves. Or the water droplet propulsion on an asymmetric micro-structured surface is only rendered by judicious technique of external stimulation like programmed shaking or vibration.
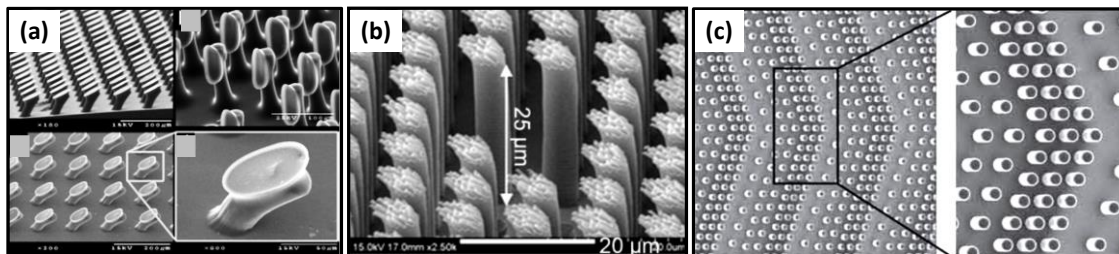
Figure 2-8. Anisotropic (a) slanted mushroom-shaped [46] and (b) hierarchical micropillars [54] for directional adhesion and friction; (c) asymmetric arranged micro-posts for directional wetting [79]

The second approach is based on chemical modification of the biomimetic micro/nanostructures with stimuli-responsive materials in order to make a micro-structured surface adaptive [81–87]. Polymer brushes and hydrogels have been frequently utilized to assist the dynamic response of the surface micro-structures to different external stimuli. In some cases, responsiveness can be restricted to the conformational change of the anchored macromolecules upon exposure to external stimuli. At higher extents, the deformation of the microstructures and alteration of the surface topography can be achieved at will. Hydrogel-Actuated Integrated Responsive Systems (HAIRS) are examples of such mechanisms. This technique, which requires the integration of mismatched materials, is typically achievable through complex chemical reactions. In addition, transport of fluids in case of the hydrogel and polymer brushes is imperative to induce a response, hampering easy applicability of such systems [3]. One example of HAIRS systems can be seen in Figure 2-9.

The third approach involves stimuli-responsive materials as structural materials for the fabrication of biomimetic micro/nanostructures. In contrast to other approaches, this method benefits from higher flexibility in programming both the stimulation and response as the chemistry and topography of the surface are strongly coupled [88,89]. There are few publications regarding the fabrication of stimuli-responsive biomimetic adhesives. Perhaps Reddy et al. were the first group to report the fabrication of a switchable adhesive. They used a shape memory thermoplastic polymer for fabrication of micropillars and studied the micropillars' bending and adhesion at different temperatures. The shortcoming in that work was non-spontaneous reversibility of the temperature-driven actuation process [88]. In another work, Jeong et al. used strain induced wrinkling of a PDMS films to create "on" and "off" states for the adhesive. The adhesive state in this structure was activated by mechanical straining of the wrinkled film, making remote control of the adhesion very challenging [90]. Later on, Krahn and Menon

introduced a new stimuli-responsive bioinspired adhesive system based on a conductive polymeric fibrillar interface. The PDMS in that work was filled with conductive carbon black and the switchable adhesion to dielectric counter-substrates was examined. The need for conductive polymers and physical connection to electrodes can be the main drawback of this system [91].
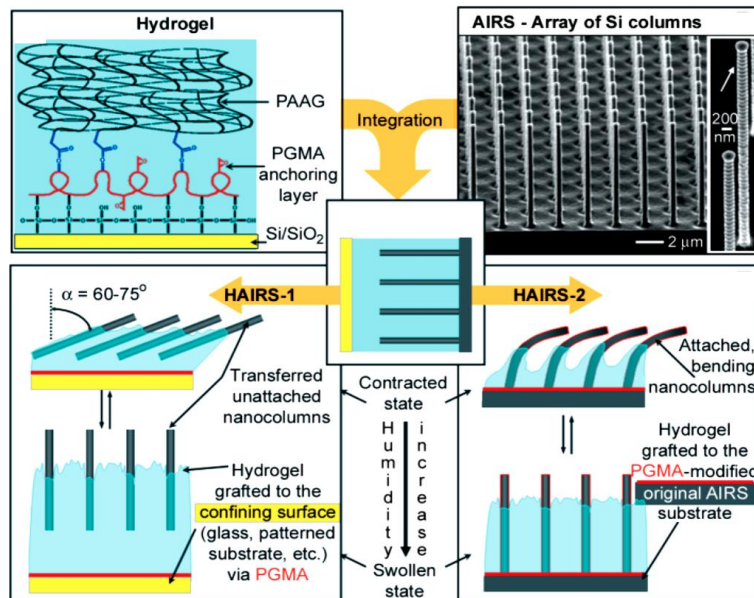
Figure 2-9. Hydrogel Actuated Integrated Responsive Systems (HAIRS) and their mechanism of actuation [82]

The latest progress in fabrication of adhesives with responsive surface topography is the use of LCEs and LCNs as a structural materials. Cui et al. reported fabrication of an adhesive made of LCE which was capable of action in "on" and "off" states. The switchability of this system relies on the temperature driven contraction of the LCE micropillars. The stimulus in this work is temperature which cannot be provided complete remotely and the actuation is limited only to the pillars. Also, the rigidity of this type of LCE hinders its use as a reliable soft adhesive, which is not industrially favorable. Likewise, Liu et al. used UV-sensitive cholesteric LCNs to create reversible switching of surface topography order to regulate friction [92]. Application of LCEs and LCNs in fabrication of adaptive surfaces is elaborated with more details in the remaining of this chapter. Although immature, the integration of LCEs and LCNs with biomimetic fibrillar adhesives seems a promising field of research. Therefore, this research project pursues integration of such smart materials to well-studied biomimetic fibrillar adhesives.

2.1.3 Applications of biomimetic adhesives

As mentioned in the introduction, switchable adhesives can be used in many applications such as consumer products (post-it notes and medical bandage [93]) and the assembly, packaging, and transportation of delicate objects in electronic devices. Micromanipulation, transfer printing, and transportation of liquid droplets and solid objects have been investigated and reported in literature. Some of the reports are focused on directional adhesion of slanted micropillars [94,95] or directional loading and unloading of straight micropillars [76,96] in order to employ them in transfer printing and transportation of light solid objects. Other groups use normal loading of the symmetrical pillars for attachment and their buckling for detachment and use this mechanism for modulation of adhesives in transportation of flat 2D objects [57,97,98]. Moreover, in a fashion with more resemblance to geckos, attachment/detachment of the fibrillar adhesives are facilitated by local stretching/peeling. Perhaps the first study using this mechanism was conducted by Xie and coworkers who used self-peeling of shape memory polymers in bonding/debonding of two solid flat surfaces [99]. More intricate versions of such mechanisms have been reported by switchable adhesion of fibrillar surfaces using the bending actuation of ion-exchange polymer metal composite [100]. Song and Sitti also reported manufacturing a soft gripper based on inflatable membranes embellished with mushroom-shaped micropillars [101]. The latest progress in this field is the application of LCN materials as artificial muscles for self-peeling of film-terminated fibrillar adhesives [19]. The details of this work is the scope of the fifth chapter of this dissertation.

2.2 Responsive Liquid Crystal Networks

2.2.1 Liquid Crystals

2.2.1.1 Basic terms and concepts

The transition between crystalline solid to isotropic liquid states is not abrupt in certain type of materials. In fact, these materials experience a different state of the matter between the crystalline solid to isotropic liquid phases which is called Liquid Crystal (LC) state. Solids have both positional (repetitiveness of the molecular structure) and orientational order. On the contrary, the packing of the molecules in liquids is random and without any order. A material in the LC state is a fluid by nature but still exhibits some degrees of crystallinity. The crystallinity is rooted in ordering of the molecules whether it be orientational or positional. The

main characteristic of liquid crystalline materials, which distinguishes them from other materials, is their anisotropic physical and optical properties. Particularly, anisotropic optical properties of LC materials is the basis of their wide range of applications in display technology. In brief, two conditions must be met for a material to be categorized as liquid crystal: 1) anisotropy of the molecular structure and 2) fluidity of the material. Some basic terms, concepts, and principles of the liquid crystalline materials are elaborated in the following section.

Depending on the molecular structure and chemical composition, LC materials are divided into thermotropic and lyotropic LCs. Thermotropic LCs generate liquid crystalline phase solely upon exposure to temperature alteration. Most commercial LC displays are based on this type of materials in which pure or a mixture of LCs are used. On the other hand, lyotropic LCs show transition to liquid crystalline phase only in solutions and upon variation in solvent concentration. Lyotropic LCs form different ordered phases like bilayers and micelles which are frequently observed and used in detergents and biological materials. Our research will focus on thermotropic LCs.

The molecular structure of thermotropic LC materials is anisotropic: calamitic (rod-like) and discotic (disc-like) molecular structures are the two main categories. We choose to use Calamitic LCs as they are commonly used in both research and industry. Figure 2-10 shows the schematic view of the structure and chemical composition of calamitic LC molecules.
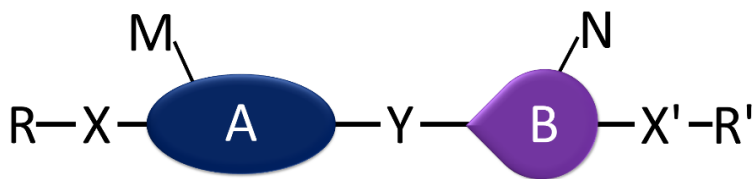
Figure 2-10. Schematic view of calamitic mesogens

Calamitic LC molecules usually consist of core groups (A and B) linked to one or two small polar or non-polar chemical substituents (M and N). The core is responsible for the rigidity of the molecule while the side groups make the molecule flexible. Linear or non-linear combinations of alicyclic or aromatic compounds are usually used in the core to provide rigidity and constraint in freedom. The side groups R and R' can be a variety of chemical compounds like straight alkyl or alkoxy chains and small polar substituents of CN, F, NCS, and NO_2 are commonly used. The alicyclic or aromatic core structures can be linked by different type of

chemical groups (Y). Linear and direct linkage or non-linear linkage through ester or ether groups are very common. The side groups can also be linked directly or through a bridge such as ester or ether groups to the core (X and X') [102].

The rod-like shape of the calamitic LCs creates a long axis and consequently anisotropy in the molecule. If there is a certain direction to which all rod-like molecules are inclined in orientation, a macroscopic "director" is formed, usually shown by $\hat{n}$. Moreover, depending on the ordering of calamitic molecules in a LC material different types of mesophases such as nematic, smectic, and cholesteric, are observed, as opposed to isotropic mesophase shown in Figure 2-11a. The least ordered liquid crystalline mesophase is called nematic mesophase. In this mesophase, the calamitic molecules are ordered in such a way that their principle axis is statistically oriented parallel to a director (Figure 2-11b). The molecular degree of order in a liquid crystal system can be quantified and translated to the macro-scale anisotropy using a term called order parameter (Q). This parameter is a function of the angle between the director and each individual molecule; the second order Legendre polynomial is usually used to quantify its value as follow:

$$Q = \langle P_2 (\cos \vartheta) \rangle = \langle \frac{3 \cos^2 \vartheta - 1}{2} \rangle \qquad \text{2-13}$$

In this equation, ϑ is the angle between the molecules' principle axis and the local director. Q is the result of temporal and spatial average over the unit volume of the LC material, while $<>$ represents the statistical average over molecules. For a system with fully ordered molecules, the order parameter converges to one and for an isotropic liquid the order parameters is equal to zero. The order parameter declines with increase in temperature and undergoes an abrupt fall to zero at the clearing point [102]. Simplicity of the nematics makes them the most known and investigated LC mesophase in theoretical and practical studies.
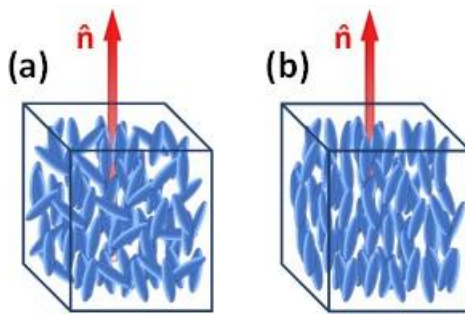
Figure 2-11. Schematic view of liquid crystals in (a) isotropic and (b) nematic mesophases.

2.2.1.2 Anisotropy of LCs

The special structure of the LC molecules gives rise to their anisotropic properties. Molecular order also leads to anisotropy in properties of the materials at larger scales. That is, the electrical, optical, magnetic, elastic and other properties of the LCs in molecular and larger scales are different when they are measured in a position perpendicular or parallel to the molecular long axis and director, respectively. For instance, if an incident beam of light is shone perpendicular to the principle axis of a calamitic mesogen the refractive index, $n_\perp$, will be different from the case the light is shone parallel to it, $n_\parallel$. The molecular optical anisotropy is equal to $n_\perp$- $n_\parallel$. The molecular anisotropy at the micro-scale is translatable to the bulk phase anisotropy at the macro-scale [102]. As a result of molecular anisotropy, a macro-scale uniaxially aligned LC system is birefringent and shows different indices of refraction upon exposure to an incident beam of light. If the incident beam is shone parallel to the director of the LC system, the refractive index is called extraordinary, or n_e, and in case it is shone perpendicular to the director it is called ordinary, or n_o refractive index. The ordinary and extraordinary indices of refraction are related to the molecular indices. The difference between these two refractive indices, i.e. $\Delta n=|n_e - n_o|$, is called birefringence and can be measured using polarized optical microscopy.

Similar to optical properties, mechanical, magnetic, electric and other properties of liquid crystalline systems can be outlined as molecular tensors. The translation of the molecular anisotropy to macro-scale anisotropy is facilitated using order parameters. The anisotropic deformation of the liquid crystalline polymers and elastomers are the most important feature of these materials that will be elaborated later in this chapter.

2.2.1.3 Surface anchoring and molecular alignment of LCs

A LC macro-domain consists of mesogenic micro-domains, each of which has their own director. Generally, there are three types of surface anchoring of the mesogenic units to the solid boundaries of a LC cell in a thin film geometry: 1) planar or homogeneous, 2) homeotropic, and 3) tilted. Figure 2-12 a-b represents two extreme surface anchoring configurations. The planar alignment is one in which all mesogens are parallel to the backing substrate. The planar alignment is disturbed when the mesogens hold a pre-tilt angle with the substrate. In another extreme, the homeotropic alignment takes place when the mesogens are perpendicular to the

substrate. Surface anchoring can be utilized as a starting point for deformation of the LC director fields. In fact, orientation of the director of the micro-domains can be changed systematically to produce different molecular alignment. Consequently, the combination of these two extreme cases results in three general director fields can be defined: splay, twist, and bend alignments as illustrated in Figure 2-12(c-e).
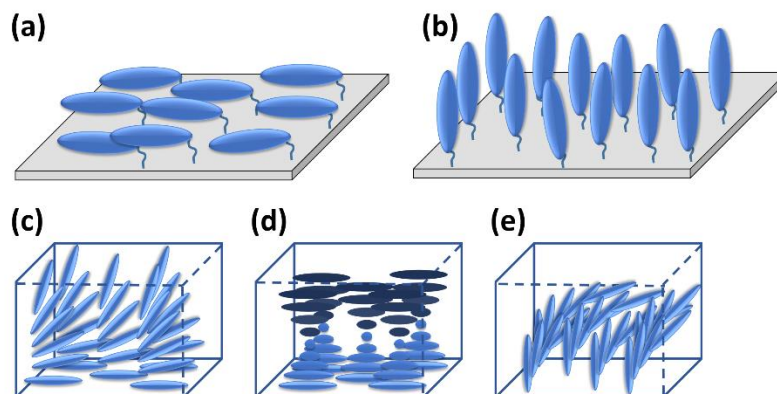
Figure 2-12. (a) Planar and (b) homeotropic surface anchoring, and (c) splay, (d) twist, and (e) bend deformation of directors field

The alignment of the LC molecules is dramatically influenced by the interaction of the mesogens to adjacent substrates. As a result, most of the commercially available alignment techniques are related to the surface preparation of substrates. Rubbing is the most common technique used in industry and research. For this method, a special type of polymer such as polyimide is dispensed on the substrate, cured and rubbed in a certain direction with a velvet cloth to control the LC alignment. Owing to the limitations of the rubbing method to be applied without dust or cloth trace at larger scales, other techniques have been investigated. Photoalignment [103], ion-beam irradiation [104] and oblique evaporation [105], use of micro-grooved [106] and chemically modified surfaces, Langmuir-Blodgett films [107] and flow are other common techniques for alignment of LC molecules [108].

2.2.2 Responsive materials and artificial muscles

The motility of the living organisms crucially depends on their response to external stimulation and the isothermal conversion of the energy received from internal or external stimuli, which are usually in different forms such as chemical, electrical, and mechanical energy [109]. Inspired by nature, scientists have devoted a great deal of efforts to developing materials

which are responsive to different internal or external stimuli such as heat, light, electrical or magnetic fields, pH or ionic strength, etc. These responses are usually manifested in alteration of shape and size, or surface, optical, chemical and physical properties. Shape and size change which lead to actuation and output mechanical energy are of particular interest in this project. Generally, actuators convert thermal, electrical, optical, magnetic and other forms of input energy to mechanical output energy. As a class of actuators, shape memory polymers (SMP) and alloys (SMA) generate mechanical energy upon their shape change. However, their use is limited as they secure only initial and final states and the transitional shape changes between the two initial and final states are not stable. In contrast, artificial muscles are a more attractive class of responsive materials due to their ability to take a continuum of shapes between two extreme states depending on the intensity and condition of the input stimulus energy [110].

Regardless of the structural material of an actuator, actuation performance crucially depends on the strain and stress, generated energy density, response time and theoretical efficiency [111]. Inorganic actuators such as electromagnetic and piezoelectric actuators have been the most common forms of actuators. However, the low torque to mass ratio and bulkiness of the electromotors hampers their use as artificial muscles in medical, robotic and fluidic applications. Despite high energy density that piezoelectric actuators provide, their inherently small strain (~ 0.1%) necessitates massive mechanical amplification [112]. Accordingly, organic or polymeric actuators have become more popular due to their availability, low cost and reasonable overall performance [113]. Polymer actuators have shown performances far better than muscles and have been utilized in medical devices, prostheses, soft robots, biomimetic and MEMS/NEMS devices [112]. Although polymer actuators can be stimulated by a variety of cues, electrical actuation has been more desired due to the very short response time. There are two general types of electrically actuated polymeric artificial muscles: 1) ionic electroactive polymers (IEAPs or wet EAPs) and 2) field-activated electroactive polymers (EAPs). Ionic polymer–metal composites, ionic gels, CNTs, and conductive polymers (CPs) fall under the category of IEAPs. The use of IEAPs is naturally limited due to their dependence on the liquid/solid electrolytes with high mobility of the ions. EAPs are more common with Dielectric elastomers (DE), liquid crystal elastomers (LCE), ferroelectric polymers, electrostrictive polymers and polymer electrets being the main polymeric materials of this category[112,114]. DE actuators are soft elastomer insulators confined between two compliant electrodes, as seen in Figure 2-13. Application of the electric potential to the electrodes generates an attractive force between them resulting in

stress/strain through the insulator. DE actuators are famous for their very fast response, large actuation force, high mechanical energy density and ability to hold induced displacement at constant voltage without consuming additional electrical energy. One of the major drawbacks of DEs is that their operation conditions is very close to the break-down voltage [115]. The stress across a DE material is expressed by Maxwell equation, $p = \epsilon_0 \epsilon_r |\vec{E}|^2$, where ϵ_0 is the permittivity of the free space, ϵ_r is the relative permittivity and $|\vec{E}|$ is the intensity of the electrical filed applied. Perline et al. have shown that for low strain actuators (e.g., < 20%) the thickness strain for DEs can be approximated by $\varepsilon_z = -p/Y = -\epsilon_0 \epsilon_r |\vec{E}|^2/Y$, where Y is the Young's modulus of the insulator film. Therefore, the strain energy density (output work density) can be approximated as $\overline{W} = 1/2\, Y \varepsilon_z^2$. Obviously, higher dielectric constant of the insulator yields higher mechanical energy storage capacity. The dielectric constant of the insulator can be increased by pre-straining the material and the addition of heavy nanoparticles such as TiO_2 [115].
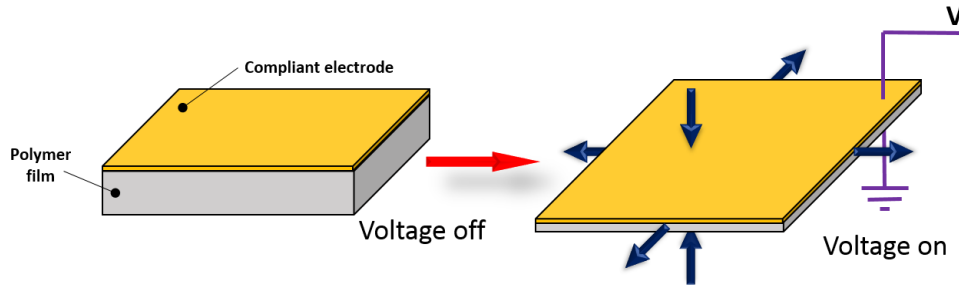
Figure 2-13. Schematic of a dielectric elastomer (DE) configuration

DE materials have demonstrated exceptional levels of actuation strain and stress using rather low cost acrylate and silicone-based polymers with medium response times [114]. However, actuation is theoretically constrained to simple in-plane strains such as expansion/contraction. Using structures with more sophistication in fabrication, such as bimorphs and multi-layer cylinders [116], might help tackle this problem. Only recently, Shian and co-workers have reported predetermined shape shifting of DE unimorphs with a few internal stiff fibers that facilitate breaking the symmetry of the strain during actuation. They have shown a variety of novel gripping actuators, suitable for soft robotics [117].

Liquid crystal elastomers and networks are a class of EAPs; their anisotropic rigid molecules (mesogens) are capable of polarization and reorientation in an applied electric field.

Such reorientation of the mesogens (either in forming the polymer backbone or being attached as pendant to it) leads to disorder in the molecular alignment and eventually shape change. In contrast to DEs, LCEs have shown remarkable shape shifting properties with more complex geometries that have not been achieved by simple manipulation of DE materials. For instance, Ware and co-workers have recently reported intricate thermally driven shape change of LCEs with spatial and local optical manipulation of the director and achieved local strains up to 55%. Similar to large LCD screens with tens of thousands pixels, they produced LCEs with up to 20000 3D-patterned elements known as "voxels" [118]. Still at an early stages of development, the incorporation of smart, real-time control over the shape of the LCE remains a challenge. This problem can be addressed by turning the liquid crystal orientation within each voxel using an electronic system integrated to the LCE [119]. The programmable mechanical response of these materials can lead to the manufacturing of reconfigurable, flexible, monolithic devices for use in aerospace, medicine, or consumer goods [118].

2.2.2.1 Liquid Crystalline Polymers, Elastomers and Networks

Liquid Crystalline Polymers (LCPs) are produced by the incorporation mesogenic units into polymer chains. If the functional groups of a monomer are substituted by mesogenic moieties, a side-chain LCP system (or SCLCP) is produced. In SCLCPs, the mesogenic units are attached by spacers to a backbone as pendant groups. If the mesogenic units take part in a condensation polymerization process, they will be located in the polymer backbone and produce main-chain LCPs (or MCLCPs). The spacer can connect the mesogenic group from either its end or center to the polymer backbone, creating end-on and side-on SCLCP, respectively (Figure 2-14) [3,4,6,8,120,121].
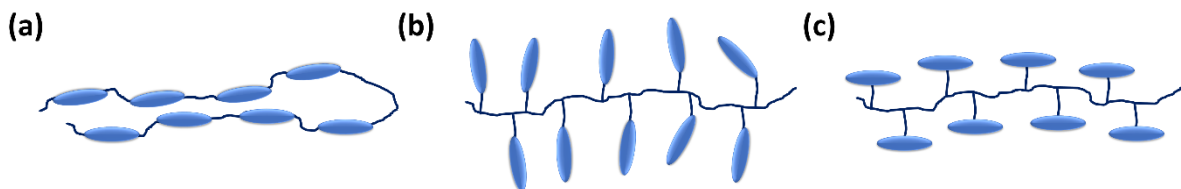
Figure 2-14. Schematic view of (a) MCLCP, (b) end-on SCLCP, and (c) side-on SCLCP

Liquid Crystalline Elastomers (LCEs) and Networks (LCNs) are cross-linked liquid crystalline polymers with low and high levels of cross-linking, respectively. Note that, the terms LCE and LCN might be used interchangeably throughout this thesis. The flexible polymer

network in LCEs contain rigid and anisotropic mesogenic units that are preferentially ordered like a liquid crystalline structure. Therefore, LCEs have properties of both elastomers (i.e. entropic elasticity) and liquid crystals (i.e. self-organization).

Similar to short chain liquid crystals, LCPs create nematic and smectic mesophases by orientational alignment of their mesogens principle axis. It is known that above the glass transition temperature T_g the polymer chains can move freely as a result of both macro-and micro-Brownian motion of the molecules. Once cross-linked, except at the micron scale, the macro-Brownian motion of the polymer chains is eliminated [6]. The free movement of the molecules at the micro-scale in a LCE allows the conformational change of the mesogenic units upon exposure to external stimuli such as heat or UV. Consequently, as they are fixed to the polymer network, any anisotropic micro-scale distortion can be translated to bulk material distortion. The condition for this situation is perfect alignment of all mesogenic principle axes in a certain direction. Otherwise, different and randomly directed molecular distortion vectors cancel out each other and no dimensional change in bulk of the material will be attained [3,4,6,8,120,121].

de Gennes theoretically studied and predicted the interaction of a polymer network with a liquid crystalline phase for the first time. He proposed the concept of LCE based artificial muscles [4,8,120,122]. These materials are supposed to mimic two main features of the human muscles, i.e. elasticity and contractility. The smartness of these materials is rooted in their reversible mechanical response, by change in the shape and size, upon exposure to a variety of external cues such as optical, thermal, electromagnetic, and ionic signals [8]. de Gennes' theory was experimentally confirmed by Finklemann and Kundler with the synthesis of the first side-chain liquid crystalline polymer cross-linked to a network [123].

The susceptibility of LCEs to experience bulk deformation upon external stimulation shows great benefit and potential as a smart material. Such an exceptional feature can be applicable in both industry and health sectors [124]. In fact, LCEs can be deemed a competitive substitute to common smart materials such as piezoelectrics, hydrogels, and other shape memory polymers. The applicability of LCEs has been examined in technologies like micromechanical systems [125], microfluidic systems [126], propulsion systems [15,127], and active smart surfaces which change their properties according to the environment. With regard to active surfaces, the optical

properties of the materials such as scattering, diffraction, and reflection [128] and physical surface properties (e.g. wetting and adhesion) have been modified using LCE surface structures [89,129,130].

2.2.2.2 Mechanism of deformation of the nematic LCE and LCNs

The unique feature of LCEs and LCNs, i.e. actuation in response to different external stimuli, is rooted in the coupling between the polymer chains of an elastomeric network and the liquid crystalline compounds. Herein, we adhere to the nematic phase which has the simplest form of orientation of the rigid rod-like mesogens in a uniform direction. In LCPs, LCNs and LCEs, preferential alignment of LC mesogenic molecules results in deviation of conformation of the long polymer chains from random coil conformation to other thermodynamically favorable chain conformations such as oblate or prolate conformations. . Due to this strong coupling between the LC mesogens and polymer chains, the nematic to isotropic phase transition of the liquid crystalline mesogens result in reorientation of polymer chains to the random coil conformation. In the random coil conformation, there is no preferred alignment of polymer chains in any direction. The LC mesogens can be present in the polymer chains backbone or be connected to them as pendant groups. As suggested by de Gennes, this coupling is the strongest when the LC mesogens are present in the polymer backbone [120].

Later on, Warner expanded the theoretical predictions of de Gennes to side-chain LCPs. He related the direction of the polymer backbone to the mean director of the mesogenic pendant groups. Three different types of relative arrangement were proposed as can be seen in Figure 2-15. In the first case, so called N_I phase, the polymer backbone is perpendicular to the director, while the principle axes of the mesogens are parallel. As a result, the LCP chain occupies an oblate spheroid conformation where the radius of gyration parallel to the director is smaller than the radius of gyration perpendicular to it ($R_{g\parallel} < R_{g\perp}$). In the second and third case, the polymer backbone is oriented parallel to the main director but the mesogens can be either perpendicular, N_{II} phase, or parallel to it, N_{III} phase. This orientation leads to a prolate ($R_{g\parallel} > R_{g\perp}$) spheroidal conformation of the LCP chain[3,120].
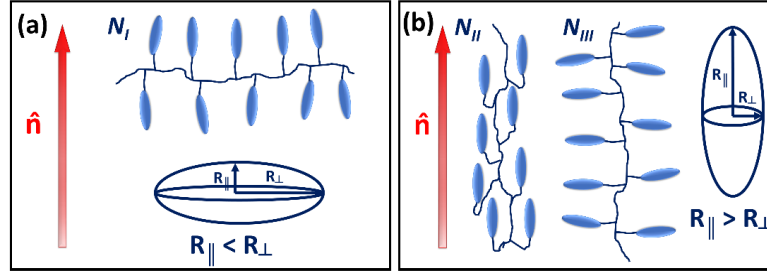
Figure 2-15. (a) Oblate and (b) prolate conformation of the LCP chains

The free energy of the polymer chains is at a minimum when they adopt the random coil conformation in an isotropic media. Upon exposure to an anisotropic phase, they tend to adopt an anisotropic conformation (either prolate or oblate spheroids). The polymer chains in LCPs, LCNs and LCEs are present in the LC medium. Hence, upon the phase transition of the LC mesogenic units from nematic to isotropic, polymer chains in the prolate conformation contract and those with the oblate conformation expand parallel to the direction of the director as shown schematically in Figure 2-15. This transition is reversible and obviously along with changes in microscopic shape and size. As mentioned earlier, a LCE system is a network of cross-linked LCPs. If a well aligned LCP system is cross-linked in a certain phase such as nematic or isotropic, any phase transition taking place for the mesogenic units will be translated to a macroscopic shape change. In fact, microscopic freedom of the polymer chains allows reorientation of the whole structure, both in the micro- and macro- scales, according to the preferred phase transition. The molecular deformation leads to deviation of the alignment of the mesogens from the director, leading to a change in the order parameter (Figure 2-16).
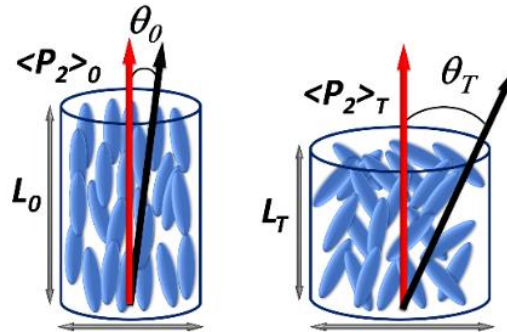
Figure 2-16. Schematic representation of the deformation of an ordered LCE network with change in order parameter, L_0 and L_T are initial and final length, $<P_2>_0$ and $<P_2>_T$ are the initial and final order parameters, and θ_0 and θ_T are the initial and final average tilt angle of the mesogens from the director.

Another determining factor for the deformation mode of the LCEs is the primary alignment of mesogens. It has been shown that the bending behavior of the LCE films is different for monodomain and polydomain crystals. In fact, the bending occurs along the alignment axis for monodomain and can occur in any direction for polydomain LCEs [131,132]. Kondo et al investigated the bending behavior of the homeotropic and homogenous aligned azobenzene containing LCE films. They showed that the LCE film bends toward the exposed UV source when the alignment is homogenous, whereas the homeotropically aligned LCE films bend in opposite direction of the light. The anisotropic deformation of the LCE films in this study is attributed to the UV absorption gradient in the thin film. That is, as seen in Figure 2-17, the exposed surface absorbs light more intensively, thus the deformation due to isomerization takes place anisotropically and more pronouncedly on the surface of the film [132].
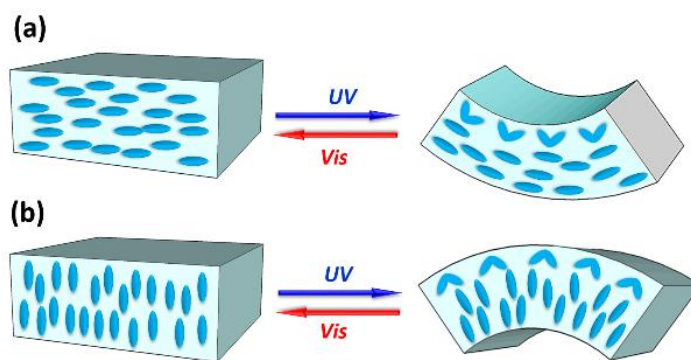
Figure 2-17. Light-driven deformation of azo-containing LCE films for (a) homogeneous alignment and (b) homeotropic alignment of the mesogens. Figure is adapted from [132].

In addition to the light-sensitive LCEs, bending behavior of thermo-responsive LCE films have been studied by van Oosten [110]. In this case, it is assumed that there is no pronounced thermal gradient in the bulk and all molecules are exposed to the external stimulus, i.e. temperature alteration, with the same extent. However, there exists an anisotropy of thermal expansion coefficient along the director and in other directions. Figure 2-18 represents the deformation mode of the thermotropic LCE thin films with different molecular alignments. For homogenous alignment of the mesogens, the anisotropy in thermal expansion coefficient is confined in-plane and leads to a slight deformation. For other molecular alignments, such as cholesteric, twisted nematic and splay, different 3D deformation can be obtained. Exposure of a cholesteric aligned LCE film to external stimuli such as heat causes out-of-plane deformation as a result of increase in the pitch of helices. The level of deformation depends on the degree to

30

which the director rotates. Twisted nematic is the cholesteric with the thickness of a quarter a pitch and its deformation is along with bending in two directions to a saddle-like structure. Finally, the deformation of a splay aligned LCE film is along with bending in only one direction. Accordingly, one can design and predict the deformation mode of the LCE film based on the molecular alignment of the mesogens.
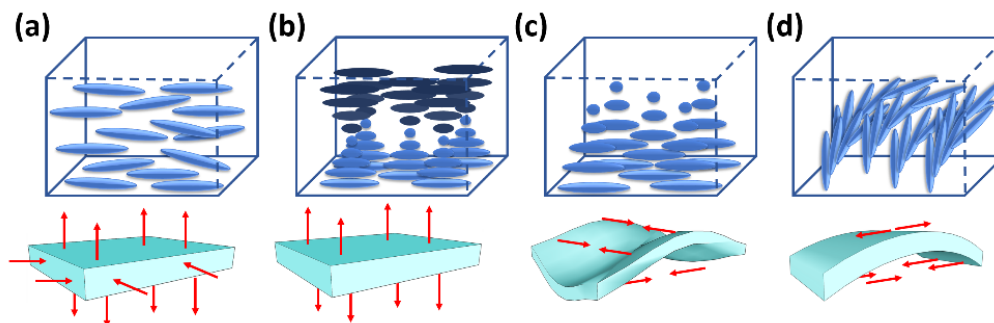
Figure 2-18. Temperature-driven deformation of the thermotropic LCE films for (a) homogeneous, (b) cholesteric, (c) twisted nematic, and (d) splay aligned mesogens. The figure is adapted from reference [110].

2.2.2.3 Chemical structure of the common LCE/LCNs and synthetic routes

Generally, synthesis of a LCE/LCN system requires build-up of LCP chains followed by cross-linking of them. Naturally, the cross-linking process of LCPs can be achieved either by in-situ polymerization of the LC monomers and cross-linking processes or cross-linking of the performed polymer chains, a reaction similar to vulcanization of the natural rubber [120]. Ohm et al. have categorized the chemical routes for synthesis of the LCEs to four general methods, which can be seen in Figure 2-19.
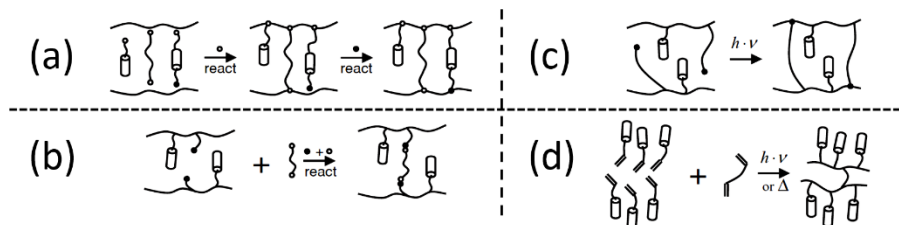
Figure 2-19. General routes for synthesis of LCEs

The first route, which is called "one-pot" method, is widely used for synthesis of silicone based LCEs (Figure 2-19a). The polymerization reaction takes place in only one batch containing a proper solvent, nonfunctional performed polyhydrosiloxane chains, mesogenic

31

groups, cross-linking agent and a proper catalyst. Usually platinum catalyzed addition of vinyl groups present on the cross-linking agent to the Si-H bonds of the polysiloxane chain takes place very fast in the first step of the reaction. The slower reaction between the Si-H bonds and methacryloyl groups makes it possible to fully cross-link the LCE network in a second step, while the solvent is fully evaporated or the polymer network is extremely thick. The alignment of the mesogenic units in this method can be achieved by the uniaxial stress of the preliminary prepared LCE. This method of alignment is the main shortcoming of the polysiloxane based LCEs for fabrication of miniaturic structures [3].

The second and third chemical pathways are based on the cross-linking of performed LCP chains (Figure 2-19b and c). In the second method, the LCP chains contain functional groups that undergo chemical reaction with the cross-linking agent in certain conditions. This method is also performed in a proper solvent. Thus, the alignment of the mesogens and LCs in a monodomain single crystal is problematic. Unlike the second method, the third method is solvent-free. The cross-linking agents are already linked to the performed LCP chains; and, only a trigger is needed to initiate the cross-linking process. The cross-linking agents can be photo or thermo-sensitive initiators that attack the C-H bonds in a H-abstraction mechanism. The absence of solvent in this type of process facilitates alignment of the mesogenic units through conventional surface or field induced alignment techniques.

And last but not least is a route in which the polymerization of the LC monomers and their cross-linking take place simultaneously (Figure 2-19d). This process requires a photo- or thermo-sensitive initiator and a cross-linking agent that may or may not be liquid crystalline. The most common monomers being used in this route are those functionalized with acrylates which are usually cross-linked by isotropic or liquid crystalline diacrylate monomers. The molten state of a mixture of all reactants are usually spread on a substrate that is formerly rubbed with an aligning compound. In this way, the alignment of the monomers before polymerization and cross-linking is facilitated. This method is commonly used in fabrication of the micro-scaled LCE structures.

2.2.2.4 Micro/nanostructured LCEs and LCNs

During the last decade, there has been a great body of literature on the fabrication of a variety of smart and responsive devices, e.g. sensors and actuators, based on LCEs. However, many of these works focused at the macro-scales. On the other hand, today's technology

necessitates fabrication and application of such devices in the micro- and nano-scales. Thus, the study and fabrication of micro/nano-scale LCE-based smart devices and surfaces seems attractive and timely, though without its own challenges. For instance, the proper alignment of the director of the mesogens and creation of a uniaxial mono-domain single crystal still remains as a difficult problem. In this section, we recapitulate the reported techniques for the fabrication of micro/nano-scale properly aligned single crystal LCEs and their applications.

Three major micro/nano-fabrication techniques reported in the literature are: 1) casting-based or templating techniques such as soft-lithography and capillary assisted lithography, 2) photo-patterning techniques, and 3) printing techniques like inkjet and micro-contact printing [133]. Furthermore, pulsed injection of LCE precursor and in-situ polymerization using microfluidic systems is used to generate mono-domain single crystal spherical beads [108].

2.2.2.4.1 Templating techniques

Templating techniques are based on the replication of a pattern from a master-mold. The replica is, in fact, the complementary pattern to the counterpart on the master-mold. Use of silicon based master-molds, i.e. silicon wafer as hard and PDMS as soft templates, is a prevalent practice in the field of micro/nanofabrication. Surface protrusions such as pillars are one of the most common geometries being fabricated.

Baugin and coworkers reported the first attempt toward fabrication of LCE micropillar actuators. They used the soft-lithography technique to pattern the calamitic LCE precursor which was previously developed [11]. The micropillars were made of a photo cross-linked network of nematic side-on mono-acrylate and di-acrylate monomers. Upon variation of the temperature, reversible shape change (30-40% strain) was observed due to the transition from nematic to isotropic phase. To enable a single crystal to contract in the longitude of the pillars, a small permanent magnet was used. In the same year, reversible shape shifting of the surface topography upon exposure to both UV and heat was reported by Yang et al [134]. They used soft-lithography technique for fabrication of nano-posts. It was hypothesized that the confinement of the feature size to the characteristic uniform domain size (ζ_D) would lead to an inherent mono-domain single crystal. Thus, the alignment would not be necessary. Nano-posts were made of side-on nematic polysiloxane based LCEs containing azobenzene moieties which was developed and reported in previous works [135]. In both works, the fabrication process was facilitated by an intermediate PDMS master-mold. Later on, Ohm and coworkers used porous anodized aluminum

oxide membrane (AAO) as a master-mold for fabrication of high aspect ratio bundled nano-fibrils and single nano-wires. The reversible actuation of the nano-fibrils in the direction parallel to the long axis of the fibrils was observed upon the change in temperature. Interestingly, one-dimensional confinement of the nano-fibrils facilitated the longitudinal self-alignment of the LCE molecules upon filling the nano-cavities [136].

The focus of all above mentioned works was on the fabrication and actuation of the micro/nano-structures. In 2012, a few groups reported their achievements in modulation of the adhesive, wetting, and optical properties by employment of LCE based fibrillar interfaces. For example, Cui et al. introduced the first biomimetic thermal-responsive fibrillar adhesive structure made of LCEs. They used the same LCE system, fabrication and alignment techniques that were reported in ref [11]. However, shape change of the micropillars was exploited to induce reversible adhesion of the patterned surface in an "on-off" condition. In fact, longitudinal contraction of the pillars caused a decrease in the height of the pillars and consequently decline in adhesion force [89].

Yan et al. studied the switchable reflectivity of a LCE surface patterned by micropillars. They hypothesized that the alignment of the LC moieties will be rendered by the shear forces induced during the filling of the micro-holes. That is, the alignment takes place at the vicinity of and parallel to the pillars' wall, while the LC molecules in the core are not expected to be aligned. Although not a perfect alignment method, it is sufficient to induce a reversible deformation by the cis-trans isomerization of the azobenzene moieties upon exposure to UV light. Thus, the optical properties of the surface can be modulated remotely just by exposure of the desired light [128].

Keller's group published two sequential papers on switchable wetting properties of the LCE fibrillar interfaces. Expectedly, geometrical variation of the surface micropillars leads to alteration of the contact angle of liquids poised on them. Accordingly, the thermo-responsive properties of the LCE system used in these two papers created a surface with tunable wetting properties in different temperatures [129,130].

2.2.2.4.2 Photo-patterning technique

Similar to conventional photo-lithography techniques, the photo-patterning technique is mainly based upon selective exposure of the LC molecules through a photo-mask. As can be

seen in Figure 2-20, the unexposed parts can be either etched away or be fixated in a different phase to form a heterogeneous surface chemistry and topography during the exposure to an external cue. The former method is called single-phase, and the latter multi-phase patterning [17,133,137–139].
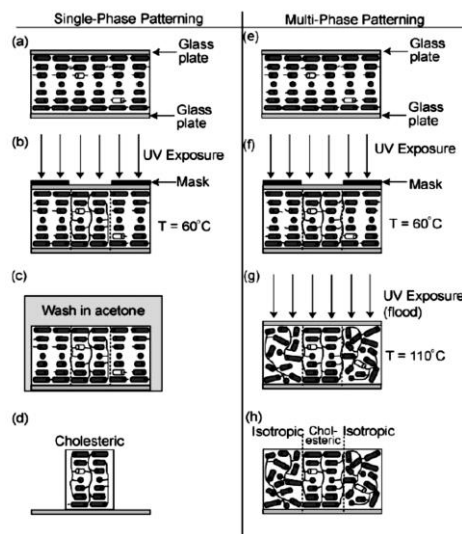
Figure 2-20. (a) Filling the LC cell with cholesteric LC precursor, (b) selective exposure to UV, and (c) developing in acetone to remove uncross-linked chains, to obtain (d) free standing micropillar. (e and f) are same steps but in (g) flood exposure has been done instead of developing to obtain (h) cholesteric LC pillar in a sea of isotropic LCs [137]

Using this technique, Sousa et al achieved thermo-responsive surface topology by fabrication of isotropic islands in a cholesteric sea. The chiral nematic phase was obtained by heating the original mixture to a proper temperature ($T_K < T < T_{N-I}$) and was locked during the photo cross-linking through a photo-mask. This step was followed by further increment of the temperature to isotropic phase ($T > T_{N-I}$). Then, uncross-linked molecules were shifted to isotropic phase and upon a flood exposure became cross-linked. The expansion coefficients of the chiral nematic and isotropic phases are different. Thus, the difference in expansion level of each phase led to creation of an array of surface protrusions at elevated temperatures [139]. A similar work was published by Elias and coworkers, where they compared the strain level and actuation efficiency of a single-phased patterned LCE with that of a multi-phased. Single-phase patterned samples, in fact, were chiral nematic LC molecules in shape of free standing micro-pillars. It is shown that a free standing micro-pillar actuates and deforms more efficiently than ones immersed in isotropic concomitants [137].

35

Recently, a new photo-sensitive switchable surface topography was reported with deeper surface modulation effect. The innovation in this work is the use of azobenzene moieties in the LCE system. That is, topographical modulation can be implemented remotely due to the cis-trans isomerization upon UV exposure. In addition, instead of isotropic sea used in other works, this work takes advantage of homeotropic alignment around the cholesteric phase. As these two phases have opposite photo-mechanical responses, the surface topology became more pronounced (Figure 2-21). Alignment of the mesogens in all of these works is facilitated by surface treatment of the substrates with proper chemicals. In addition, the cholesteric phase can be obtained by doping of the mixture with a small amount of common chiral mesogens.
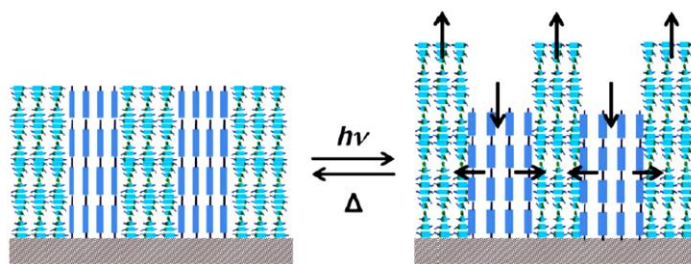
Figure 2-21. Counter actuation of homeotropic and cholesteric aligned micro-domains upon exposure to UV and heat[138]

2.2.2.5 Printing techniques

In these techniques, the pattern is transferred to a substrate either through the contact of an impregnated stamp (micro-contact printing) or through spraying a certain material from a nuzzle (inkjet printing) (Figure 2-22). These techniques benefit from low waste and ease of scalability to ultimately reach roll-to-roll production [133]. However, the creation of high aspect ratio structures with this method seems challenging. As the thickness of the ink determines the overall feature size, fabrication of the high aspect ratio structures requires numerous steps of printing.

A preliminary study on the micro-contact printing of a LCE mixture was reported by Elias and coworkers. A LCE mixture with and without chiral dopant was first spread on a substrate, then transferred to the second substrate and polymerized at a temperature below T_{N-I}[133]. In a more sophisticated experiment, van Oosten et al have fabricated a double layer micro-cantilever. Using multi-inkjet printing technique, they fabricated a bilayer composed of LCE doped by two different types of photochromic dyes. Planar and splay alignment of the LCE

molecules was facilitated by rubbing of a polyimide coated substrate and doping of the mixture with a special surfactant. As each dye was only responsive to a certain wavelength, different level and direction of the strain can be controlled upon exposure to light. This actuator, simulates the motion of natural cilia and is proposed to be useful in lab-on-chip applications [15].
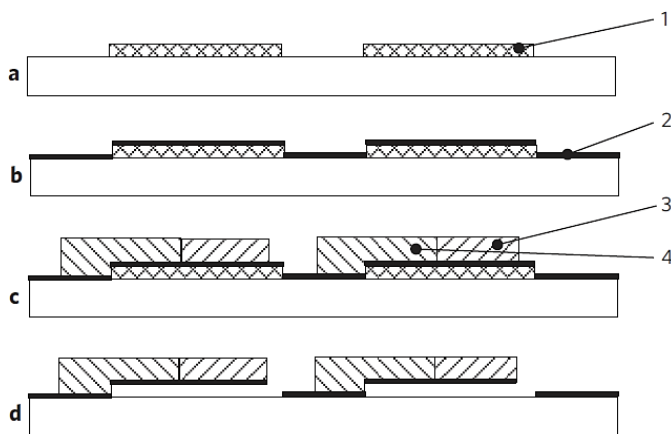
Figure 2-22. (a) Selective deposition of the PVA(1) as sacrificial layer, (b) deposition of polyimide aligning layer (2), (c) inkjet printing of the LC precursors (3 and 4), and developing of the PVA after curing [15].

2.2.2.5.1 LCE beads and micro-particles

The fabrication of micro/nanostructures from LCEs was not limited only to surface protrusions and cantilever shape structures. Ohm et al reported a pioneering work in the fabrication of LCE spherical beads in the micro-scale. In this work, the LCE monomers were stored in two syringes that are immersed in a hot bath. The continuous flow of the monomers leads to their mixing at the outlet. Then, a pulsed injection of the mixture into a continuous flow of silicon oil creates micro-beads that instantly polymerized by UV. Proper control of the flow conditions leads to alignment of the molecules in the beads (Figure 2-23). A remarkable actuation degree (70% strain) was reported for the transition between nematic to isotropic phases. Depending on the type of the molecular alignment, spherical and spheroidal beads can be obtained [108].
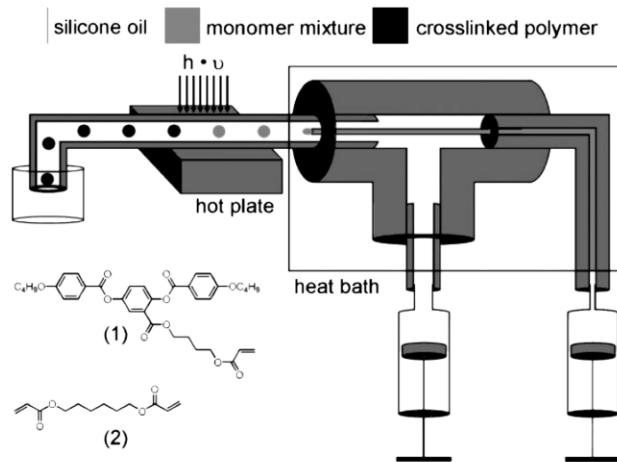
Figure 2-23. Microfluidic set-up used by Ohm et al. for fabrication of LC micro-particles[108]

Chapter 3
Biomimetic Functionally Graded Adhesive Materials[†]
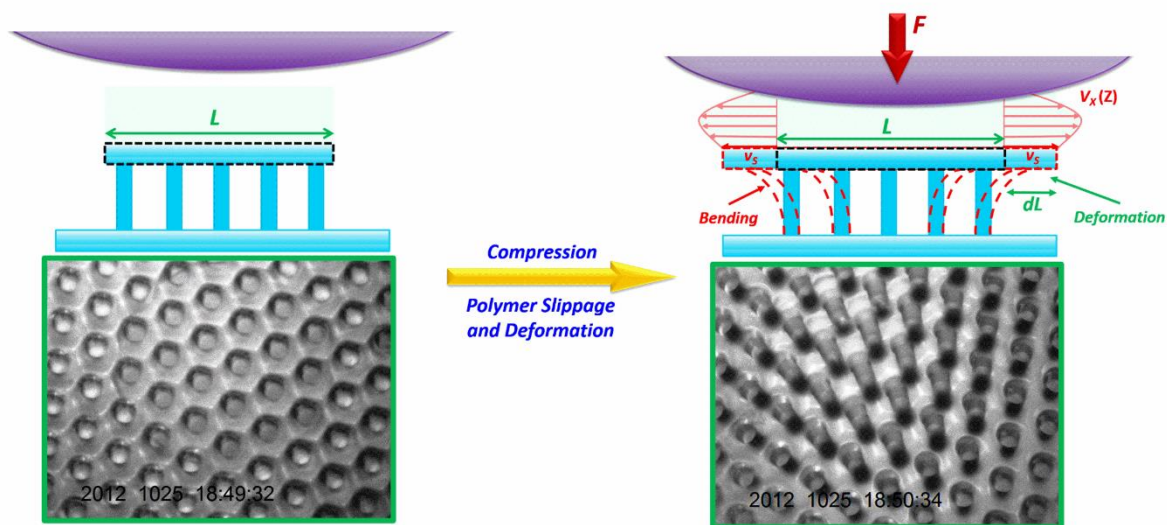
3.1 Introduction

Adhesion is an interesting phenomenon in nature and polymer adhesives are widely used in many manufacturing processes. The importance of adhesion and adhesives is continuously increasing for the development and manufacturing of advanced materials at ever-smaller scales. Other than the permanent structurally adhesive bonding, effective soft and temporary adhesive materials are in high demand for both consumer products (post-it notes and medical bandage) and the assembly and packaging of functional elements in electronic devices. The locomotive organs of the geckos and tree frogs are outstanding examples of the temporary adhesive materials. The amazing aptitude of these creatures to stick readily and rapidly to surfaces has attracted extensive research interests on development and application of biomimetic structures.

The adhesive functionalities of the gecko toe pads are rooted mainly in their sophisticated micro/nanostructures, which utilize the van der Waals intermolecular interactions and/or capillary forces to generate sufficient adhesive forces [38,42–44]. The hierarchical micro- to nano-structures on the gecko toe pads maximize the compliance, contact area, and accordingly effective van der Waals forces with the mating surface [45]. As a result of more than a decade of extensive studies, synthetic biomimetic fibrillar adhesives with a variety of geometries and materials have been fabricated. The first class of these structures is based on the simple surface protrusions such as pillars or posts [49–51], some with different tip shapes, e.g. mushroom-shaped pillars [46,52]. These have been fabricated in either single or multi levels from nano to micron scales [53,54]. Another class of biomimetic structures is based on incisions underneath the free surface of a material. Film-terminated micro-fibrils [55,56], bridged micro-fibrils [57], and capped micro-fluidic channels have been fabricated in single or multi levels of hierarchy [58]. Thus far, mushroom-shaped, film-terminated, and bridged pillars are introduced as the most effective prototypes. These synthetic structures have shown to increase adhesive strength and toughness of a flat control by combination of mechanisms such as contact splitting [59], enhanced compliance [60], and crack trapping [55]. In contrast to geckos, the toe pads of tree frog have relatively simpler structure, consisting of hexagonal micro-posts separated by grooves or channels which are covered by viscous fluids. The exact mechanism of adhesion of tree frogs is not fully understood but several mechanisms have been proposed such as capillary, friction, and viscous forces contributing to the total adhesion. For instance, it is believed that micro-scale hexagonal grooves and channels regulate the meniscus forces associated with the liquids secreted [41]. Water drainage in contact

has been offered as of one mechanism of the adhesion in wet condition. Thus, the adhesive ability of such systems may be rooted in a combination of the mentioned mechanisms [40].

Inspired by the amazing adhesion abilities of the toe pads of both gecko and tree frog and their surface structures, a few publications reported the integration of a dissipative material (like the "wet" nature of the tree frog toe pads) to both elastic flat and fibrillar interfaces (like the fibrillar nature of gecko foot pads). Although not explicitly stated, the effect of chemical, mechanical, and geometrical gradient on the adhesion properties of such structures has been studied. For instance, Cheung et al. demonstrated a simple method to enhance adhesion by deposition of a thin layer of silicon oil on an array of a biomimetic fibrillar interface. The enhanced adhesion was attributed mainly to the viscous and induced capillary forces during the debonding [72]. In a similar attempt, Patil and coworkers coated a layer of liquid PDMS solution with a low content of cross-linker on an array of micro-posts and found enhanced adhesion with limited magnitude of deformation and less cohesive separation [73]. In both of these works the fibrillar interface is immersed in the viscous counterpart. In addition, Carelli et al studied the effect of composition gradient in a viscoelastic bilayer during a debonding process. They found that the effect of gradient in composition of viscoelastic layers on adhesion and the mode of failure is complex, depending on the nature of probe [74]. Similar to this work, Patil and coworkers used an elastic PDMS skin to coat a viscoelastic layer of the same material to improve reusability and retain adhesive fracture [75].

To the best of our knowledge, the possible synergetic effect of the bioinspired fibrillar interfaces and their viscoelastic counterpart on the adhesive properties in a singular graded material have not been studied. We have previously reported the fabrication of a hybrid adhesive structure consisting of an array of elastic biomimetic micropillars terminated with a thin pressure sensitive adhesive film. Localized separation instabilities along with more dissipative nature of the top layer in that structure enhanced the adhesion remarkably [56,71]. The observed adhesion enhancement of the adhesive film on top of the micropillars suggested a significant synergetic interaction between the top layer and sub-surface micropillars.

The objective of this work is to systematically investigate the observed synergetic effects in a hybrid adhesive system consisting of a viscoelastic top layer and micro fibrillar base. The main difference between our structure and ones previously reported is the nature of the backing material and its interaction with a more dissipative top layer in a non-immersed geometry.

41

Systematic studies of three comparative adhesive structures, i.e. viscoelastic film, viscoelastic film coated on a soft elastomer, elastic film-terminated micropillars were performed in parallel to the newly-developed graded adhesive structure to acquire fundamental insights in the context of current understandings of viscoelastic polymer adhesion and biomimetic adhesion. The research findings in this work depict a new outlook to the question of "the combined role of shear and normal forces on the compliance, adhesion and friction of fibrillar structures"[140], which is an unsolved fundamental question in the field of biomimetic adhesion.

3.2 Experimental

PDMS (Sylgard® 184, Dow Corning) resin and curing agent were used in all adhesive structures. Schematic pathway of fabrication of the graded adhesive structure is shown in Figure 3-1. Hexagonal arrays of PDMS micropillars were fabricated through the soft-lithography technique. A 10:1wt mixture of PDMS (Sylgard® 184, Dow Corning) resin and curing agent were poured on a master-mold of micro-holes fabricated by DRIE process. The PDMS coated master-mold was cured at 90^{0}C for 1 hour and the PDMS was peeled off the master-mold after curing. The resultant positive structures were pillars with 50μm diameter, 150μm height and 115μm center-to-center spacing (surface density of 17%). The final thickness of the cured PDMS backing film was controlled to be 1000 ± 100μm.
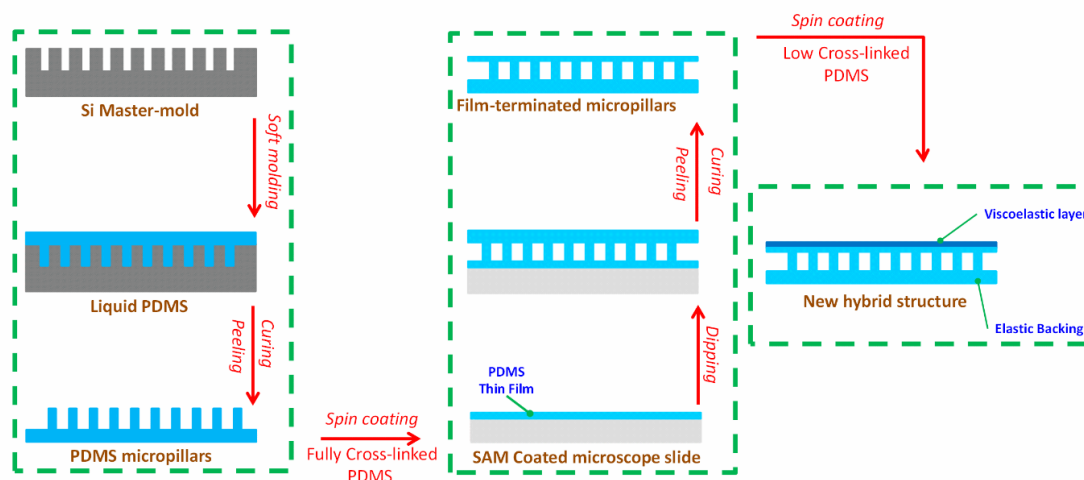
Figure 3-1. The schematic view of the fabrication pathway including the three key steps of soft-lithography and micro-inking which are followed by coating of a viscoelastic layer on top of the elastic film-terminated micropillars

Dipping method developed in reference [55] was used to fabricate thin film-terminated pillars. A thin layer of PDMS was spun on a low surface energy microscope glass slide. The reduction of the surface free energy was achieved by coating a self-assembled monolayer of heptadecafluoro- 1,1,2,2,tetrahydrodecyltrichlorosilane on a glass slide as described in reference [141]. The spin speed and time determine the final thickness of the terminal film. Fabricated micropillar arrays were placed upside-down on the thin PDMS layer and kept in room temperature overnight to ensure the contact between all pillars' tips and the thin film. The entire system was placed in the oven at 90^0C for 1hr and the cured sample was peeled off gently. Thickness of the terminal films, which was varied from 8 to 24μm, measured by weighting the samples and confirmed by the optical interferometry. Coating of the elastic film-terminated fibrillar structures with the viscoelastic top layer was performed using the spin coating technique. Again, the thickness of the terminal viscoelastic layer was adjusted using spin speed. Weighting of the samples and optical interferometry were used to estimate the thickness of the terminal viscoelastic film which varied from 18 to 50μm.

Oscillatory frequency sweep and shear relaxation tests were performed using a RA2000 model rheometer (TA Instruments) to characterize the thermomechanical properties of 100:10wt, 100:4wt and 100:1.6wt PDMS mixtures. PDMS mixtures were poured on the bottom plate of a plate-plate geometry and cured at 90°C for 1 hr. The instrument environment was then cooled down to room temperature to perform the oscillation. The maximum oscillation amplitude was set to 3% to avoid any non-linear response. The time dependent shear modulus ($G(t)$) of the sample was measured in a shear relaxation test for 30 minutes. The obtained storage (G') and loss (G'') moduli of the samples were recorded in order to estimate of the liner rheological properties of the terminal film.

Adhesive properties of all samples were characterized by the indentation of a 6mm diameter hemispherical fused silica probe (Ispoptics Co., NY, USA) using a micro-indenter assembled on top of an inverted optical microscope. The load–displacement data were measured with a 0–10g load-cell (GSO-10, Transducer Techniques). The contact area and deformations during loading and unloading processes were visualized from the bottom-view images. The set-up was equipped with a side-view camera to monitor the possible necking during separation and the mode of separation. The loading velocity in indentation tests was maintained 1μm/s for all of the samples. Upon reaching the preload force, a slight decrease in the force and an expansion

of the contact area were observed due to the stress relaxation in the viscoelastic layer. The contact time was set to 30 seconds, where the expansion of the contact area levelled off. The holding time was also much greater than the effective shear relaxation time of the sample obtained from rheology tests.

3.3 Results and Discussion

3.3.1 Fabrication and characterization of adhesive of properties BFGAs

We use PDMS materials to make the biomimetic structures because PDMS has low surface energy and adhesion and is commonly used as a releasing agent. The viscoelasticity of the PDMS can be readily changed by varying the curing agent to resin ratio, making it a good model system to investigate the fundamentals of the complex graded materials. Previous works showed that a flat film of 100:10wt PDMS can be deemed purely elastic having very low adhesion. Introduction of the biomimetic micropillars with different tip shapes, e.g. mushroom tipped, bridged, or film-terminated pillars, bestowed non-adhesive elastic PDMS remarkable adhesive properties [46,52,55–57]. We have previously reported an enhancement of pressure-sensitive adhesives using a thin PDMS film-terminated PDMS fibrillar interface. In that work, the curing agent to resin ratio of the terminal film was set to 100:4wt. Although more dissipative than 100:10wt PDMS, 100:4wt PDMS was elastic rather than viscoelastic [56,142]. We speculated that using more dissipative PDMS as the terminal layer would result in better adhesive properties in terms of higher adhesion energy and pull-off force. To make a more viscous layer, we varied the concentration of PDMS mixtures from 100:4wt to 100:1.2wt. We limited our study to solid-like state of the matter to avoid excessive complications in the study of liquids in contact.

Figure 3-2a shows a schematic view of the new hybrid graded adhesive structure. It consists of three components: a viscoelastic top layer, an elastic intermediate layer and elastic biomimetic micropillars. h' is the thickness of the elastic and h represents the thickness of the viscoelastic terminal layer. Figure 3-2b shows a viscoelastic layer coated on the glass substrate (deemed as a simple non-graded structure); Figure 3-2c shows a viscoelastic low cross-linked PDMS layer coated on a fully cross-linked PDMS film (deemed as a chemically graded structure); and, Figure 3-2d shows an elastic film-terminated fibrillar adhesive (deemed as a geometrically graded structure). For clarity and brevity, we designate the adhesive samples by the immediate backing material to the terminal layers (i.e. P for the flat PDMS film, and B for

the biomimetic fibrillar adhesive), elasticity (E) or viscoelasticity (VE), and the thickness of each terminal layer (h or h'). For instance, B-E12-VE50 represents a graded adhesive structure consisting of a terminal viscoelastic layer of 50 μm in thickness backed with a biomimetic fibrillar interface with intermediate elastic layer of 12μm. Note that a glass slide is employed as the supporting substrate for all the adhesive samples and has not been considered as a part of the adhesives. Geometrical features of the fabricated samples are summarized in Table 3-1
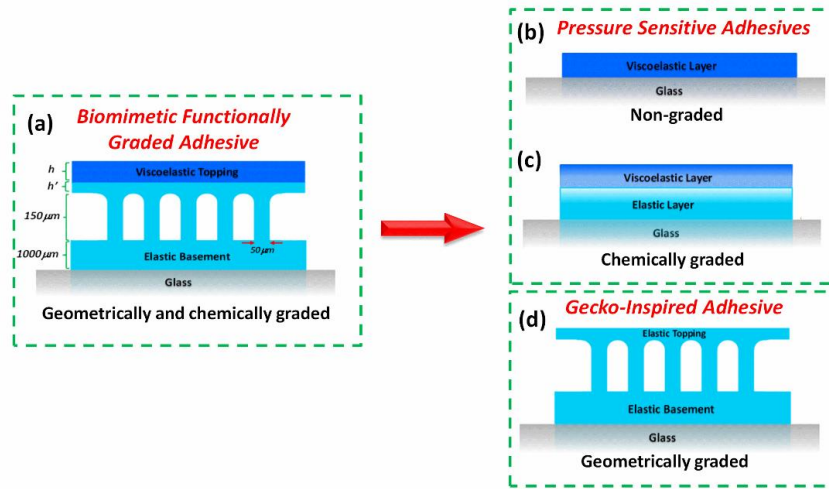
Figure 3-2. The schematic view of the (a) biomimetic functionally graded adhesive B-E12-VE50, control samples (b) viscoelastic layer on glass VE50, (c) viscoelastic layer on the polymer P-VE50, and (d) the elastic-film terminated biomimetic fibrillar adhesive B-E12

Table 3-1: Geometrical features of the fabricated and tested samples

Sample	Elastic terminal layer thickness, h' (μm)	Viscoelastic terminal layer thickness, h (μm)	Schematic
G-VE50 (Viscous film)	-	50	
P-VE50 (viscoelastic film on elastic film)	-	50	
B-E12 (elastic film-terminated)	12	-	
B-E12-VE50 (viscoelastic film-terminated)	12	50	

The viscoelastic properties of PDMS with varied degree of cross-linking were characterized. Figure 3-3a demonstrates the variation of both storage and loss components of the modulus (*G'* and *G''*) against content of cross-linking agent for three mixtures of 100:10wt, 100:4wt, and 100:1.6wt during a frequency sweep rheology test. The storage modulus for both 100:10wt and 100:4wt is almost independent of the frequency, while its variation against frequency is more pronounced for the 100:1.6wt sample. Also, the loss modulus of the 100:10wt PDMS is almost three orders of magnitudes greater than that of 100:1.6wt mixture. The damping factor *tan δ* of the 100:1.6wt mixture is higher than that of both100:10wt and 100:4wt mixtures, indicating its more viscoelastic or dissipative nature. Figure 3-3**b** shows the variation of the shear modulus against time for 100:1.6wt PDMS mixture. The relaxation test was performed under 3% shear strain for 1800s. The shear modulus regime change took place at t*<<30s. In fact, 30s holding time is quite larger than the stress relaxation time and thus the polymer can be assumed to be fully relaxed.
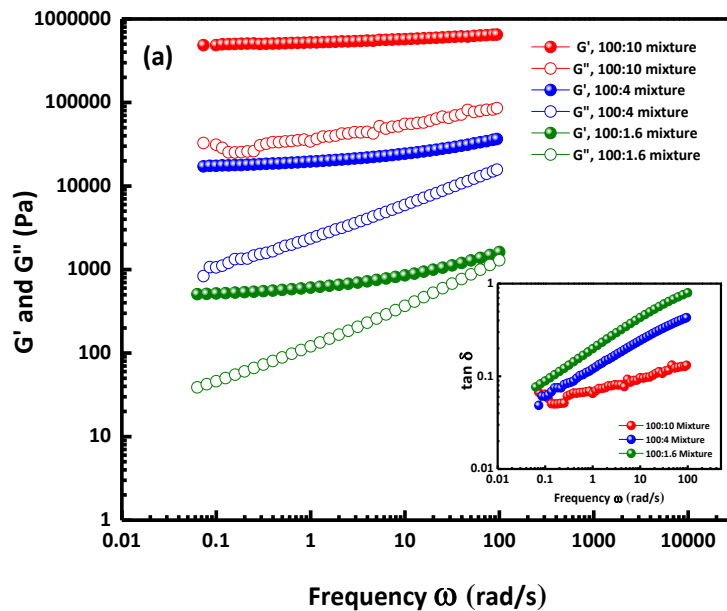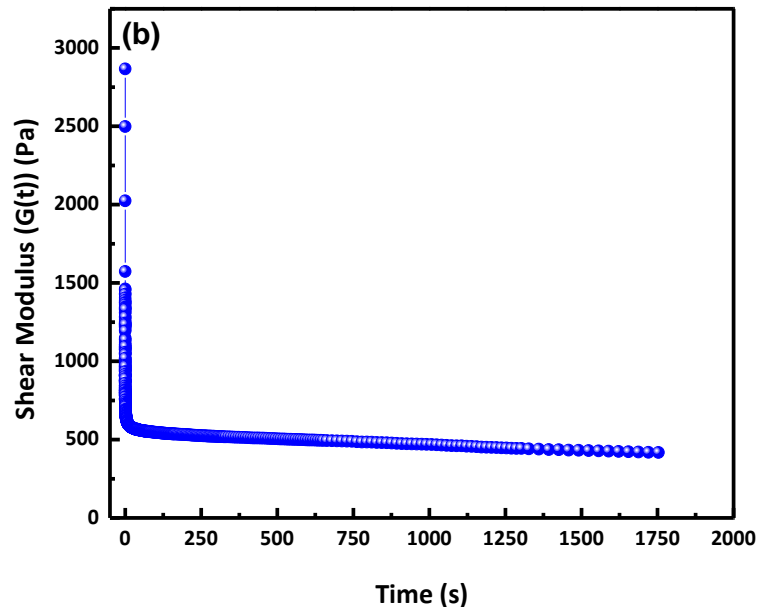
Figure 3-3. (a) Rheological properties of the 100:10, 100:4, and 100:1.6 wt PDMS mixtures, (b) variation of shear modulus against time during a shear relaxation test

100:1.6wt PDMS mixture was chosen to make the top layer because it is close to transient gel point of the PDMS and it can be assumed fairly as a viscoelastic material. However, the micropillars could not be topped easily through the dipping method due to the cohesive peeling of the low cross-linked PDMS from the glass substrate. The solution developed here was to coat an elastic thin film-terminated fibrillar structure with the liquid PDMS. Figure 3-4a is obtained from optical microscopy of the sample B-E12, in which the terminal film and micropillars are easily distinguishable. Surface defects in the form of cavities were sporadically located on the elastic terminal film. Figure 3-4b represents the SEM micrograph of the sample B-E12. It seems the presence of the slightly rippled surface on the terminal layer is inevitable as a result of capillary rise of the liquid PDMS within the micropillars. Such surface instability must be minimized or covered well to avoid any undesirable effect on the adhesion test. Undesired effects of such instabilities on the adhesion have been reported by Nadermann et al [143]. These surface instabilities can be replicated on the viscoelastic layer if the thickness of the terminal viscoelastic layer is below a critical amount. A detailed study on the effects of such surface instabilities on the contact behavior has been reported in [144]. Herein, we minimized the extent of this surface instability by making a smooth terminal film. For this purpose, the viscoelastic terminal layer was chosen to be thick enough so that an approximately smooth surface can be achieved.
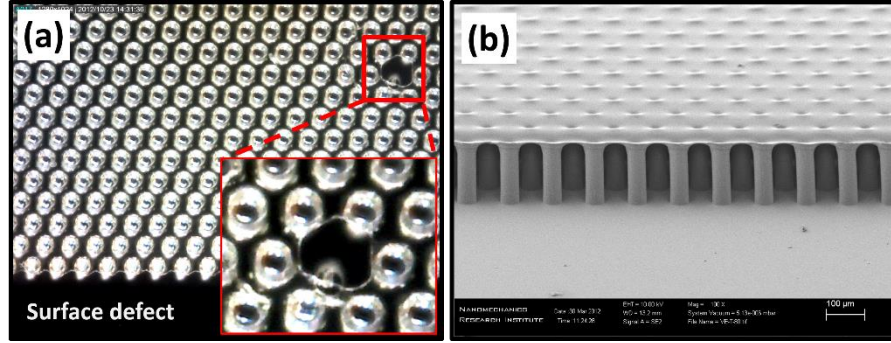
Figure 3-4. (a) Optical micrograph of the sample B-E12 with a surface defect on top right corner, and (b) SEM micrograph of the sample B-E12

An efficient viscoelastic–adhesive must show strong adhesion to a substrate surface and retain its cohesive strength during the separation. This requires a careful design of the adhesive in terms of both thermomechanical and geometrical properties, such as terminal layers thickness, the fibrils' arrangement, spacing, and aspect ratio. The effect of geometrical features such as spacing, fibrils' length, and arrangement have been studied thoroughly in recent literature [145,146]. It is shown, that the energy release rate for an elastic film-terminated structure is strongly proportional to w^4, where w denotes the inter-fibrillar spacing and weakly scales with fibrils length, i.e. $L^{-1/4}$, where L is the fibrils height. Moreover, it has been shown that the hexagonal arrangement of the fibrils with the same surface density as of the square arrangement results in stronger adhesion energy and pull-off force[145]. For the hybrid graded adhesive structures reported in this work, the thermomechanical and geometrical properties of the micropillars remain constant; the varied parameters are the thickness and elasticity of each of terminal layers.

In order to achieve the most efficient structure, we first varied the thickness of the elastic terminal layer to obtain an optimum thickness. Figure 3-5 shows the variation of the pull-off force vs preload for micropillars topped with different thicknesses of the elastic terminal layer. The pull-off force of elastic film-terminated structures increased with decrease of the thickness from 24μm to 12μm over the entire range of preload. The same trend was observed for sample B-E8 having the thinnest terminal layer but only at high preload. At low preload, the B-E8 has the lowest pull-off force and the separation instabilities such as cavitation and fingering phenomena were observed on top of the fibrils. In contrast, for other samples with thicker terminal films, separation instabilities were constrained to only crack trapping on the crack line. Thus, we chose sample B-E12 as the elastic foundation for the terminal viscoelastic layer in

order to have the highest possible pull-off force while having no pronounced debonding instabilities on top of the fibrils. In general, we speculated that, the thinnest possible elastic terminal film topped with the thickest possible viscoelastic layer will create the most efficient adhesive structure. A similar assumption has led to fabrication of efficient reusable PSAs with an elastic skin in the study by Patil et al [75]. In that work, the adverse effect of the elastic skin shielding the PSA's adhesion strength and viscoelastic loss is attenuated by decreasing the elastic skin thickness. In our study, the elastic film is between the micropillars and the top viscoelastic layer. Thus, it may shield the desirable effect of the micropillars in enhancement of total compliance of the new hybrid structure.
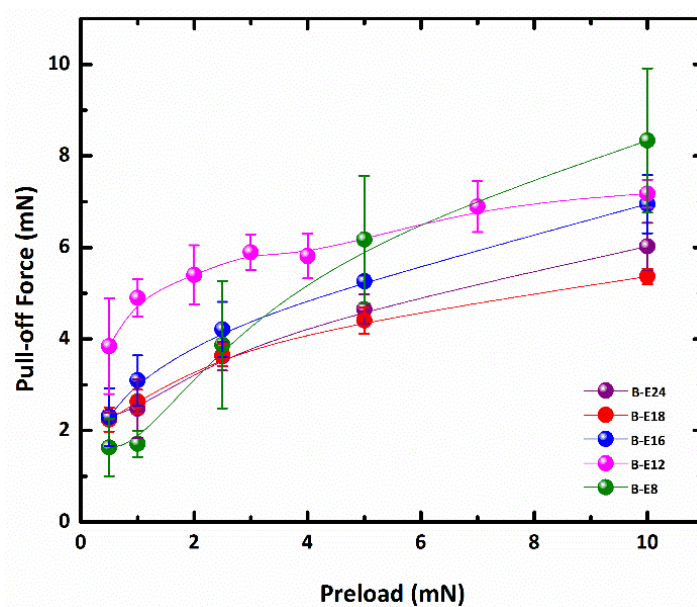
Figure 3-5. Effect of thickness of the elastic terminal layer on the pull-off force of film-terminated fibrillar adhesives

Figure 3-6 shows the variation of pull-off force vs preload for viscoelastic layers of varied thickness coated on the sample B-E12. The thicker the viscoelastic layer, the higher the adhesive pull-off force is achieved. The influence of the thickness of a viscoelastic layer on the adhesion properties in an axisymmetric probe test experiments has been reported in only a few references [56,147–149]. Generally, it is believed that the thicker the viscoelastic layer the greater adhesion energy and the pull-off force. However, to the best knowledge of authors, theoretical study on the effect of thickness was not reported in literature thus far perhaps because of the complexity of debonding instabilities. Note that the effect of thickness on the adhesive properties

49

of the viscoelastic adhesives have been well studied for other testing geometries such as peeling geometry [148]. Results show that there is an optimum thickness point for viscoelastic adhesives at which the adhesion energy and pull-off maximizes. From the experimental evaluation of the thickness effects in Figures 5 and 6, the sample B-E12-VE50 was chosen as the hybrid graded adhesive structures to investigate the interplay between the top viscous layer and the micropillar base. Furthermore, the viscoelastic PDMS having the same thickness was coated on the glass and a thick (≈ 2mm) flat PDMS elastomer film to obtain flat control samples, VE50 and P-VE50. The initial elastic film-terminated structure, B-E12, was chosen as the third control sample.
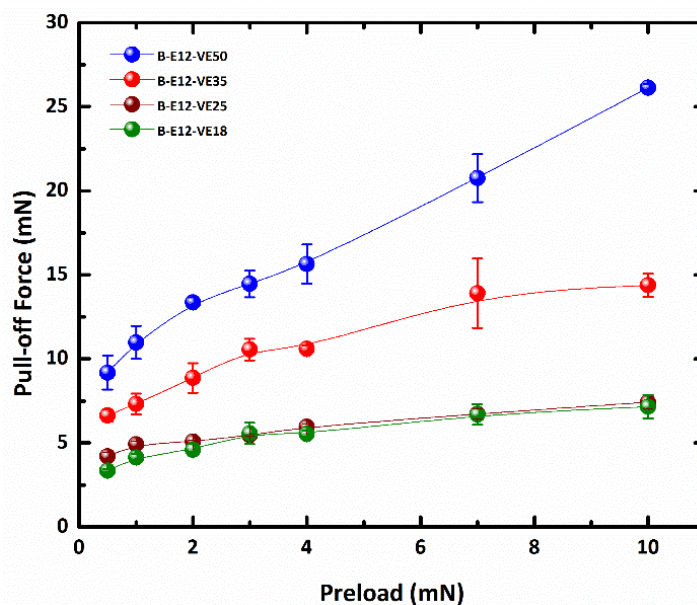
Figure 3-6. Effect of thickness of the viscoelastic top layer on the pull-off force of the new hybrid structure

The load-displacement curves of the four types of adhesive structures (**B-E12-VE50, VE50, P-VE50**, B-E12) are shown in Figure 3-7. There is no noticeable snap-in force for the elastic sample B-E12. For all other samples, bonding process starts with a pronounced snap-in force **when probe approaches to the surface because of the intermolecular surface forces**. Following that, a normal compressive load (i.e. preload) of 0.5mN was applied to enlarge the contact area. During unloading, the load-displacement curves were linear for a remarkable range of retraction distance before reaching the pull-off point where the tensile adhesive force is the highest. The debonding for the elastic sample B-E12 is rapid and has several small zigzag steps, suggesting

50

the presence of crack trapping mechanism during the separation. The debonding process of the viscoelastic samples is gradual and smooth but undergoes a slope change between the pull-off point and the separation. This slope change is indicative of the bulk deformation processes such as fibrillation, cavitation and other instabilities as discussed in later section. The slop change is most pronounced for the viscous film on polymer (P-VE50), becomes less for the viscous film on glass (VE50), and is the least pronounced for graded structure (B-E12-VE50). This observation suggests the possible change of crack mechanisms during the separation.
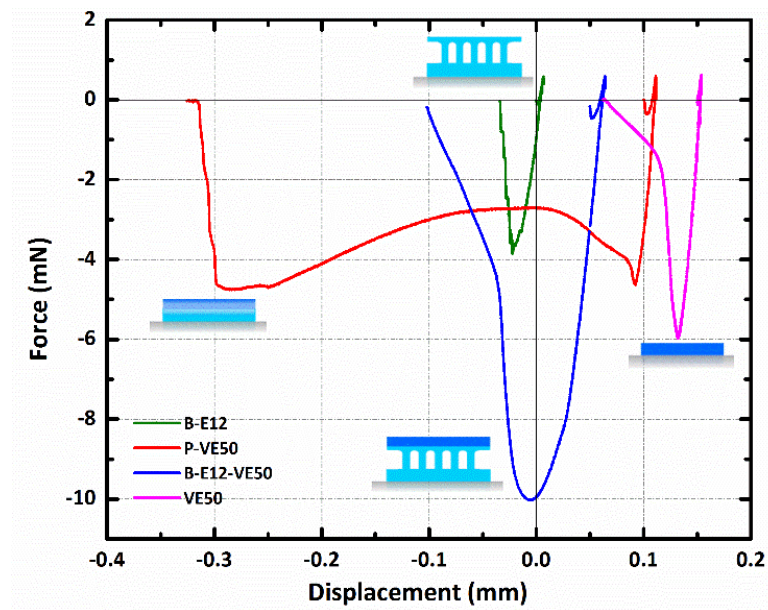
Figure 3-7. Typical load vs displacement curves for indentation test on four different samples under 0.5 mN preload

To quantitatively characterize the crack mechanisms and energy dissipation processes, we divided the unloading curves into two phases, as shown in Figure 3-8: (phase 1) crack initiation before the pull-off point and (phase 2) crack propagation after the pull-off point. The consumed energy for each phase gives a coarse idea about the sink of energy and the mode of separation in each system. Inset table in Figure 3-8 shows the ratio of the energy required for each phase with respect to the energy required for the entire debonding process. The required energy for the phase 2 of the sample P-VE50 is about 88%; the energy dissipation processes include instabilities such as vertical fibrillation, fingering, and cavitation. As a result, this system is prone to experience cohesive failure and the extent of plastic deformation is also higher than that of other samples. The required energy for the phase 2 of the sample B-E12-VE50 is about

51

54%, which is much less than that of the sample P-VE50 (88%) and even lower than that of sample VE50 (58%). The comparison between the relative amounts of energy dissipated in the crack propagation revealed that less energy is consumed in the separation of the graded adhesive structure than that of a simple viscoelastic film. This situation renders the detachment process to take place at the interface or at the adhesive mode of separation. Thus, the base micropillars inhibit the cohesive failure of the viscous film, leading to an adhesive material with higher structural integrity. To verify this analysis, we carefully examined the debonding using a side-view and a bottom-view CCD camera. Bottom view images confirmed that the mode of failure for the sample B-E12-VE50 is adhesive since there is no residue left on the probe. Although having a large elastic deformation, the adhesive layer had experienced no discernible plastic/permanent deformation. In contrast, intense bulk deformation and vertical fibrillation were developed during the separation process for the sample P-VE50. In addition, we observed cohesive failure for some of the samples. The following section shows the detailed evolution of the contact area and its deformation and instabilities during loading and unloading.
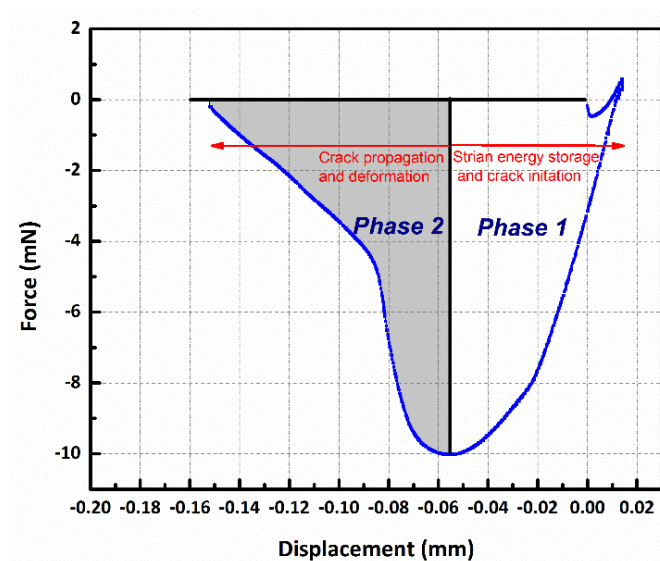
Figure 3-8. The division of two phases during the debonding of the sample B-E12-VE50 under 0.5 mN preload. Phase 1: strain energy storage and crack initiation; Phase 2: crack propagation processes. Inset table lists the contributions of each phase in total energy dissipation during the debonding of the four adhesive structures.

3.3.2 Evolution of adhesive contact area and separation instabilities

The evolution of the adhesive contact and separation was observed and recorded by the bottom view camera showing a full indentation cycle on the samples B-E12, P-VE50, and B-E12-VE50. The contact area during the loading was measured from the bottom view image as shown in the first column of Figure 3-9. In our experiments, the preload varied from 0.5mN to 10mN. Dashed circles indicate the contact line at the preload point. Apparently, the sample B-E12-VE50 always has the greatest contact area, suggesting this sample has the highest compliance, while the sample B-E12 has the smallest contact area. The contact area for samples VE50 and P-VE50 are roughly comparable to the one for the sample B-E12-VE50 under the preload of 0.5mN, but the difference between them starts to grow for higher preloads. Note that the contact area increased with preload and became even larger than the imaging frame for the viscous/elastic-pillar sample B-E12-VE50 under preloads higher than 4mN. The similar trends were observed for displacements δ at the preload. Displacement at the preload is the largest for the sample B-E12-VE50 ($\approx$14μm for preload 0.5mN). Samples VE50 and P-VE50 have almost equal displacement at preload values ($\approx$10μm for preload 0.5mN), and the sample B-E12 under the same preload has considerably smaller value than that of other samples ($\approx$6.8μm). To a first approximation, the contact radius (a) is geometrically related to the depth of penetration or the displacement (δ) by $a = \sqrt{R^2 - (R - \delta)^2}$, where R is the probe radius. It is assumed that there is no meniscus raise of the PDMS around the contact with the probe. We compared the estimated values with the experimental values determined from the bottom view image. The measured contact area is always larger than the calculated one by 1.2-1.3 times because of the viscoelastic nature of the materials. This method gives an estimate of the contact area for the graded structure B-E12-VE50 for preloads higher than 4mN. This method has been used by Paiva et al as well [150].

Second column of Figure 3-9 shows the bottom view images of the contact at the pull-off point; third column shows the bottom view images of the contact at an arbitrary point after pull-off. As expected, during the unloading, significant amount of fingering instabilities and undulations were developed for samples VE50, P-VE-50, and B-E12-VE50 but not for the elastic sample B-E12. Comparing the three viscoelastic samples, the extent of undulation for the sample B-E12-VE50 is more pronounced than the other two. The effective contact zone during the separation is indicated by dashed circles and defined as the area in which 1) the probe and

adhesive are fully in contact and 2) there is no trace of undulation. The effective contact zone is smaller for the sample B-E12-VE50 and the finger instabilities are more developed. In addition, the contact line has been located between the fibrils and not on top of them. The effective contact zone for the sample P-VE50 is remarkably larger than that of the sample B-E12-VE50. It means that the crack propagation is facilitated on top of the sample B-E12-VE50. As the retraction continues, the fingering instabilities of the sample B-E12-VE50 resemble that of the sample P-VE50. However, separation event for the sample P-VE50 takes much longer time than that of the sample B-E12-VE50. The fingers, and also vertical fibrils, on the flat control sample appear to be pinned while they tend to move easily for the new hybrid structure. This can be seen in the force-displacement curves in Figure 3-7 for the mentioned samples. While the retraction trail for the sample B-E12-VE50 shows only a slight slope change, it undergoes a huge strain hardening for the sample P-VE50. The fourth column shows the surface deformation left after the complete separation. The probe retraction from the sample VE50 induces a moderate trace of plastic deformation. Likewise, separation from the sample P-VE50 is occurring with a greater level of plastic deformation which is easily visible after breakage; in contrast, there is no discernible plastic deformation on sample B-E12-VE50.
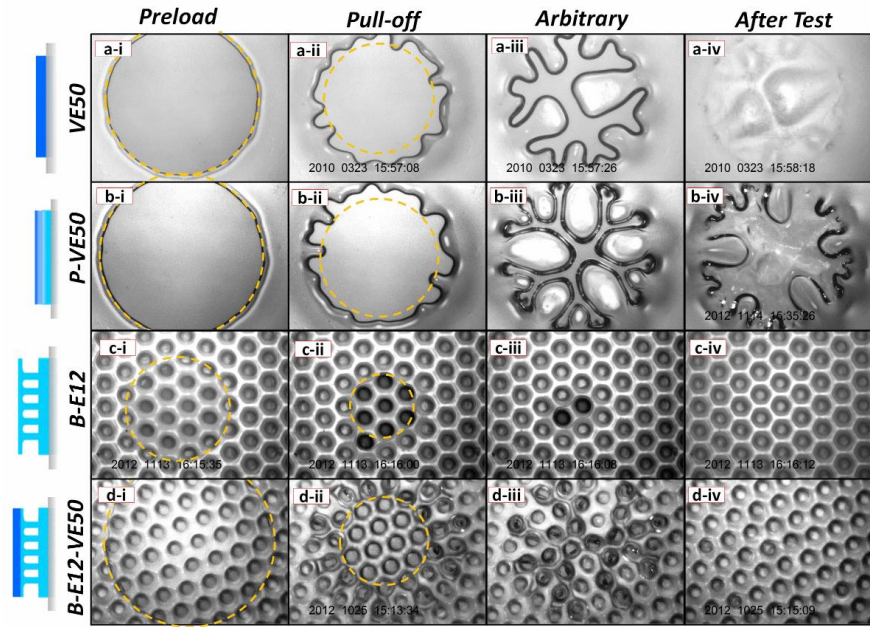
Figure 3-9. Bottom view images of the contact at (i) preload point, (ii) pull-off point, (iii) an arbitrary point after the pull-off, and (iv) after indentation test for (a) sample VE50, (b) sample P-VE50, (c) sample B-E12, and (d) sample B-E12-VE50. The experiments have been performed under 0.5 mN preload.

3.3.3 Preload dependence behavior of BFGAs

It has been previously reported that the adhesion and mechanical properties of homogenous flat samples, either elastic or viscoelastic, have a limited dependence on preload [151]. Preload dependence becomes more important if the material has a graded nature. Functional graded materials have been shown to have variation of the mechanical properties along the depth from their surface. For instance, modulus of elasticity of the power law graded materials are known to vary with distance from the surface [152]. Biomimetic fibrillar adhesives have been treated as the graded materials by Yao and Gao [153,154]. The preload dependence of mechanical and adhesive properties of these adhesives has been well studied in the literature [50,155]. Figure 3-10 shows the variation of the pull-off force with preload for the four adhesive structures. The pull-off forces for all samples increased as the preload increased. The functionally graded structure B-E12-VE50 has a much higher pull-off force and greater dependence on the preload than that of the other three. This significant preload dependency can be attributed to the presence of both micro-pillars and the top viscoelastic layer.
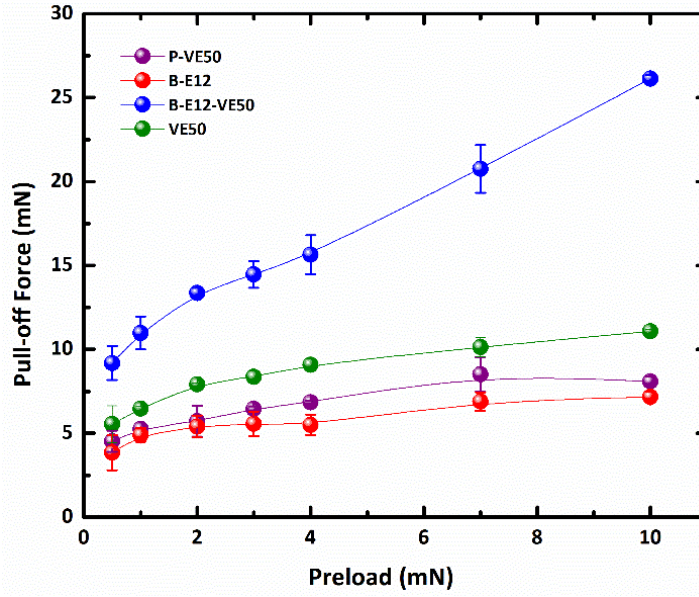
Figure 3-10. Variation of pull-off force vs preload for the four different samples indicating their preload dependence behaviors

3.3.4 Adhesion energy and compliance analysis of BFGAs

While pull-off force is one of the most commonly used indicators of the surface adhesion, preload dependence of the pull-off force for biomimetic fibrillar structures make it difficult to use [155]. For this reason, the work of adhesion can be calculated as a relatively universal value to indicate the adhesive properties of a material. In an indentation test, the work of adhesion is defined as the hysteresis or energy dissipation per change in the area of the contact. The hysteresis is defined as the difference between the stored strain energy due to inter-surface attraction and loading, and the work required separating the contacting surfaces during the unloading.

$$U_{Hys} = U_1 + U_2 = \int_0^{d_{max}} F d\delta + \int_{d_{max}}^d F d\delta = \oint F d\delta \qquad (3-1)$$

U_1 is the strain energy stored in the system. U_2 is the required energy to separate the probe from the surface, or open a crack at the interface. d_{max} is the displacement or depth of penetration of the probe at preload; d is the displacement of the failure point. For an entire indentation process, the contact area at the starting and the failure points are equal to zero and the total work of adhesion can be shown as:

56

$$W_{adh} = \frac{U_{hys}}{\Delta A} = \frac{\int_0^{d_{max}} F d\delta}{A_{max} - A_0} + \frac{\int_{d_{max}}^{d} F d\delta}{A_d - A_{max}} = \frac{\oint F d\delta}{A_{max}} \qquad (3-2)$$

Since we have performed the indentation tests with different preload values, both the contact area at preload and hysteresis vary. Thus, the slope of the linear fit to the U_{Hys} vs ΔA data provides the universal work of adhesion value. A similar reasoning has been used in reference [156] to obtain the work of adhesion for fully elastic systems. Figure 3-11 shows the variation of the hysteresis against preload and consequently contact area for the tested samples. It reveals an approximately linear relationship. Thus, the work of adhesion can be determined from the slop of the linear fitting lines.

It is well known that the critical release energy rate is a multiplicative function of thermodynamic work of adhesion, or the quasi-equilibrium energy release rate at $v \approx 0$ ($\mathcal{g}_0$), and dissipation factors which are dependent on temperature and debonding velocity ($\varphi(T,v)$),, i.e. $\mathcal{g} = \mathcal{g}_0 \big(1 + \varphi(T,v)\big)$. It is believed that the thermodynamic work of adhesion does not significantly depend on the amount of cross-linking agent used in a polymer. Thus, in our experiments, the only origin of alteration in adhesion energy is related to the extent of irreversible energy dissipations. The energy release rate of a fully cured and purely elastic PDMS film estimated through JKR fitting was found about $0.07 J/m^2$ which is greater than its thermodynamic work of adhesion ($\approx 0.044 J/m^2$) [156]. According to Figure 3-11, the work of adhesion for the elastic thin-film terminated micropillars (sample B-E12) is about $0.35 \ J/m^2$ which is higher than that of a flat non-patterned elastic PDMS film. This value is very close to the value obtained for a similar structure in ref [156]. This increase is attributed to the combination of mechanisms such as crack trapping and enhanced compliance. The work of adhesion for the viscoelastic film on the glass (sample VE50) is $0.77 \ J/m^2$ as a result of the more dissipative nature of the viscoelastic sample. The adhesion energy for sample P-VE50 is greater than VE50. Larger contact area and higher compliance of the backing material are the main reasons for this difference. Also, this leads to increment of the confinement ratio, rendering the separation process toward an unstable more dissipative event. Finally, the adhesion energy for the sample B-E12-VE50 is the highest. Even the values obtained by superimposing the work of adhesion for both pairs of (B-E12, VE50) and (B-E12, P-VE50) is lower than the work of adhesion obtained for the sample B-E12-VE50. This can be attributed to the synergistic effect of compliance of the

backing material and also the elasticity of the top layer on the total adhesive properties of the system.
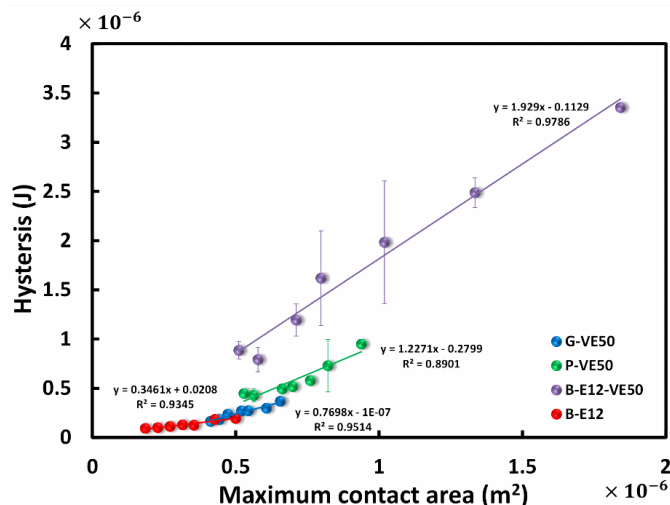
Figure 3-11. Plot of the hysteresis versus contact area for tested samples underwent different preloads during the indentation tests; slope of each line indicates the work of adhesion for each tested sample.

Enhancement of compliance has been reported as one of the main advantages of the biological fibrillar adhesives [60,67,156,157]. Enhanced compliance in such adhesive systems leads to increment of effective contact area and accordingly increase in effective surface forces during the interaction with mating surfaces. It has also been shown that the increase of compliance can amplify the adhesion hysteresis and energy [156]. Nadermann et al investigated the effect of contact compliance on the performance and strength of biomimetic film-terminated structures[143]. They showed that the use of arrays of micro-fibrils underneath an elastic PDMS thin film increases the compliance of the interface. Following this work, we hypothesize that the compliance of the biomimetic film-terminated structure can be further enhanced using a viscoelastic top layer. To verify this idea, we calculated the contact compliance and Young's modulus since they are the determining parameters for predicting the efficacy of an adhesive material.

Firstly, the effective Young's modulus was calculated based on the Hertz model. The fitting/numerical results deviated from the experimental results, particularly for the samples with viscoelastic top layer at small preloads. In fact, surface interactions at low preloads caused a remarkable deformation of the surface and accordingly snap-in force, hindering the use of Hertz model to predict the correct effective Young's modulus. The JKR theory includes the surface

interactions but it cannot be directly used for measurement of the elastic modulus of viscoelastic materials; modified JKR models have been developed for viscoelastic materials which involved complicated mathematical treatments [156,158–160]. Given the limitations of the Hertz and JKR models for the loading portion, we opted to use the unloading portion of the indentation cycle. In detail, to calculate the Young's modulus and compliance, the slope of the load-displacement curve and the Boussinesq definition of the compliance at the start of the unloading point were used, where the contact area is almost pinned and constant. This approach is essentially the same as the one which Oliver-Pharr theory used. That is, the effective Young's modulus can be calculated from the unloading portion of the indentation cycle by relating the stiffness of the material ($S = 1/C$) to the pinned contact area at the vicinity of the unloading point and reduced Young's modulus [161–163]. One main aspect of the Oliver-Pharr theory is the approximation of the unknown contact area based on the indentation depth and total displacement. Furthermore, veracity of this theory for both non-polymeric materials undergoing plastic deformation and viscoelastic polymeric materials has been reported in ref [162]. Since the contact areas for most of our samples are known, the use of the Oliver-Pharr's approximation is not necessary. However, the similarity of our approach to theirs makes it reasonable to calculate the compliance at the starting point of the unloading indentation curve and the use of the Boussinesq definition. Herein, the compliance (C) for a fixed contact area is defined as the change in displacement per unit force ($C = d\delta/dF$). This value is obtained by finding the slope of the unloading curve at the point where the unloading starts. Figure 3-12 shows the load-displacement curves for indentation of sample B-E12 with different preloads. The similar graph can be obtained for other samples tested in this study. The unloading cycles in our experiments were linear for a remarkable range of retraction distance. This situation makes unnecessary the use of Oliver-Pharr theory which is based on power law fitting to the unloading curve [161,162].

To quantify the effective Young's modulus of our samples we used the Boussinesq definition of the compliance with a constant contact area upon loading as follow [156]:

$$C_B = \frac{1}{2aY^*} = \frac{1}{2\sqrt{\frac{A}{\pi}}Y^*} \tag{3-3}$$

In this equation a is the contact radius; Y^* is the combined effective Young's modulus of substrate and probe that can be related to the elastic modulus of each side by the following equation:

59

$$\frac{1}{Y^*} = \frac{(1 - \sigma_1{}^2)}{Y_1} + \frac{(1 - \sigma_2{}^2)}{Y_2} \qquad\qquad (3-4)$$

, where σ shows the Poisson ratio of each side of the interface. As our probe is fused silica the equation (3-4) reduces to the form of $\frac{1}{Y^*} = \frac{(1-\sigma_1{}^2)}{Y_1}$. We also assume $\sigma = 0.5$.
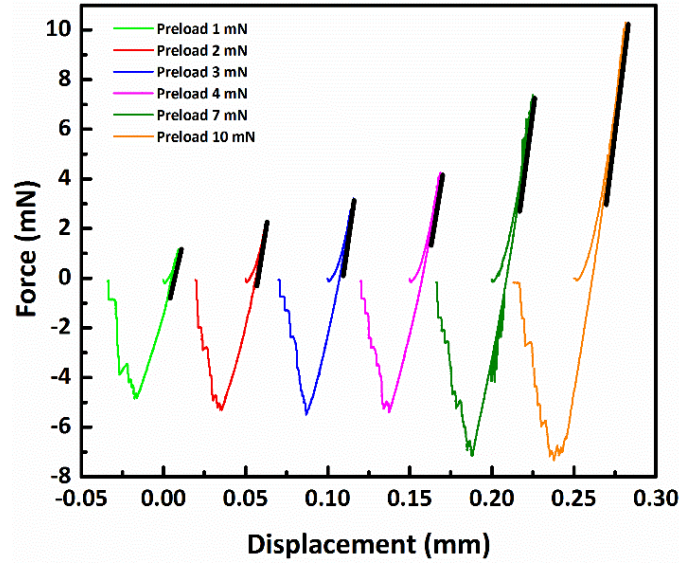
Figure 3-12. Force vs displacement curves of the sample B-E12 under different preloads ranging from 0.5mN to 10mN. The slope of the unloading curve at the preload has been used to estimate the compliance.

Variation of the compliance and Young's modulus with preload is shown in Figure 3-13(a-b). The compliance of the sample B-E12-VE50 is the highest and dramatically decreases as the preload increases at low preloads (< 3mN). The compliance of the samples B-E12 is less and also dramatically decreases as the preload increases at low preloads (< 3mN). In contrast, the compliance of P-VE50 and VE50 are much lower and gradually decrease with preloads. At higher preloads (> 3mN), the contact compliance of the samples VE50 and P-VE50 and B-E12 continued to gradually decrease. But for the sample B-E12-VE50, the compliance only slightly decreased for the preload between 3mN to 7mN and started to increase at higher preloads (10mN). The Young's modulus shows the opposite trend to the compliance as predicted by the equation 3-3. It is interesting to note that the Young's modulus of the sample B-E12-VE50 is in the same order of magnitude of a typical pressure sensitive adhesive as described by the Dahlquist criterion [164]. It is also informative to notice that adding the micropillar to the sub-

surface layer of the viscoelastic film reduced the effective modulus by 6 times to have a value of 1.5 x10^5 Pa. This analysis confirmed that the biomimetic fibrils increase the contact compliance and verified that the viscoelastic top layer further increased the contact compliance. Note that the compliance and Young's modulus of the elastic film-terminated fibrillar interfaces and arrays of simple micro-fibrils have been theoretically modelled by Shen and Noderer et al [145,156]. Assuming the additive contributions of each layer to the global structure of the graded adhesive, it might be interesting to apply these existing models to predict the contributions of each layer and the influence of structural parameters. However, we have observed a significant interplay between the top viscous layer and the base micropillars as discussed in the following sections, which hinders the analysis of the whole structure using the existing analytical models and requires more detailed analytical and numerical studies.
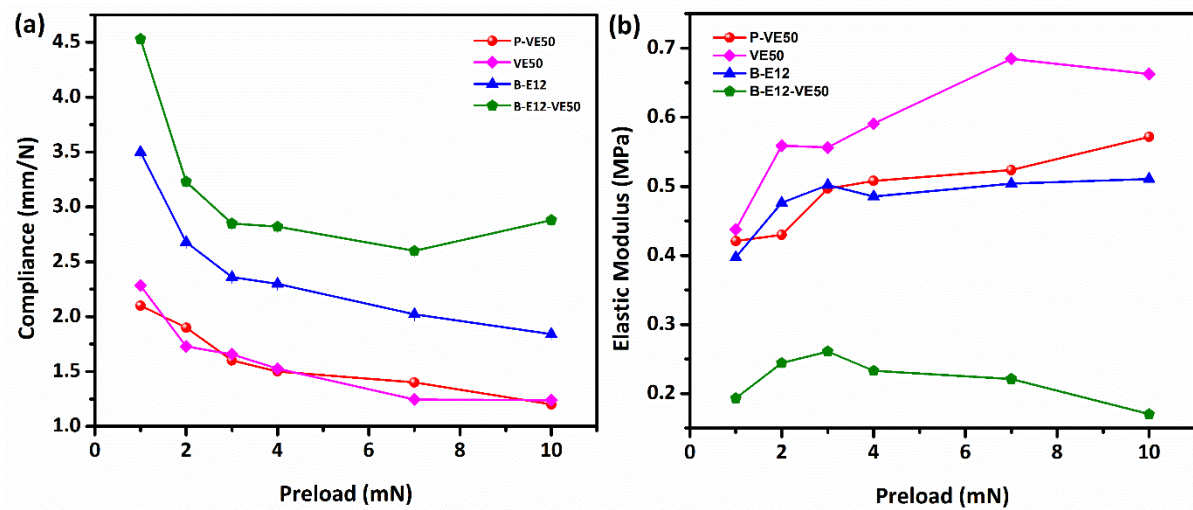
Figure 3-13. Variation of (a) the compliance and (b) elastic modulus versus preload

3.3.5 Synergetic interactions between surface fibrils and the viscoelastic top layers

It is known that buckling of fibrillar structures can increase the compliance [156]. Thus, we further investigated the possible bending and buckling of biomimetic fibrils at increased preloads. Figure 3-14 shows typical bottom-view images for the sample B-E12-VE50 at increased preloads. Examination of the recorded videos of the contact deformations revealed that the minimum preload for bending the pillars in the sample B-E12-VE50 is around 3mN. In contrast, a minimum preload of about 25mN is required to induce visible bending of the pillars in sample

B-E12. We approximated the weight of a 50μm thin PDMS layer for a unit of area (≈0.5mN/m^2). This result shows a negligible extra weight on top of the fibrils. Thus, there should be another mechanism causing the bending and buckling of the pillars than the extra weight induced by the viscoelastic top layer. This suggests the possible synergetic interactions between the fibrils and viscoelastic top layers.
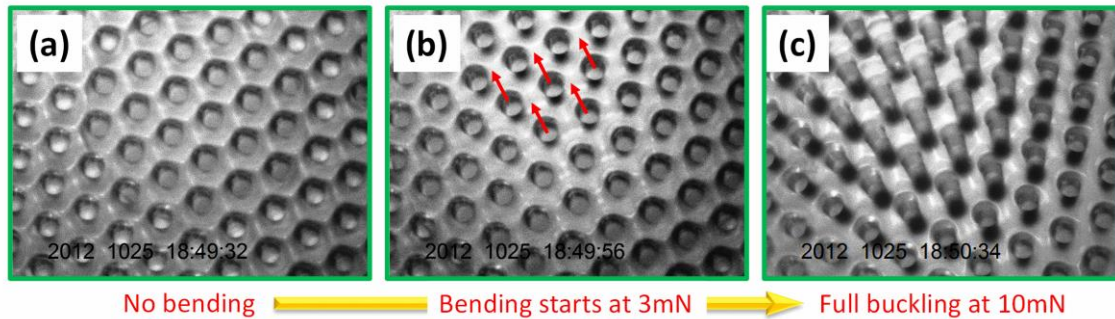
Figure 3-14. Bottom view images of the pillars in the sample B-E12-VE50 during an indentation test (a) no bending, (b) slight bending at preload of 3mN, and (c) full buckling at preload of 10mN.

The enhanced compliance for the new-hybrid structure can be attributed to two mechanisms. First, because of the viscoelastic nature of the top layer, it deforms laterally on the surface under the preload, causing interfacial shear stress to the underlying elastic film. If the viscoelastic top layer is completely diffused into the elastic backing layer, it forms an interphase. Thus, the no-slip condition governs the interfacial shear stress. In such a case, the only possible reason for the facilitated bending of the pillars can be related to the deformation of the intermediate elastic film induced by Poissonian deformation of the viscoelastic top layer.

The existence of a second scenario is possible as the elastic layer is fully cross-linked and the diffusion at the interface might be limited. It is known that there exists a slippage of the viscoelastic polymers confined between two substrates. This is the case even for compression of a polymer melt in a confined geometry that is chemically modified with the identical polymer. Although Brochard and de Gennes reported that the identical grafted chains on confining substrates can hinder the polymer slippage remarkably, in certain stress rates the conformation of the grafted chains shift from "coiled" to "stretched" , causing polymer slippage [165]. In our experiments, a significant amount of shear slippage is expected at the interface between the

viscoelastic and elastic layers. This shear slippage can result in deformation of the elastic film laterally and consequently bending of the fibrils as illustrated in Figure 3-15.

Moreover, the extent of the polymer slippage at the interface is affected by both thermomechanical properties of the polymer and surface properties of the substrate. The static and dynamic friction between the polymer and substrate hinders the slippage and flow of the viscoelastic material [166–168]. But the softness of the polymer facilitates its slippage on the substrate. This idea is in accordance with Brown's observation that the interfacial shear stress and slippage strongly depends on the segment mobility on the slipping materials. Elastomers have greater segment mobility on their surface due to the presence of flexible polymer chains, while the glassy polymers are deemed as materials with immobile segment or less mobile chains. It has been shown that the slippage of the polymer surface is remarkably facilitated for the surfaces with greater segment mobility [169]. The slippage results in the less adhesion force of a viscoelastic material laid on a substrate with higher segment mobility. The lower pull-off force and higher contact area for the sample P-VE50 comparing to that of the sample VE50 can be explained by this fact. For the graded adhesive structure B-E12-VE50, the presence of micropillars at the base of the sample may have increased surface mobility and the slippage, which in turn enhance the bending and buckling of the micropillars at low preloads. This synergetic interaction resulted in higher pull-off force and adhesive energy comparing to that of P-VE50.
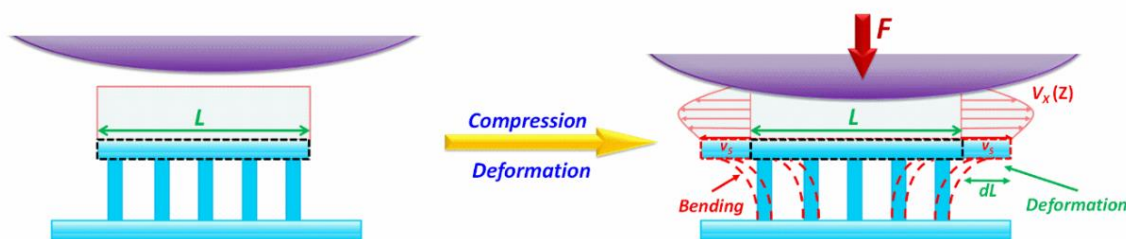
Figure 3-15. The interplay of the top viscous layer and base micropillar during the compression: the slippage of the viscoelastic polymer stretched the intermediate layer which subsequently induced the bending deformation of micropillars.

Finally, it is worthwhile to look at the gecko and tree frog-inspired hybrid adhesive structure from the perspective of functionally graded materials and discuss the technical implications. There exists a myriad of natural substances having outstanding bulk resistance to

cracking, deformation, and damage, thanking to their micro-structured or porous-based gradations. Bamboos, bones, and plant stems are the common examples of such structures with the strongest elements located where the stress is the maximum [152]. Particularly, the Humboldt squid's body is composed of an extremely stiff beak embedded in a soft buccal envelop. When hydrated, the chemical gradient in the beak renders a gradient in stiffness ranging two orders of magnitude from the top to the base [170]. It has been shown such gradients in chemical and mechanical properties of a structure are able to hamper the cracking, deformation, and damage through concentrating the stress to the joints between mechanically dissimilar materials [152,170]. In the other words, the extent and mode of crack growth can be intensified or reduced across an interface by alteration of the elastic properties underneath the free surface of the material. Therefore, graded materials have attractive potentials as materials resistant to contact damage [152]. Contact mechanics study of both elastic and plastic graded materials has been facilitated by depth-sensing indentation [153,154,171–174]. Gradient in the chemical, geometrical, and mechanical properties along the depth axis is also believed to regulate the adhesion properties of materials [172]. Thus far, there is only a few theoretical studies on the mechanics of elastic graded materials considering adhesive contacts [154,172]. Interestingly, bioinspired fibrillar structures can be treated as graded materials. For instance, Yao and Gao developed an interfacial crack model and showed propensity of the elastic bioinspired fibrillar adhesives, as graded materials, to increase adhesion robustness and flaw tolerance [175]. While the domain of these investigations is limited to only elastic graded materials, there is an appeal to elaborate more about plastic or viscoelastic graded materials [152,173].

The reported bio-inspired graded adhesive structures in this work composed of three components: an array of elastic micropillars at the base, a thin elastic intermediate layer and a viscoelastic top layer. The biomimetic fibrillar interface functions as a spring foundation storing the elastic energy during the bonding. It dramatically increases the compliance of the system both before and after bending and buckling of the pillars. The stored energy in the pillars can be retrieved during the separation which facilitates the crack propagation at interface instead of cohesive failure. The intermediate elastic layer facilitates integration of the viscous layer on top of the biomimetic fibrillar foundation and transfer the shear stress from the top to the base micropillars. The viscoelastic top layer dissipates a large amount of energy during the separation because of the bulk deformation and instabilities, which induced a shear stress at the interface and enhanced the bending and buckling of the fibril. This synergetic interaction among the three

64

components resulted in higher pull-off force and adhesive energy, higher compliance and resistance to cohesive failure. Other than the scientific insights obtained in this complex system, the introduction of the concept of functionally graded materials to the biomimetic adhesives may provide effective ways for the development of soft temporary adhesive materials for effective adhesion and bonding processes used in biological and mechanical systems' applications, for instance, the emerging soft electronic devices that are foldable and able to stick to biological tissues.

3.4 Summary

We made a bio-inspired graded adhesive structure composed of an array of elastic film-terminated micropillars at the base and a thin viscoelastic film of the same material on top. A systematic investigation of this bio-inspired graded adhesive structure was performed in comparison with three control adhesive materials: viscoelastic film coated on a glass substrate, viscoelastic film coated on a soft elastomer, and elastic film-terminated micropillars. Indentation measurements show that more energy is consumed in crack initiation and less energy is consumed in crack propagation during the separation of the functionally graded adhesive structure than that of a simple viscoelastic film. This facilitates the adhesive mode of separation (or inhibits the cohesive failure of the viscoelastic film) and leads to an adhesive material with higher structural integrity. The evolutions of adhesive contact area and separation instabilities during the indentation were examined, revealing a large amount of fingering, cavitation and crack trapping phenomena. The preload effects on the adhesive pull-off force and work of adhesion were investigated along with energy and compliance analysis. These studies showed a remarkable increment of pull-off force, work of adhesion, and compliance. The significant compliance of the new structure was attributed to the effect of interfacial slippage on the bending and buckling of the fibrils underneath the viscoelastic layer. Accordingly, higher amount of energy dissipation was observed for such structure. Retrieving of the elastic energy stored in the fibrils underneath a viscoelastic layer facilitated the crack propagation resulting in the less bulk deformation during the separation for the graded structure when it is compared to that of the control samples. Overall, this work demonstrated that the synergetic combination of gecko-inspired micro-pillar structure with the viscoelastic top layer resulted in a functionally graded adhesive material delivering high adhesion, high compliance and resistance to cohesive failure.

Chapter 4
Smart Muscle-Driven Self-Cleaning of Biomimetic Structures from Liquid Crystal Elastomers†
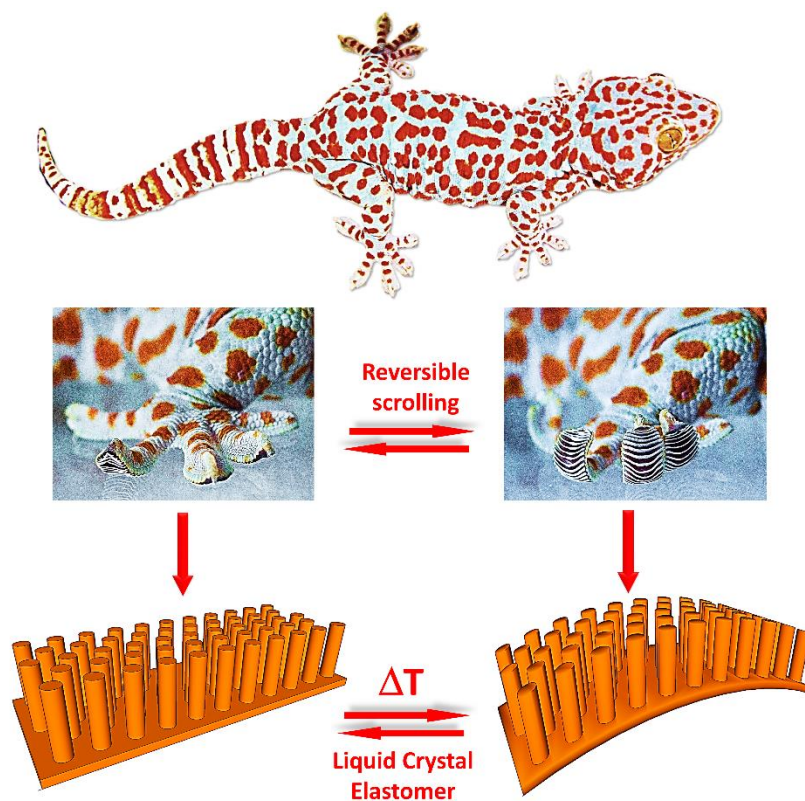
4.1 Introduction

For more than a decade, strong and smart climbing ability of geckos has been the subject of extensive research. Geckos can readily attach/detach their toe pads to/from almost any surface in fractions of a second repeatedly without any extra attempt for combing, thanks to their switchable adhesive, superhyrdrophobic and self-cleaning nature [45]. From the anatomical point of view, both skin and muscles of gecko toe pads are engaged in creating this extremely efficient adhesion and self-cleaning ability. At the skin level, hierarchical micro- to nano-fibrils on gecko toes promote compliance, facilitate intimate contact and maximize omnipresent van der Waals interactions with mating surfaces [43,176]. The fibrillar surface structures also bestow a remarkable anti-fouling property, so-called Lotus leaf effect [177]. However, certain muscular motions such as adduction/abduction and rotation dictate the fast adhesion switchability between attachment and detachment [178]. That is, the toe pads can attach to and detach from mating surfaces when extending forward and scrolling backward, respectively. Likewise, dynamic self-cleaning crucially depends on distal-to-proximal peeling motion induced by digital hyperextension of toe pads at detachment [179]. In fact, reverse scrolling of the toes allow not only detachment from the mating surface with a trivial force [176,180], but also enough acceleration to dislodge dirt particles [179].

To date, numerous types of synthetic dry fibrillar adhesives have been fabricated. Some are based on micro- or nano-pillars with different shapes bundled in single or multi levels and others are based on film-terminated or bridged micro-fibrils [1,46,51,52,54,55,57,181]. The majority of the existing works address the requirements for strong and directional adhesion, super-hydrophobicity and self-cleaning, but only for static and isolated structures. Also, a few studies focus on external control and switchable adhesive properties of isolated dry fibrillar adhesives. In this regard, much effort has been devoted to tuning the adhesion and wetting by altering the surface topography upon exposure to external cues such as heat, light, electric and magnetic fields. The outstanding examples are based on the use of MEMS [182], shape-memory polymers [183,184] and alloys [185], responsive composites [186], and more recently, liquid crystal elastomers [129,130,187,188]. However, in contrast to synthetic adhesives, switchability of adhesion and self-cleaning in natural gecko toe pads is essentially muscle-driven and the surface topography is rather constant. Only a few publications are inspired by the muscle-driven external control of adhesion and wetting by three-leg clamps, pneumatic soft grippers, and mechanical poking

[96,101,189]. Recently, Guo and coworkers reported their effort to electrically regulate dry fibrillar adhesion using shape shifting ion-exchange polymer-metal composites [190]. However, their elaborate fabrication technique provides only low deformation amplitudes. None of these works allow a large range of remote control of adhesion and wetting.

LCEs and LCNs are interesting examples of active materials deemed as artificial muscles with extends of elasticity and contractility [191]. Benefiting from features of both rubbers and liquid crystals, LCEs possess reversible shape shifting characteristics. Their practical advantages compared to other responsive materials stem from their wide-range of mechanical properties (from soft LCEs to stiff glassy LCNs), larger actuation amplitude, and versatile sources of stimulation, such as heat, UV, and electrical fields. These make LCEs and LCNs outstanding candidates for use in different technological applications such as MEMS and responsive surfaces [3,192,193]. A great number of techniques have been published to study stimuli-responsive deformations of LCEs, ranging from simple bending actuators to accordion-like ribbons and sophisticated voxelated 3D structures [118,194,195]. Microfabrication techniques have been employed to make various 2D and 3D micro-structures from LCEs and LCNs [11,187]. However, active LCEs have never been utilized as a muscle prototype conjugated with biomimetic fibrillar structures. Use of micro-patterned LCE-based systems might have several advantages over other reported techniques such as less external perturbation due to their complete remotely controllable nature. Also, LCEs with different mechanical properties, modes and amplitude of deformation can be pre-designed based on the formulation of the system.

In this chapter, reversible shape shifting characteristics of a hybrid aligned LCE has been exploited to mimic muscular motions of gecko toes. Integrative soft-lithography is used, for the first time, for micro-patterning of an active LCE layer. The proposed structure is made by integration of a splayed nematic side-chain LCE film, as the active backing material, and a passive micropillar layer from the same LCE material. This reduces the chemical mismatch at the interface and prevents delamination during deformation. By varying the thickness of the splayed LCE backing layer, different modes of deformations, such as bending and twisted bending could be achieved to mimic the motions of gecko toes. These results are potentially valuable for fabrication of switchable dry adhesives with dynamic self-cleaning properties.

4.2 Experimental

4.2.1 Synthesis of the LCE and fabrication of LCE micropillars

Figure 4-1(a-b) show a schematic view of the fabrication process along with monomers used in our study. ITO-coated glass plates were cut into 2.5cm by 2.5cm squares. To render planar molecular alignment, glass slides were coated with 10nm PI-2550 (HD Micro Systems) layer, baked and rubbed with velvet cloth in one direction. To induce homeotropic surface anchoring, glass slides were coated with 10nm of an alignment polymer SE-1211 (Nissan Chemical Industries, Ltd) and baked without rubbing. Planar cells were assembled using two planar treated glass slides placed anti-parallel to each other. Splay cells were made by placing one planar treated and one homeotropic treated glass slides on top of each other. PET Mylar films were used as spacers between the glass slides to control the thickness, ranging from 65μm to 288μm. Paper clamps were used to sandwich spacers between glass slides.

Monomer M1, 4-(6-Acryloxy-hex-1-yl-oxy)phenyl 4-(hexyloxy)benzoate (T_{NI}=64) and monomer M2, 1,4-Bis[4-(6-acryloyloxyhexyloxy)benzoyloxy]-2-methylbenzene (T_{NI}=113) were purchased from Synthon Chemicals and used as received. A mixture of monomer M1 as mono-functional mesogen (87.12%wt), M2 as bi-functional mesogenic cross-linker (11.88%wt) and Irgacure®651 as photo-initiator (1%wt) was prepared. The mixture (T_{NI}= 65) was melted to its isotropic phase at 95^{0}C and injected into the capillary cells. The filled cells were cooled down (~1^{0}C/min) to the mixtures' nematic temperature (~53-55^{0}C) followed by photo-initiated cross-linking by 365nm UV light (Blak-Ray™ Model B-100AP/R) for 30 min. Then the cells were cleaved while LCE films were still attached to the planar glass slide. To study thermal-actuation of bare LCE films, freestanding films of 1.3mm length and 2mm width were cut and separated from glass using a razor blade.

Arrays of micro-holes (15μm diameter, 68μm height and 30μm center-to-center spacing) were replicated from a Si wafer master mold with positive patterns by casting and curing of a liquid PDMS with 10%wt resin to cross-linking agent ratio (Sylgard 184, Dow Corning). Prior to the LCE micro-fabrication, PDMS molds were coated by gas phase deposition of self-assembled monolayers of FDTS (heptadecafluoro- 1,1,2,2- tetra hydrodecyl) trichlorosilane, Gelest) to reduce sticking of the LCE micropillars during casting. PDMS master mold was attached to a glass substrate as a stiff backing material to control the thickness of the fabricated

structures. To ensure the uniformity of the micro-pillars in their sizes, 13 to 15mg of solid LCE precursor mixture was sandwiched between the PDMS mold, and previously prepared splayed LCE attached to the glass substrate using paper clamps. The whole assembly was heated up to the isotropic temperature (95$^{\text{o}}$C) so as to melt the LCE precursor and fill the holes. Pressure produced by paper clamps squeezed excessive LCE precursor out of the film. After cooling to nematic temperature (~53-55$^{\text{o}}$C) cross-linking took place for 30 min. Finally, the PDMS mold was peeled off gently and micro-patterned LCE films were used either attached to or detached from glass for further studies. Again, to reduce surface energy and increase hydrophobicity of the samples, the fabricated LCE micropillars were treated with FDTS. Geometrical features were characterized using a white light interferometer (Rtec Instruments, USA).
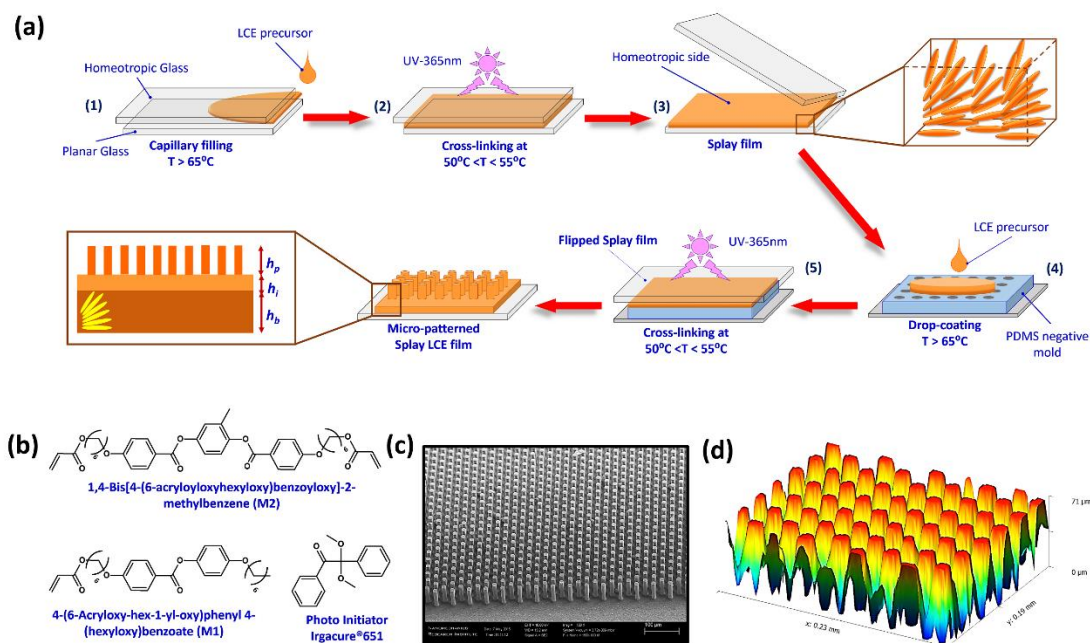
Figure 4-1. The fabrication and characterization of the splayed LCE micro-pillars. (a) Schematic view of the fabrication process, (b) molecular structures of the mesogen and photo-initiator used in LCE precursor, (c) SEM and (d) optical interferometer images of the fabricated LCE micro-pillars

4.2.2 Contact angle measurements

Sessile drop technique was used for contact angle measurements. A custom made apparatus was employed for this purpose. Droplets of water and glycerol with volumes of about 5μL were deposited on the samples with the rate of 20mL/hr. At least four images of the liquid droplets deposited on the surfaces were analyzed to extract the contact angle at the three-phase

contact line. Thermo-responsive experiments were conducted on a heating stage to trigger deformation of the samples during the measurement.

4.3 Results and Discussion

4.3.1 Fabrication and characterization bare and micro-textured LCN thin films

LCE films with different thicknesses were fabricated via capillary filling of a glass cell followed by photo-polymerization at LCE precursor in the nematic phase (Step 1 to 3 in Figure 4-1). Differential Scanning Calorimetry (DSC) analysis of the LCE films showed a broad glass transition temperature (T_g) at around 20**°**C, similar to results reported in ref [137]. The nematic–isotropic phase transition temperature (T_{NI}) of the type of LCE used here cannot be accurately determined similar to other types of LC diacrylates [196]. However, the examination of the variation of birefringence with temperature shows the emergence of a plateau at about 200**°**C, which might be interpreted as T_{NI} (details in Appendix and Figure A-1). Birefringent values for LCE films with planar molecular alignment were more than twice that of splayed films, confirming successful hybrid alignment of mesogens [194]. Arrays of PDMS micro-holes with 15μm diameter and 68μm depths were used to cast LCE micro-pillars via conventional soft-lithography technique (step 4). The hybrid LCE film were brought in contact with PDMS micro-holes, which were formerly filled with the LCE precursor at the isotropic temperature, and bonding took place by photo-polymerization at the nematic temperature (step 5). Upon reaching the desired cross-linking time, the system was cooled down to room temperature and the PDMS mold was gently peeled from the LCE films anchored to a glass substrate. SEM and optical profiler images confirm perfect replication of the pattern onto the LCE film as shown in Figure 4-1(c-d). Geometrical characteristics of all fabricated samples are tabulated in Table 4-1.

Our fabrication technique creates three distinct geometrical regions along the thickness of the whole structure as shown in Figure 4-1a. Given the initial thickness of the LCE backing layers, h_b, and height of the micropillars, h_p, the thickness of the LCE layer sandwiched between the pillars and the backing layer, h_i, was estimated to be 10±2μm for all samples. Unlike other reported techniques in the literature [129,187], preferential alignment of mesogens in micropillars was avoided to restrict the thermal actuation to only the LCE backing layer.

Table 4-1. Geometrical parameters and mode of deformation of different samples. h_b and h_i represent thickness of the LCE backing layer and intermediate LCE layer. h_p represents height of the pillars.

Sample	h_b (μm)	h_p (μm)	h_i (μm)	Mode of Deformation	$d\kappa/dT$ [$mm^{-1}\kappa^{-1}$]
B-LCE-0	288±6	-	-	Bend	1.1×10^{-2}
B-LCE-1	188±4	-	-	Bend	2.1×10^{-2}
B-LCE-2	95±2	-	-	Bend	3×10^{-2}
B-LCE-3	65±4	-	-	Bend	3.8×10^{-2}
P-LCE-0	288±6	68±2	10±2	Bend	8.4×10^{-3}
P-LCE-1	188±4	68±2	10±2	Bend	1.4×10^{-2}
P-LCE-2	95±2	68±2	10±2	Twist-bend	-
P-LCE-3	65±4	68±2	10±2	Twist-bend	-

4.3.2 Thermal deformation of the micro-textured LCN thin films

The LCE films separated from the glass substrate were usually curled at room temperature due to residual stress built up during polymerization [197]. The curvature $\kappa = 1/r$ (where r is the curvature radius) at room temperature is greater for thinner films of otherwise same LCE composition. The thermal deformations of one-end-fixed LCE films were monitored in a custom-built heating chamber equipped with a CCD camera and a stereo-microscope. The deformation is purely bending for bare samples, as shown in Figure 4-2(a-b). Samples B-LCE-1 and B-LCE-2 become flat upon heating about 35 to 40°C and then the sign of curvature reverses upon further heating until the isotropic phase is reached. This temperature-induced bending deformation of LCE film is due to the alignment dependent lateral expansion coefficients, which are different on the two sides for our hybrid LCE film [194]. In our polyacrylates-based LC networks, the majority of the covalent bonds are parallel to the director [196]. Also, entropy-driven tendency of the chain segments between networks to adopt random coiled conformation is satisfied at increasing temperatures [120]. Therefore, heating leads to a decrease of the order parameter and to contraction along (negative expansion coefficient) and expansion perpendicular to the molecular director (positive expansion coefficient). Accordingly, in a splayed structure, the homeotropic side gives a large in-plane 2D expansion, and the planar side undergoes small in-plane contraction along, and large expansion perpendicular to the molecular

director. The deformation is completely reversible for heating and cooling, with fairly small hysteresis. The thermal bending coefficients $d\kappa/dT$ are found to be 2.1×10^{-2} mm^{-1} K^{-1} for B-LCE-1 and 3×10^{-2} mm^{-1} K^{-1} for B-LCE-2. The magnitude of these thermal deformations are an order of magnitude larger than results published by Mole and Broer (ca. 1×10^{-3}mm^{-1}K^{-1}) for almost twice thinner LCE films thus showing greater aptitude for deformation at lower temperatures [194]. In the framework of 3D incompressible nonlinear elastic theory Sawa et al [198] and Warner et al [199] have derived that the curvature is inversely proportional to the thickness of the flat film $\kappa = \Delta S_d/h_b$, where ΔS_d is the difference in distortional strains at the two sides of the film, which allows comparing curvatures of films with different thicknesses [198].
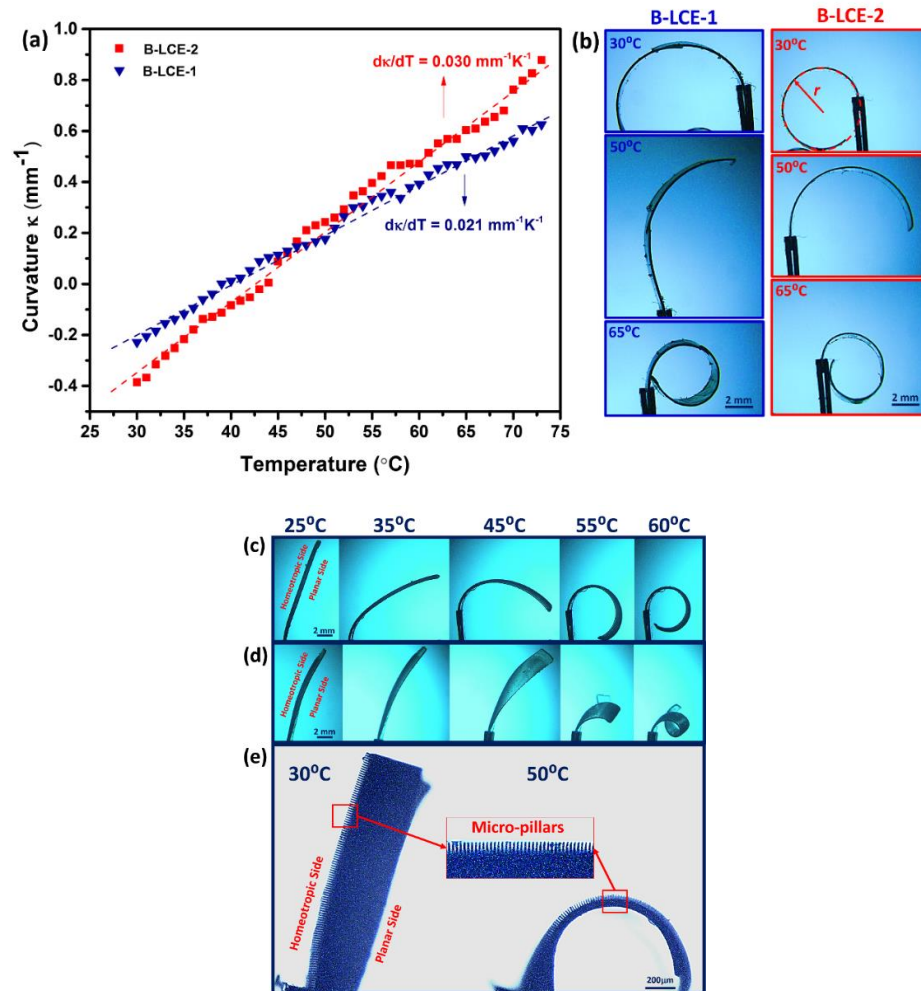
Figure 4-2. Illustration of thermally-induced deformations of the studied LCE films. (a) Variation of curvature vs temperature for bare splayed LCE films; (b) bending deformation of sample B-LCE-1 and B-LCE-2; (c) bending deformation of sample P-LCE-1; (d) twist-bending deformation of sample P-LCE-2; (e) High-magnification side-view of the micro-pillars of the bending P- LCE-1 film

Micro-patterning of the splayed LCE films has a remarkable impact on their mode of deformation. P-LCE-0 and P-LCE-1, where $h_b \gg h_i + h_p$, shows only bending, but with a reduced thermal bending coefficient (8.4×10⁻³, 1.4×10⁻² mm⁻¹ K⁻¹) as compared to B-LCE-0 and B-LCE-1 with the same h_b. This is because the micro-pillared layer does not contribute to the bending, so the curvature induced by the hybrid layer should be reduced by a factor $\mu = h_b/h_{total}$, which in comparison with B-LCE-1 and P-LCE-1 would be $\mu \sim 0.7$, which is close to the observed 1.4/2.1=0.67 value. This indicates that the Young's modulus of the microtextured layer is comparable to that of the continuous layers.

Interestingly, for P-LCE-2 and P-LCE-3, where $h_b \sim h_i + h_p$, the combination of twist and bend occurs leading to a spiral structure. This is significant, as it shows that varying the ratio of the thicknesses of the bend-inducing h_b and the bend-inactive $h_i + h_p$, one can prepare micro-patterned LCE films with deformations ranging from various strength of pure bend to twist-bend, resembling to the muscular motions of gecko toe pads. The appearance of the twist in addition to the bend is similar in nature to the transition from helicoidal to spiral ribbons of twisted nematic LCEs [197]. The underlying physical mechanism leading to the spiral structure is the mismatch between layers of the laminated composite, as described theoretically by Chen et al [200]. Such a mismatch is probably induced by a small pretilt on the homeotropic surface of the hybrid layer that makes an arbitrary azimuth angle with respect to the planar surface. Detailed study of the alignment inside the micropillars and the intermediate LCE layer is described in Appendix A. When the bending energy E_b stored in the hybrid backing layer is large enough, the mismatch is not able to lead to twist. It is known that $E_b = \frac{Y h_b^3 l b}{24 r^2 (1-\sigma^2)}$, where Y is the Young's modulus of the LCE, l and b are the length and width, σ is the Poisson ratio and r is the curvature radius [201]. Since the curvature radius is proportional to the thickness, the bending energy can be approximated as $E_b \approx \frac{Y h_b l b}{24(1-\sigma^2)} \cdot \left(\frac{h_b}{h_{total}}\right)^2$, which increases with h_b, thus explaining qualitatively the appearance of the twist when $h_b << h_{total}$. Summary of thermally-induced deformations of samples P-LCE-1 and P-LCE-2 are illustrated in Figure 4-2(c-e).

4.3.3 Dynamic self-cleaning properties of the micro-textured LCN thin films

Wetting properties of the LCE microstructures were studied using the sessile drop technique on LCE structures kept at constant (room) temperature (passive sample) and while being heated from bottom (active sample). Figure 4-3a shows a drop of water on a flat LCE

74

film. Contact angle (CA) is slightly higher on the homeotropic side than the planar side. However, both values are still larger than 90^0 showing moderate hydrophobic behavior of the LCE film. When the flat surfaces were tilted the water droplet did not slide even when they were turned upside down. This was also the case for the glycerol droplet, as shown in Figure 4-3b.
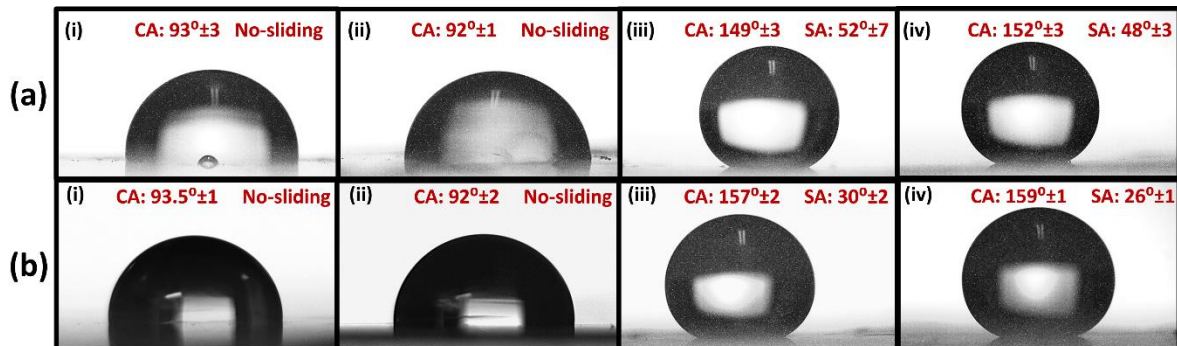
Figure 4-3. Side view images of small droplets on horizontal flat surfaces of passive LCE films. (a) Water droplet; (b) Glycerol droplet; (i) on homeotropic side (ii) on planar side, (iii) on micro-patterned side, and (iv) on a SAM coated micro-patterned splayed LCE film

It is well-known that micro-patterning often results in hydro-or oleo-phobicity of materials [202]. As anticipated, micro-patterning of the flat splay LCE films led to a remarkable increment of CA for both water and glycerol, as seen in Figure 4-3 (iii). The increment became more pronounced for samples coated by a self-assembled mono-layer (SAM) of Perfluorodecyltrichlorosilane (FDTS). The sliding angle (SA) decreased to 48^0 and 26^0 for water and glycerol, respectively. It is worth noting that both liquids left no trace after sliding on the micro-patterned samples indicating non-adhesive nature of liquid-solid contact, similar to Cassie-Baxter regime, at the interface. We also noticed that deliberate manipulation of the experimental conditions such as pressing on the droplet, external vibration, or increasing the size of the droplet may trigger the transition from non-adhesive to adhesive contact (Wenzel state). Thus, we speculate that our experiments are in the metastable Cassie regime. In accordance with our observations, it is believed that micro-patterning of materials with moderate hydrophobicity (CA ≈90^0) encourages liquid-solid contact in a metastable Cassie regime [203].

To demonstrate the self-cleaning ability of the fabricated samples, both the bare and micro-patterned samples were contaminated by glass micro-beads with diameters ranging from 10μm to 400μm. Contaminated samples were first put onto an analog vortex mixer (Fisher

Scientific), set to the medium speed, to mechanically shake off the dirt particles in dry state. ImageJ and a custom developed program were used to calculate the surface coverage by particles. Surface coverage by contaminant particles were reduced from 56% to 22% for the flat samples and from 54% to 0.8% for the micro-patterned samples (Figure 4-4(a-b) ii). The dusted samples were then rinsed with DI water. Less hydrophobicity of the flat sample causes clustering of micro-spheres and their adhesion to the surface (Figure 4-4a iii). In contrast, the micro-patterned sample is remarkably cleaner than the flat sample with only some small particles trapped between the pillars (Figure 4-4b iii). Note that the self-cleaning ability of a micro-patterned surface depends on both the size of contaminant elements and microstructures as particles smaller than the stem diameter and spacing between the micro-fibrils may be trapped [204].
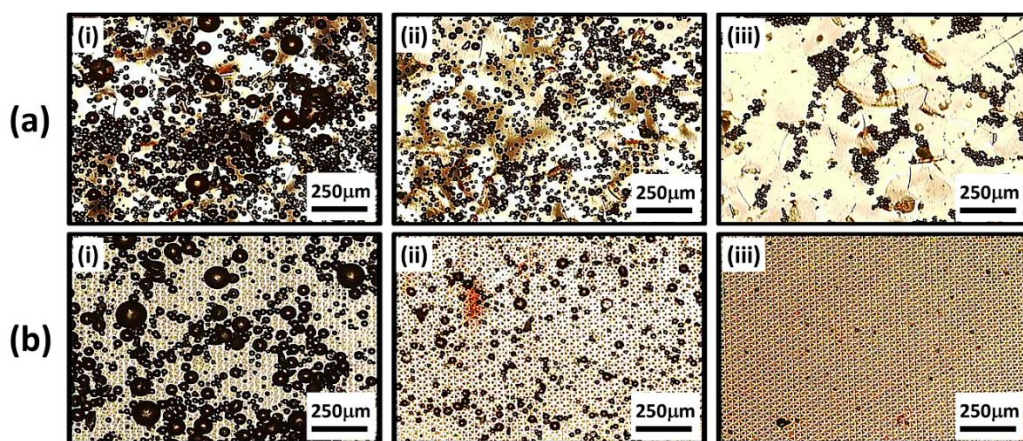
Figure 4-4. Optical microscopy of contaminated samples; (a) bare LCE and (b) micro-patterned LCE; (i) right after contamination, (ii) after mechanical agitation, and (iii) after rinsing with water

Stimuli-responsive properties of LCE samples create a great potential for remote harvesting of their dynamic self-cleaning features. To examine this idea, a droplet of glycerol was poised onto the free standing films of both bare and micro-patterned LCEs. Measurements on active surfaces were conducted only on glycerol that has a boiling point of 290°C to avoid evaporation of the liquid droplet during heating [130]. Due to the absence of any preferential alignment inside the micropillars, no remarkable change in the shape, size and contact angle of the passive micropillars was anticipated at varying temperatures. To determine the possible effects of temperature on the shape, size and contact angle of the passive micropillars, white light interferometry and contact angle measurements were conducted at different temperatures ranging from room temperature to 105°C. A heat-stage was used to control the temperature

during the surface topography and contact angle measurements. Figure 4-5a shows the top view image of a scanned area of 1mm^2 measured at 25^{0}C. Figure 4-5b shows the surface profiles at 25^{0}C and four elevated temperatures (45^{0}C -105^{0}C) for the micropillars under the yellow line in Figure 4-5a. Apparently, the variation of temperature has a minimal effect on the size of the micro-pillars. Additional contact angle measurements at different temperatures were performed, showing negligible effects of heating on the samples' contact angles.
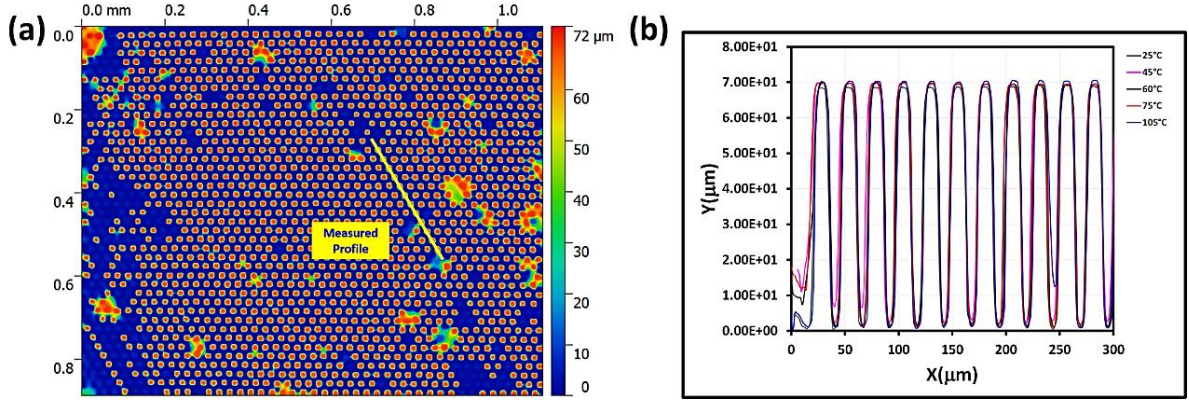
Figure 4-5. (a) Top view image of an arbitrary spot on passive micropillars under an optical profilometer, (b) detailed surface profile of the micropillars measured at different temperatures along the yellow line drawn in (a).

Moreover, we anticipated that heating from the bottom can induce bending deformation to the splayed LCE film backing the passive micropillars. As shown in Figure 4-6a, glycerol droplet sticks to the surface of the bare sample and does not slide off the surface even at high temperatures and curvatures. On the contrary, glycerol droplet finds the shortest path for sliding off the micro-patterned LCE when the thermally-induced curvature reaches the sliding angle (21^0±3) (Figure 4-6b). Samples contaminated as described above were also studied here to demonstrate thermally induced curvature-driven self-cleaning ability. As can be seen in Figure 4-6c, micro-particles are attracted to glycerol droplets, which clean their pathways during sliding.
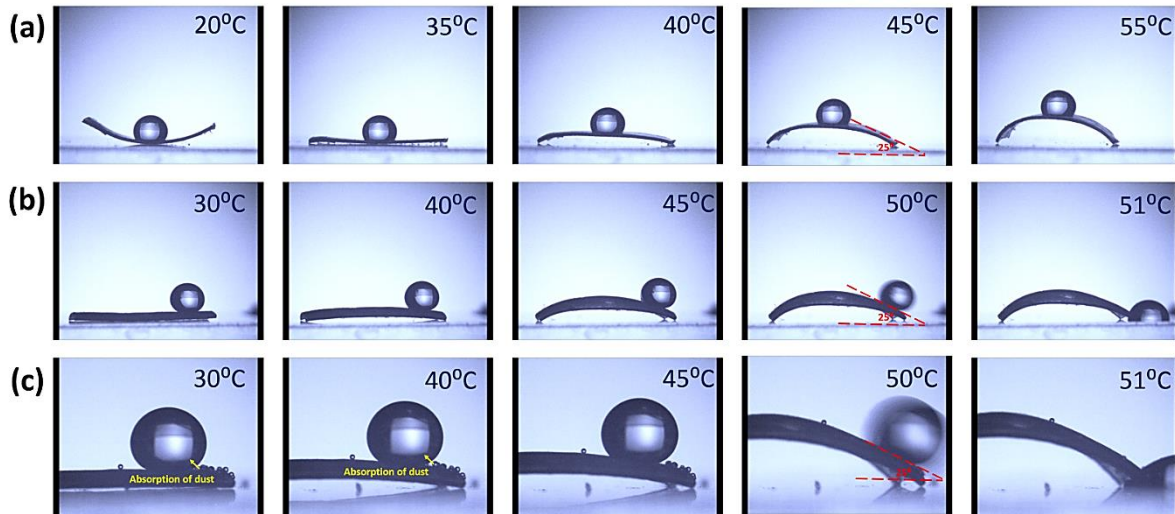
Figure 4-6. Side view images of a glycerol droplet on active splayed LCE surfaces. (a) Bare SAM coated film; (b) SAM coated micro-patterned film; (c) dynamic wet self-cleaning characteristic and dust adsorption by sliding droplet on a SAM coated micro-patterned splayed LCE film.

4.4 Summary

We used integrative soft-lithography of a hybrid aligned LCE to produce muscle-driven actuation of micro-fibrillar structures. Our fabrication technique enabled the LCE to have different modes of temperature-driven deformation. As a key feature of gecko inspired structures, dynamic self-cleaning properties of the LCEs have been investigated. It is shown that self-cleaning properties of such structures can be remotely exploited when triggered by an external stimulation. Results in this communication can be a stepping stone for development of new generation of dry fibrillar adhesives with more resemblance to actual gecko toe pads that can be remotely controlled. Although only thermo-responsive LCEs are used in our work, a great number of external cues such as UV, electrical field and humidity can be used to emulate similar deformation and function.

Chapter 5
Thermally Active Liquid Crystal Network Gripper Mimicking the Self-Peeling of Gecko Toe Pads [†]
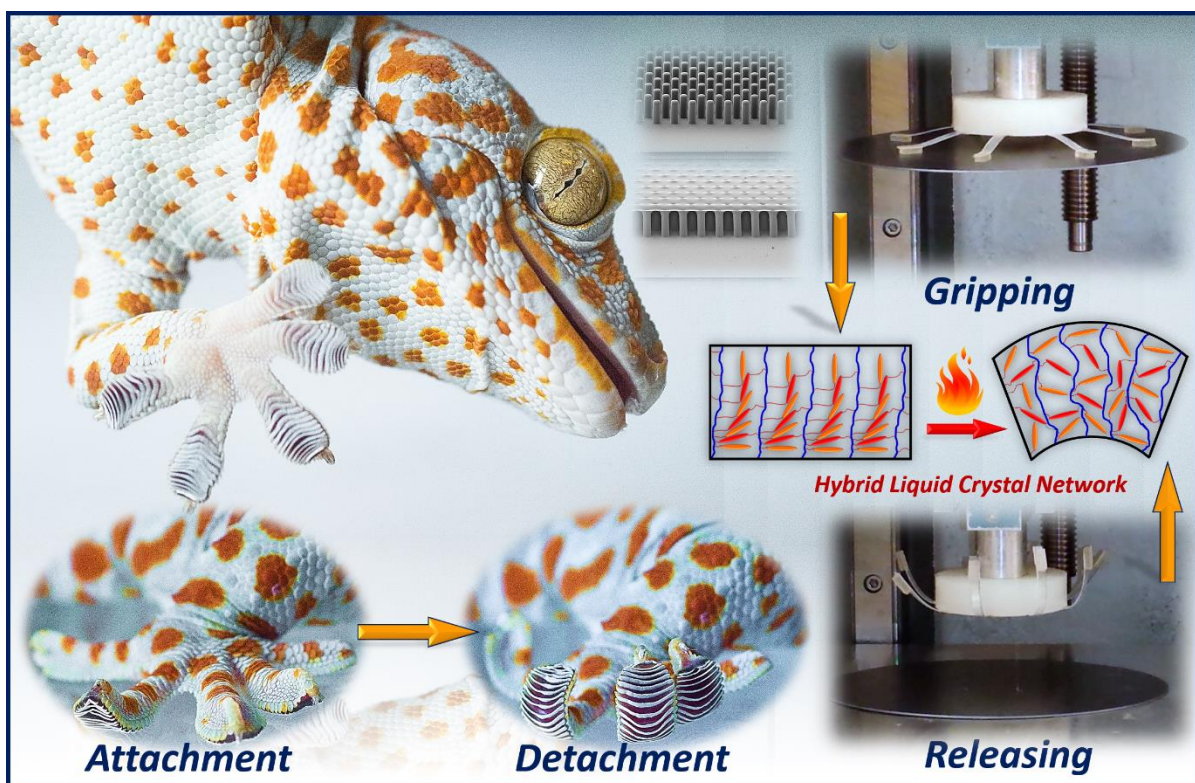
5.1 Introduction

Climbing ability of geckos is mainly attributed to their adhesive toe pads which are embroidered with hierarchical hair-like structures. Such surface structures promote compliance, facilitate intimate contact, and maximize omnipresent van der Waals interactions with mating surfaces [45,47]. It is known that particular configurations of geckos' toes play important roles in regulation of adhesion during their locomotion. In attachment, two diagonally opposite toes are attached and pull inward toward the animal's body center of the mass while the other two are detached. In a configuration known as Y-configuration, gecko applies both normal and lateral forces to push and drag the setae array against the mating surfaces [47,180,208,209]. During detachment, setae arrays are arranged in a critical angle to facilitate releasing of toe pads. Toes curl and scroll upward and away from the surface to rapidly reduce the high adhesion/friction using the setal shaft acting as the lever for perpendicular peeling off the spatulae from the substrates [2]. The back-scrolling motion and self-peeling of the toes at any instant during detachment concentrates the detachment force only on a small portion of all attached setae [45]. The back-scrolling motion is not only important for releasing, but also for self-cleaning, as contamination can be shed twice as fast when this motion is used [179].

Development of gecko-inspired adhesives is now a well-established field of research as a result of numerus reports published in the past two decades [46,49,210,211]. These structures usually are based on simple micro/nanopillars that are terminated by flaps [212] or thin films [1,213], and are bundled in either single or multiple levels [53]. Despite of the great achievements in fabrication of isolated and static fibrillar structures, active control of adhesion by mimicking smart and switchable properties of gecko toe pads still remains a challenge. Toward this end, one approach is based on gecko-inspired structures with tunable surface topography upon exposure to external cues, such as heat, light, or magnetic fields [89,138,183,186]. Second approach is based on directionality of dry fibrillar adhesives. Using this approach, shear induced grip and release and buckling-based release were employed in industrial and manipulation systems [98,214], or slanted micropillars were exploited for transfer printing [95]. The other approach is based on self-peeling and back-scrolling mechanism of gecko toe pads, which is practically used in a limited number of applications such as releasing phase of robotic locomotion mechanism [215]. Despite of the accomplishments in

mimicking the anisotropic mechanism of frictional adhesion of gecko toes during the gripping, the muscle-driven detachment mechanism, which is based on back-scrolling of gecko toes, has not been fully exploited and reproduced. This is important as the climbing dynamics and self-cleaning of the gecko toes is crucially dependent on this mechanism [216]. The resultant releasing capabilities can also have direct implication in other technologies such as pick and place handling of delicate objects and transfer printing.

Cross-linked networks of liquid crystal polymers (LCNs) with different level of cross-linking have been used as bending actuators, accordion-like ribbons, sophisticated voxellated 3D structures [4,118,195], and in applications, such as microfluidics, micro-electro-mechanical systems (MEMS), adaptive surfaces, and even transportation of 3D objects [126,137,188,217]. Also, remote control and manipulation of adhesion, friction, surface undulations and wetting of LCN micropillars have been subject of interest in a few reports [18,89,92,129]. However, potential application of LCNs for regulation of adhesion by stimuli responsive back-scrolling and self-peeling, resembling to the motion of gecko toe pads, has not been addressed well in the literature. In the only report recently published by us, dynamic self-cleaning was demonstrated by temperature-controlled deformations of micro-textured LCNs [18].

In this chapter, we report the integration of gecko-inspired adhesives to a hybrid nematic side-chain LCN cantilevers so as to design a multi-legged gecko gripper having thermally-induced self-peeling capacity. We also fabricate a prototype of the gecko gripper to handle (pick and place) thin delicate objects by determining the optimum mechanical strength of the LCN and the maximum size of the adhesive patch.

5.2 Experimental

5.2.1 Fabrication and synthesis procedures

Arrays of PDMS micro-pillars (50µm diameter, 150µm height and 100µm center-to-center spacing) were replicated from a Si wafer master mold with negative patterns by casting and curing of a liquid PDMS with 100:10 resin to cross-linking agent ratio (Sylgard 184, Dow Corning). The dipping method developed in ref [1,56] was used to fabricate thin film-terminated pillars (as sown in Figure 5-1a). A thin layer of liquid PDMS with the same resin-to-curing agent ratio was spun on a low surface energy microscope glass slide, and the fabricated micropillar arrays were placed upside-down on top of it. The entire system was placed in the

oven at 120°C for 1 hour, and the cured sample was peeled off gently from the substrate. Thickness of the terminal films, which was varied from 8μm to 24μm, measured by weighting the samples and confirmed by optical interferometry. The fabricated Geometrical features were characterized using a white light interferometer (Rtec Instruments, USA), digital microscope (DinoCapture from Dino-lite) and SEM.

Splay cells were made from two ITO-coated glass slides; one with planar and the other with homeotropic surface anchoring. Details of the cell preparation procedure has been described elsewhere [18]. The capillary cells were filled with molten mixtures of mesogenic monomers M1 and M2 (as shown in Figure 5-1b) with different weight ratios of M2 ranging from 12% to 75% at their isotropic temperatures. Monomer M1 is a mono-acrylate molecule, 4-(6-Acryloxy-hex-1-yloxy)phenyl 4-(hexyloxy)benzoate (T_{NI}=64), and M2 is a di-acrylate molecule, 1,4-Bis[4-(6-acryloyloxyhexyloxy)benzoyloxy]-2-methylbenzene (T_{NI}=113). Photopolymerization of the mixtures was triggered by Irgacure®651 photo-initiator, and carried out in the nematic phase (~53-55^{0}C) of the mixtures using 365nm UV light (Black-Ray™ Model B-100AP/R) for 30 min. The resultant LCN thin films were cut into rectangular cantilevers with different sizes.
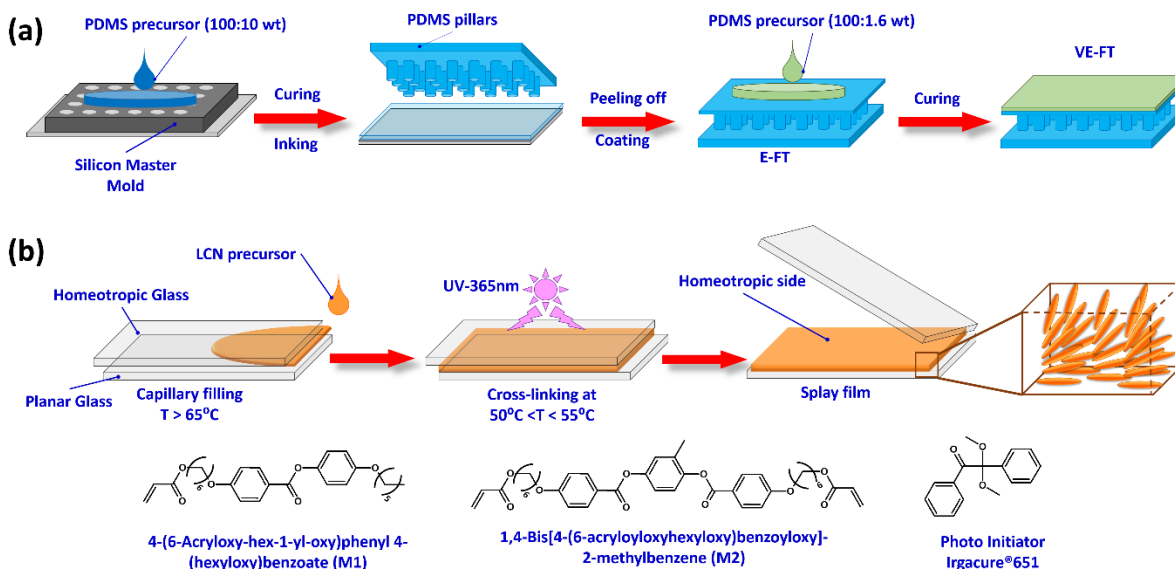
Figure 5-1. (a) Schematic view of the fabrication pathway including the three key steps of soft-lithography and microinking, which are followed by coating of a viscoelastic layer on top of the elastic film-terminated micropillars; (b) Schematic view of the fabrication process and molecular structures of the mesogen and photoinitiator used in LCE precursors.

PDMS adhesive patches cannot readily be attached to the LCNs by a piece of acrylic double-sided tape due to the low adhesion at the interface between the acrylic tape and the PDMS. To enhance the interfacial adhesion or bonding, a paper sheet was used as an intermediate layer to adhere the LCN to the PDMS. For this, a piece of paper was adhered to one side of the acrylic tape. Then, a small amount of the liquid PDMS precursor was poured on the paper side. Finally fabricated film-terminated fibrillar adhesives were laminated on the liquid PDMS and the whole system was placed in the vacuum oven at 120°C for 2 hours. Once cured, the second side of the acrylic tape was attached to the LCN film which was formerly cut into rectangular cantilevers.

For preparation of magnetic patch Iron micro-particles with 99% purity and 70 mesh size (< 212μm from Acros Organics, USA) was mixed with liquid PDMS precursor (100:10 wt% resin to cross-linking agent) with 25% weight ratio. The mixture was degassed with vacuum for 10min and then poured on a silicon wafer. A 1T electromagnet was put underneath the silicon wafer in order to align the iron particles. The whole assembly was placed in the oven and mixture was cured at 120°C for 1 hr. A circular magnetic patch with 1 inch diameter was then used for the measurement of magnetic stress. The magnetic attraction force was determined indirectly by measuring the required force for pulling-off the magnetic patch attached to the electromagnet when it is in "on" state. In detail, the magnetic patch was glued to an aluminum SEM stab with 1 inch diameter and the stab was connected to a string. The string was hanged on a hook that was clamped to a load cell of the universal material tester (UMT from Bruker, USA). The electromagnet was secured at the bottom stage. The magnetic patch was brought into contact with the electromagnet in "on" state. Then it was pulled away with a motorized load cell with 500μm/s retraction speed. The load vs. time was recorded during the experiment as can be seen in Figure 5-2. The magnetic stress was calculated by dividing the maximum pull-off force by the area of the patch and found to be ~7.6 kPa.
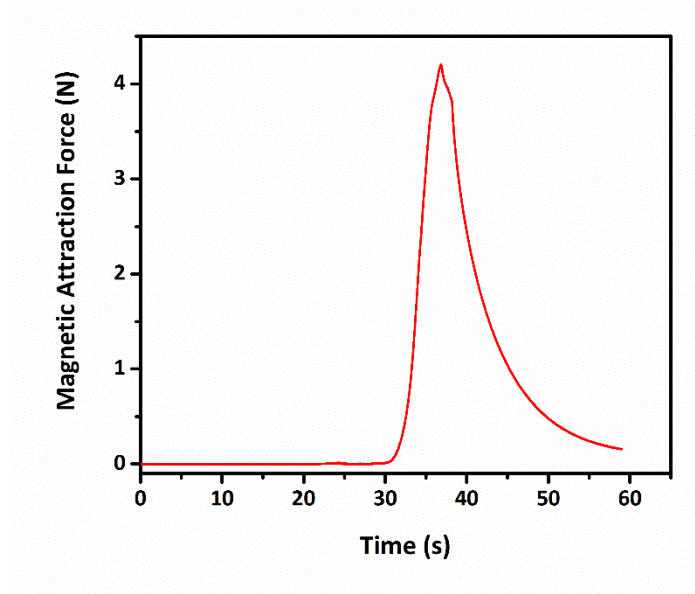
Figure 5-2. Magnetic pull-off force vs. time. The peak amplitude indicates the maximum force required to separate the magnetic patch from a 1T electromagnet in "on" state.

5.2.2 Characterization procedures

A custom-made micro-indenter assembled on top of an inverted optical microscope was used to measure the adhesive properties of all samples. Indentation was carried out by a 6mm diameter hemispherical fused silica probe (Ispoptics Co., New York), and the load−displacement data were collected with a 0−10 g load-cell (GSO-10, Transducer Techniques). The loading velocity in indentation tests was maintained at 1μm/s for all of the samples and the unloading velocity was varied from 1μm/s to 160μm/s.

The moduli of freestanding LCN films were measured using a Pyris Dynamic Mechanical Analyzer (Q800) with thin film clamp in tension mode. Temperature sweep tests were performed with 15μm amplitude and 1Hz frequency from 30°C to 150°C with the heating/cooling rate of 2°C/min. A Pyris Thermal Mechanical Analyzer was used to determine the thermotropic behavior of the LCN thin films. A static force of 50mN was employed during temperature sweep tests with 5°C/min heating rate.

The blocked force of the LCN cantilevers was measured using a stainless steel cantilever beam connected to a force transducer (FVL-0830, UMT from CETR, USA) while the whole arrangement was kept in a heating chamber. The tips of the LCN beams were fixed by a

84

2mm×2mm copper sheet glued to a cylindrical (1mm diameter) steel shaft connected to the cantilever beam, as shown in Figure 5-3a. Then, the blocked forces with zero tip deflection at different temperatures were recorded by a load transducer. The free displacement/deflection was measured by heating the LCN cantilever beams in a custom-build chamber equipped with a stereo-microscope and a CCD camera as shown in Figure 5-3b. ImageJ software was used to analyze the cantilever deformation images and calculate the radius of curvature. The overall tip displacement was measured by the arc length (*s*) of a circular profile that was projected on to the pathway of the cantilever during deformation. Sample calculation steps and pertinent trigonometric correlations are demonstrated in the Figure 5-3c.

$$\therefore \delta = \sqrt{\delta_x^2 + \delta_y^2}$$

$$= \sqrt{(x_2 - x_1)^2 + (y_2 - y_1)^2}$$

$$\rightarrow S = 2R \ \sin^{-1}\frac{\delta}{2R}$$
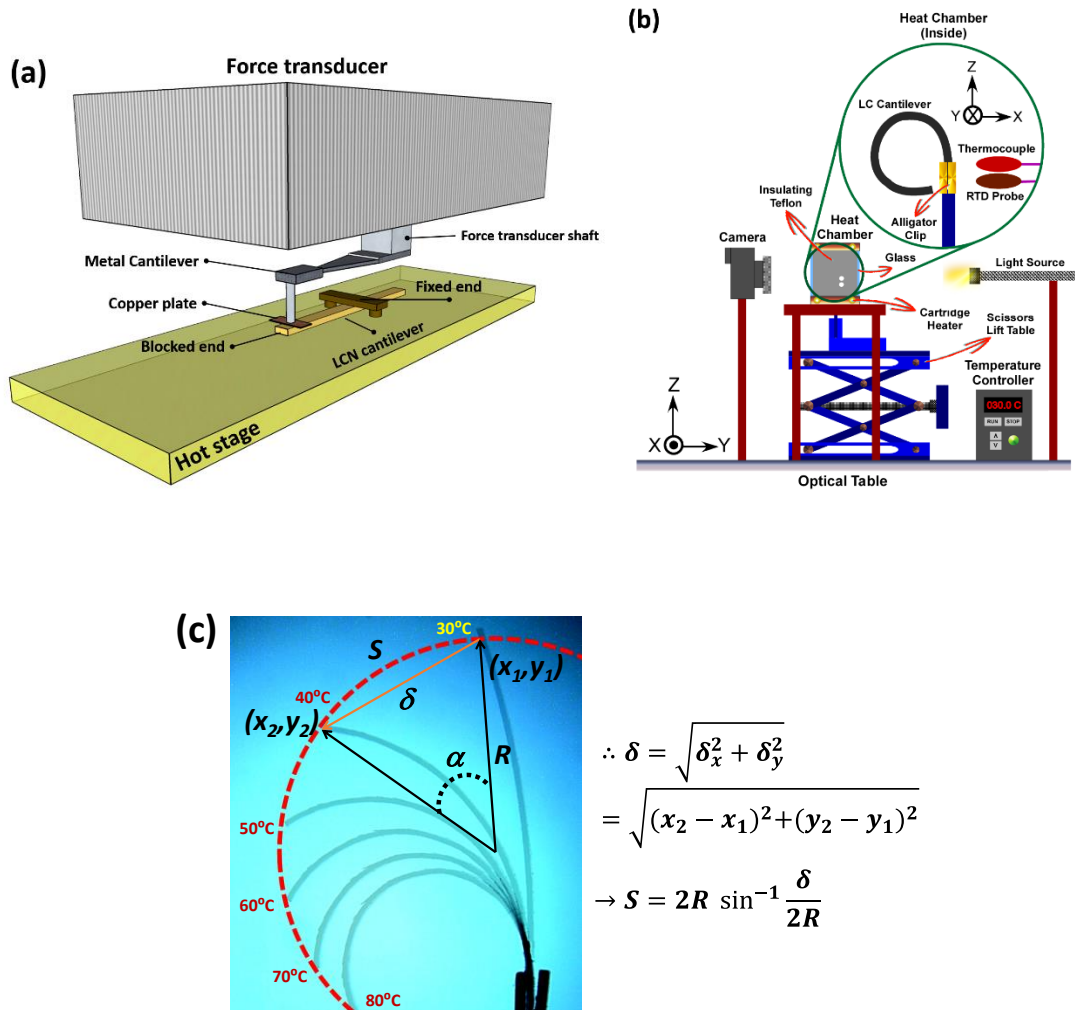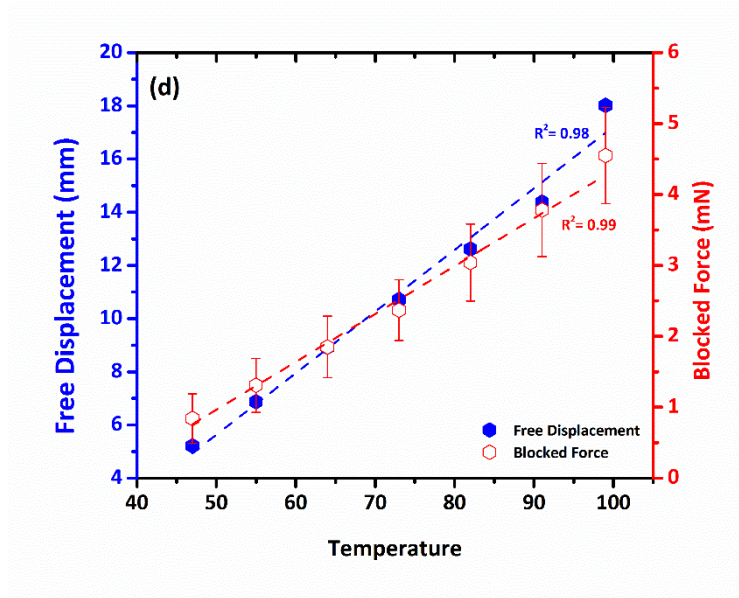
Figure 5-3. (a) Schematic of the blocked force measurement setup; (b) schematic of the free displacement measurement setup; (c) graphical illustration of the deformation arc length calculation and (d) variation of free displacement and blocked force with temperature

5.3 Results and Discussion

5.3.1 Design of a multi-legged gecko-inspired LCN gripper

Physical appearance of the gecko toes in gripping and releasing mode are shown in Figure 5-4(a-b). The schematics of the developed multi-legged gripper and the proposed mechanism of pick-and-place are illustrated in Figure 5-4(c-f). Each leg is made by a hybrid aligned (splay deformation) LCN cantilever fixed at one end, and a film-terminated fibrillar adhesive patch attached to the other end. The thickness of the LCN cantilevers is fixed at $188 \pm 4 \mu m$ and they are made of mixtures of mesogenic material (M1) with various cross-linking contents (M2). Two types of film-terminated fibrillar adhesive structures of PDMS, fully elastic (E-FT) and with a viscoelastic top-coat (VE-FT), will be used as adhesive patches. Figure 5-4d shows SEM image taken from the sample E-FT. In our design, the gripping of lightweight thin and flat objects such as a silicon wafer can be achieved through normal preloading of the adhesive patch to the substrate. Due to the flexibility of the LCN cantilever and lightness of the adhesive assembly, natural downward curvature of the LCN did not provide adequate preload stress during approaching. For this reason, we attached small magnetic patches to the upper side of cantilevers as shown in Figure 5-4e; in this way, preload stress can be provided via attractive

86

magnetic field created by an electromagnet underneath the sample. Releasing was triggered by the temperature-driven bending of the LCN cantilever that caused peeling off the adhesive patch, as can be seen in Figure 5-4(f-g).
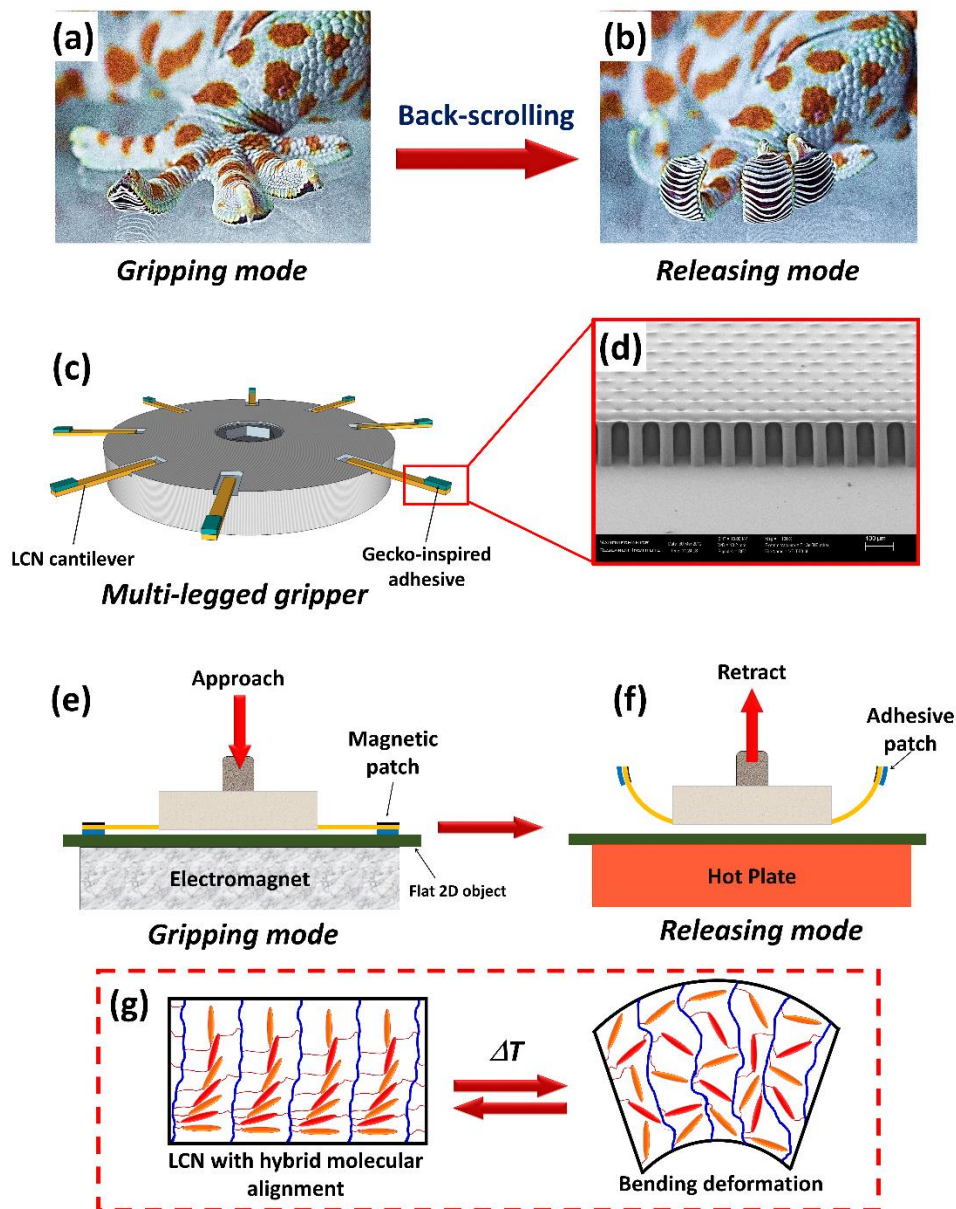
Figure 5-4. Optical images of gecko toes (a) fully extended in gripping and (b) back-scrolled in releasing modes; (c) schematic view of the designed multi-legged LCN-based gripper with (d) biomimetic film-terminated fibrillar adhesives; proposed mechanism of (e) gripping facilitated by an electromagnet and (f) releasing induced by thermal deformation of hybrid LCN cantilevers; (g) mechanism of shape change in a nematic hybrid LCN during nematic – isotropic transition which is along with expansion on the homeotropic side and contraction on the planar side.

There are some basic criteria that should be met to enable the gripping and releasing. *For gripping*, the magnetic field should be sufficient to impose necessary preload; the adhesive strength of the adhesive patches need be high enough to bear the gravitational force acting on the lifted object; the LCN cantilevers must be resilient enough to retain their structural integrity when bearing the weight of the lifted objects. *For releasing*, the LCN cantilever output bending force must be high enough to overcome the adhesion of the patches and the deformation must be large enough to create sufficient momentum to develop crack front during the peeling. We expect higher load bearing and bending forces but smaller bending amplitude from stiffer LCN cantilevers since high force output and high amplitude are mutually exclusive due to limited output work density of the actuators. The output work density (the work generated by the bending actuators divided by their volume) is $\overline{W} \sim (\frac{1}{2})Y.\varepsilon^2$, where Y is the Young's modulus and ε is the strain [218]. Due to deterministic nature of the work of adhesion, LCN output work density and the adhesive patch size are indeed only design parameters of interest in this work.

5.3.2 Thermo-mechanical properties of the LCN cantilevers

The mechanical properties of free-standing LCN cantilevers with different compositions were determined by dynamic mechanical analysis (DMA). Results showed that the Young's modulus of the LCN at room temperature increases from 30 MPa to 1.5GPa when the M2 content increases from 12 wt% to 75 wt%. Side-view images of thermal deformation of LCN cantilevers fixed at one end with different M2 contents are shown in Figure 5-5a. The curvature ($\kappa = 1/r$), where r is the radius of curvature, was measured by fitting the bent LCN to a circular profile using ImageJ software. The temperature dependences of the curvature measured during cooling with different cross-linking contents are plotted in Figure 5-5b. The magnitude of thermal deformation ($\partial\kappa/\partial T$) decreases with increasing M2 content.
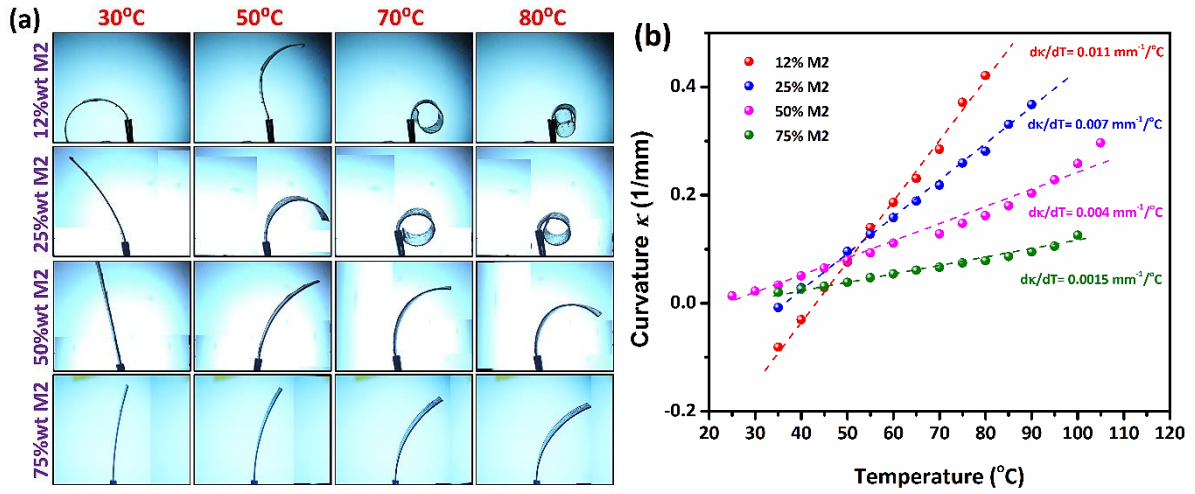
Figure 5-5. (a) Side-view images of hybrid LCN cantilevers with different content of cross-linking mesogen subjected to thermal deformation (photos are taken during the cooling); (b) variation of curvature with temperature

In order to calculate the output work density of the LCN cantilevers, both free tip displacement and blocked force (the maximum force generated at the free tip of LCN cantilever when it is fixed) need to be known. Therefore, two separate sets of experiments, similar to methods developed in [219,220], were performed to measure the blocked force and free tip displacement. In the arrangement shown in Figure 5-3a the free tip of the LCN beam was fixed by a stainless steel cantilever to block the thermal deformation. The maximum force at the LCN cantilever tip, $F_{max,}$ was measured and recorded by a force transducer during heating. The free tip displacement, δ_{max}, is defined by the LCN cantilever tip deflection during thermal deformation without any constraint and was measured visually at different temperatures using a CCD camera, as shown in Figure 5-3b. Note that unidirectional tip deflection cannot be used due to extremely large deformation of the LCN cantilevers. Instead, the free tip displacement was approximated by the arc length on the trajectory of thermally induced tip deflection that was projected on a virtual circle. Details of free displacement measurement and calculation are illustrated Figure 5-3c.

Samples with 12% and 25% M2 content did not show sensible blocked force in the arranged setup. Therefore, LCN samples with 50%wt M2 content were chosen for the rest of studies. As both F_{max} and δ_{max} are temperature-dependent, the $F_{max,}$ vs δ_{max} curves must be plotted for characterization of the system at corresponding temperatures. As shown in Figure 5-3d for

$1.3mm \times 2mm \times 0.188mm$ size LCN cantilevers, in first approximation, both $F_{max,}$ and δ_{max} vary linearly with temperature [221,222]. Figure 5-6 shows variation of blocked force vs free displacement at different temperatures. The area under $F_{max,}$ vs δ_{max} curves represent the maximum mechanical work output that LCN cantilever provides. The work density of the cantilevers at each temperature is shown at the inset of Figure 5-6. It shows that the slope of the temperature dependence of the energy density is increasing with temperature and the values are similar to the output work density obtained for materials with similar chemistry [223].
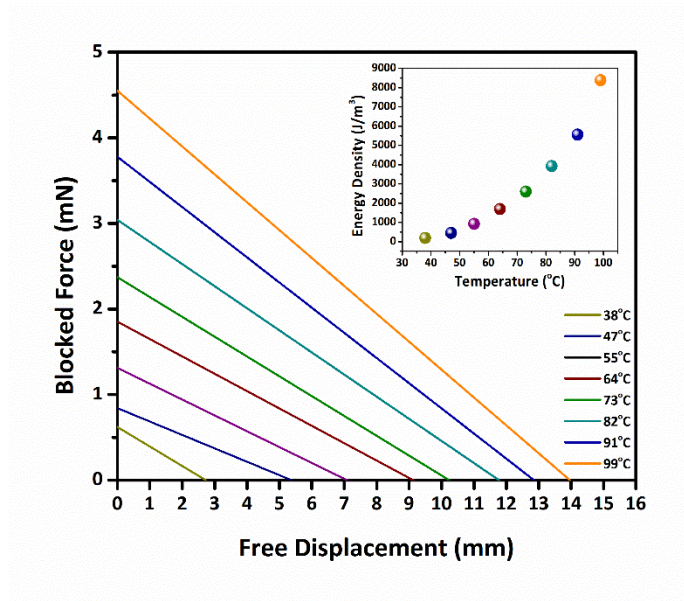
Figure 5-6. Blocked force versus free displacement for an LCN cantilever with $13 \times 2 \times 0.188$ mm3 size at different temperatures. The inset shows the variation of output energy density with temperature.

The bending energy of the LCN strip of Young's modulus Y, length of l, width of b and thickness h is related to the curvature κ as: $E_b = \frac{Y\kappa^2 h^3 lb}{24(1-\sigma^2)}$ where σ is the Poisson ratio of the LCN strip. Accordingly, LCN cantilevers with higher Young's modulus can generate greater work for peeling off the adhesive patch during the releasing. However, deformation of the stiffer LCN cantilevers takes place at higher temperatures and requires more thermal energy input. This will adversely influence the efficiency of the gripper and limits its applicability in transport of objects at lower temperatures. It is worth noting that the theoretical output work density of bending LCN actuators is usually obtained from room temperature modulus and the strain as $\overline{W} = \frac{1}{2}Y.\varepsilon^2$. Assuming a symmetric linear strain profile along the thickness, one can estimate the strain difference between top and bottom of the cantilever with respect to straight unbent

position as $\Delta \varepsilon = \kappa h$. Using definition of energy in linear elasticity, theoretical energy density can be calculated by the measured Young's modulus, the curvature and the film thickness as $\overline{W} = \frac{1}{24}\frac{\kappa^2 h^2}{(1-\sigma^2)}Y$ and also can be estimated from the measured F_{max} and δ_{max} by $1/(lbh)\int_0^{\delta_{max}} F_{max}d\delta$. Those results are tabulated in Table 5-1. Results show that there is an increasing discrepancy between experimental and theoretical values of the output energy density at increasing temperatures. This is likely due to softening of the LCN cantilevers in higher temperature as seen in DMA results. That is, the softer they become the less output work they provide due to lower elastic modulus. Furthermore, the theoretical values are valid only for small deformations, which is not the case, especially at increasing temperatures. Systematic study on theoretical prediction of output energy density and elastic modulus will be the scope of our future work.

Table 5-1. Variation of theoretical and experimental output work density with temperature

Temperature [^{0}C]	Work Density (experimental) [kJ/m^3]	Work Density (theoretical) [kJ/m^3]
38	0.19	0.45
47	0.45	1.1
55	0.92	25
64	1.7	70.1
73	2.6	110
82	3.9	129
91	5.6	181
99	8.4	229

5.3.3 Adhesive properties of the biomimetic adhesive patches

Physical properties of film-terminated fibrillar adhesives have been extensively investigated in other works [1,56,146,157,213]. Previous studies showed that the adhesion enhances when the thickness of the elastic terminal layer decreases and the thickness of the viscoelastic topcoat increases [1,56,157,213,224]. Based on our previous results, the optimum thickness of the elastic terminal layer and the viscoelastic topcoat were set at 10 and 50μm, respectively [1].

Force vs displacement and variation of the pull-off force against preload for E-FT and VE-FT were compared to the bare control PDMS sample (E-B) and results are plotted in

91

Figure 5-7(a-b), respectively. Except for E-FT, a pronounced snap-in force is observed when the indentation probe approaches the surface of E-B and V-FT because of the intermolecular surface forces. Upon contact between the probe and the samples, the contact area forms and expands as applying increasing normal compressive loads (i.e., preload). B-E and VE-FT have the highest and the lowest contact area and slope of the loading portion. This is due to remarkable increment in surface compliance for the functionally graded adhesive. Comparison of the loading portion of the force-displacement curves for E-FT and VE-FT reveals that the micropillar arrays in VE-FT experience the buckling at much lower preloads. This phenomenon leads to drastic enhancement of compliance associated with slippage/shear of the viscoelastic topcoat and generates higher pull-off force [1]. The unloading portion of the force vs. displacement curves was linear for a remarkable range of retraction distance before reaching the pull-off point, where the tensile adhesive force is the highest. The debonding for both E-B and E-FT is rapid, but with several small zigzag steps for the E-FT, suggesting the presence of crack trapping mechanism during the separation. The debonding process of the VE-FT sample is smooth but with a slope change before separation as a result of dissipative bulk deformation processes such as fibrillation, cavitation and other instabilities, which are thoroughly elaborated in our previous reports [1,56]. Both E-FT and VE-FT have remarkably greater pull-off force and hysteresis than that of E-B. In contrast to the bare elastic control sample, both E-FT and VE-FT show notable preload dependence. The preload dependence is much more pronounced for the VE-FT and was shown in previous studies to level-off at higher preloads [1,56].

Two other parameters required for proper design of the gripper are "pull-off" and "preload" stress. These parameters are calculated by dividing the pull-off and preload forces by their corresponding contact area. The results are tabulated in the Table 5-2.
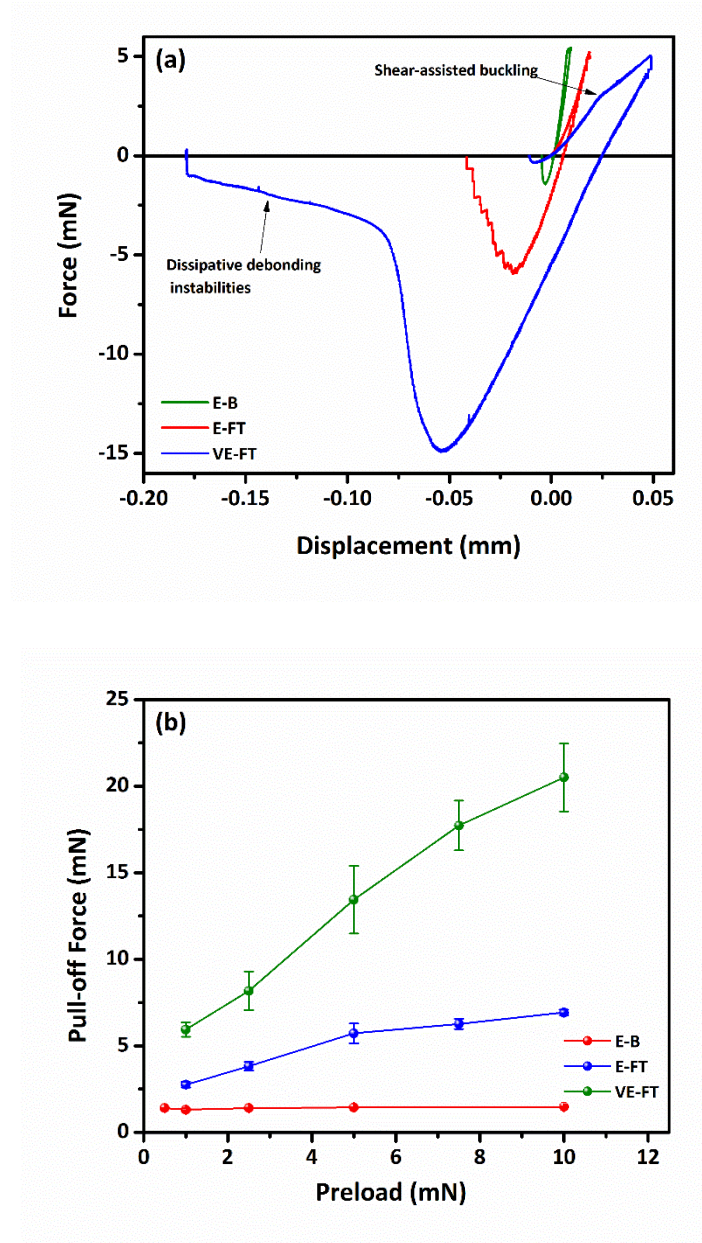
Figure 5-7. (a) Load vs. displacement curves for the indentation of a hemispherical probe on different adhesive samples, elastic bare PDMS (E-B), elastic film-terminated fibrillar adhesive (E-FT), and viscoelastic film-terminated fibrillar adhesive (VE-FT); (b) variation of pull-off force with preload

Table 5-2. Variation of pull-off stress vs preload stress for different adhesive structures

Sample	Preload Force (mN)	Preload Stress (kPa)	Pull-Off Force (mN)	Pull-Off Stress (kPa)
	1	5.5	2.7	14.5
	2.5	12.2	3.8	18.8
E-FT	5	17.9	5.7	26.6
	7.5	22.6	6.3	27.9
	10	24.2	6.9	28.9
	1	1.7	5.9	17.7
	2.5	3.3	8.2	21.7
VE-FT	5	4.8	13.4	26.3
	7.5	5.8	17.7	30.9
	10	6.1	20.5	32.6

The adhesion energies for E-FT and VE-FT were measured by calculating the area between the loading and unloading curves in an indentation cycle. Then the overall work of adhesion (W_{adh}) was measured from the slope of the adhesion energy against maximum contact area as shown in Figure 5-8. The work of adhesion for both VE-FT (1.49 J/m^2) and E-FT (0.49 J/m^2) are remarkably greater than that of E-B (0.07 J/m^2), which was previously obtained by JKR [1]. This indicates that both VE-FT and E-FT can be used as reusable biomimetic adhesives for the purpose of the pick-and-place.
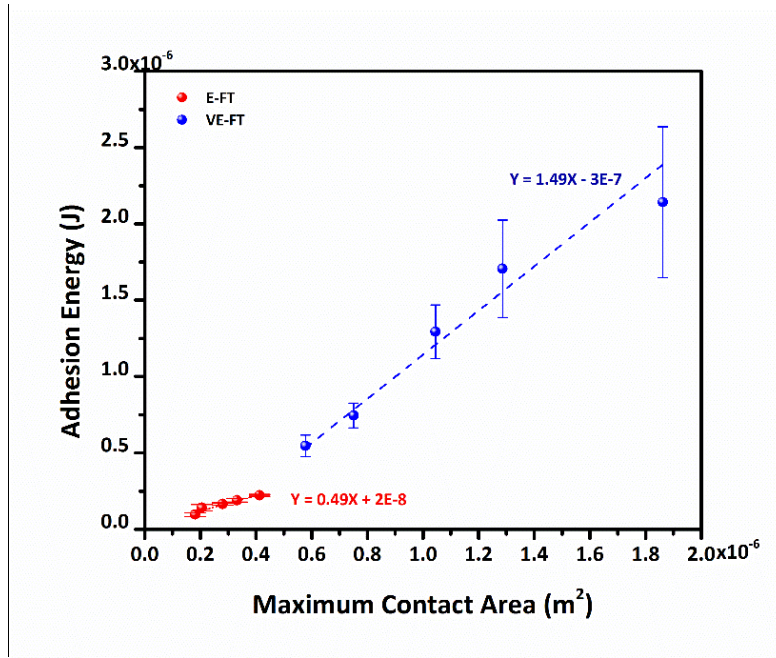
Figure 5-8. Variation of adhesion energy with the maximum contact area at preload for determination of overall work of adhesion

5.3.4 Development of gecko-inspired LCN gripper

The maximum magnetic stress that an electromagnet with a magnetic field of 1T provides the maximum preload stress of ~7 kPa. This preload stress is corresponding to pull-off stress of ~35 kPa for VE-FT and ~16 kPa E-FT (Table S1). To lift and transfer a 4" silicon wafer with mass of ~9 g, the minimum required size for the VE-FT and E-FT adhesive patches will be ~2.8 mm^2 and ~6.4 mm^2, respectively. Practical imperfections such as misalignment and non-constant or inadequate preload stress necessitates use of larger adhesive patches to guarantee secure transfer of delicate objects. However, the maximum size of the adhesive patch is limited to the output bending work of LCN cantilevers so they are able to propagate the crack at the adhesive interface for efficient releasing. Knowing the LCN work output vs temperature and overall work of adhesion for the VE-FT and E-FT, the maximum size of the adhesive patch that can self-peel via the bending of LCN cantilevers can be calculated at different temperatures from $E_b = W_{adh}.A_{max}^P$. The maximum size of the adhesive patches of E-FT and VE-FT that an LCN cantilever with 13×2×0.188 mm^3 size can peel off from a smooth flat substrate at 100°C were obtained 84 and 28 mm^2, respectively.

95

It is worth noting that both the work of adhesion and the bending energy of LCN depend on the surface temperature. Higher surface temperature could heat up the LCN faster, causing the larger and faster bending of LCN, which could in turn increase self-peeling speed of LCN (see the supporting information for additional details). Hence, temperature/rate-dependent dynamic effects are involved in our system. The rate-dependent behavior of fibrillar adhesives are well studied in the literature [57,101,225–228]. It has been found that the speed of crack propagation increases as the retraction rate (i.e. the peeling rate in our case) increases, giving higher strain energy release rate or adhesive force.

For this reason, two sets of experiments were conducted to examine the rate of LCN deformation at different surface temperatures and the influence of delamination rate on the adhesion. Due to the practical limitations, measurement of the adhesion force and rate of LCN deformation at different temperatures at the same time is not viable. We first conducted a series of experiments to calculate the maximum rate of deformation in the testing geometry of our system. A single LCN cantilever was attached to the gripper central clamp and the whole assembly was approached towards a preheated hot stage. A magnetic and an adhesive patch were attached to the free end of the LCN cantilever to mimic the real loading condition during the gripping/releasing experiments. The radius of curvature and location of the LCN free end before and after contact with the hot stage were recorded using a side-view camera. The heating stage was preset to different temperatures ranging from 80^{0}C to 140^{0}C. Then, the average LCN deformation speed was calculated by dividing the length of the tip deflection vector to the time. Results show that the higher the heating stage temperature is, the faster LCN cantilever can deform (0.4 mm/s to 1.8mm/s). In a crude approximation, these values can be deemed as upper limits of the retraction speed at different hot stage temperatures (see Figure 5-9a). In a separate set of experiments, the adhesion force of the VE-FT adhesive patch was measured by indentation at different retraction speeds from 0.001 mm/s to 2 mm/s. As can be seen in Figure 5-9b, higher unloading velocities result in higher adhesive pull-off forces. Similar behavior has been observed in other reports in the literature [57,226–228].

96
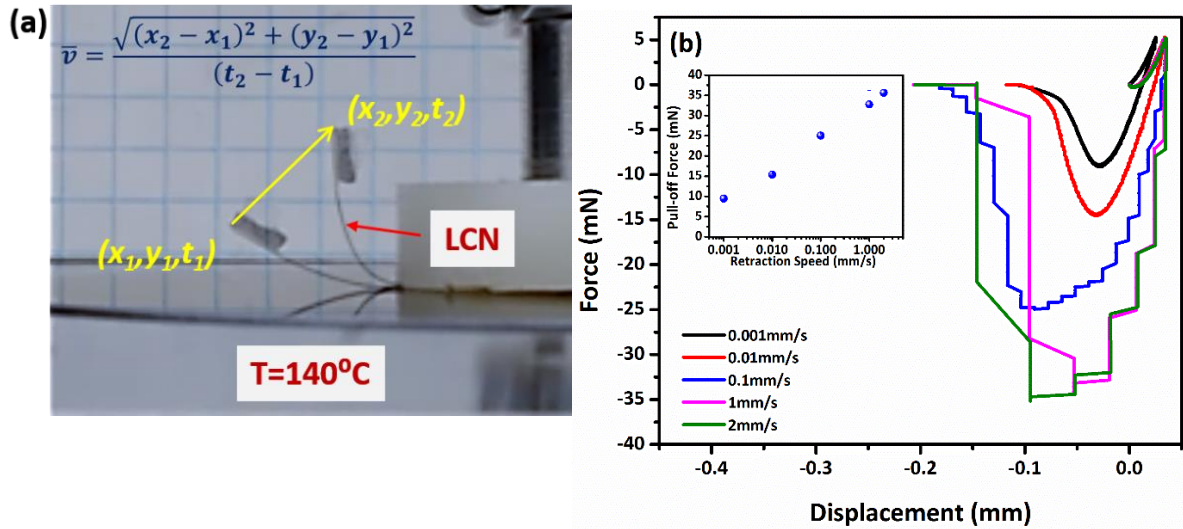
Figure 5-9. Experimental set-up for measurement and calculation method of the LCN deformation speed; (b) load-displacement graphs for indentation on VE-FT adhesive sample with different retraction velocities ranging from 0.001 mm/s to 2mm/s.

As indentation tests show, that the adhesive pull-off force of our adhesives increased with the retraction speed. This rate-dependent dynamic adhesion force should be taken into account in design and compensated for easy detachment. A similar case has been reported by Song and Sitti, where mushroom shaped micropillars on a soft inflatable membrane were used as a soft gripper for transferring of 3D objects. Due to viscoelastic dissipations, increment of the retraction speed during the unloading of adhered objects resulted in higher adhesion force. To compensate for these additional forces, they used higher inflated length or curvature during releasing [101]. Herein, in a similar strategy, larger curvature of LCN cantilevers caused by the higher surface temperature (Figure 5-5) can spontaneously compensate for the excessive adhesion forces arising from dynamic viscoelastic effect. Even though the complex dynamic effects involved in our system have yet to be elucidated in future work, they are not expected to change the estimated maximum size of the adhesive patches much. Indeed, our experiments showed that the LCN adhesive pads designed using the parameters obtained at a constant temperature and speed can effectively release adhesion by the surface temperature-induced self-peeling of LCN, even though the adhesion force would be greater at higher temperature.

A prototype multi-legged gripper was made as shown in Figure 5-10(a-b). Misalignment with objects' center of gravity and undesired torque can be prevented by use of

at least three legs. Our design is composed of eight LCN cantilevers, which are fixed at one end to an aluminum holder cylinder and attached to biomimetic fibrillar adhesive patches on the other end. The sizes of the adhesive patches were between minimum and maximum values calculated in the previous section (8-10mm^2 for each cantilever). Magnetic patches of identical size are glued on the top of the adhesive patches to facilitate preloading by attractive magnetic stress. According to Figure 5-10(c-h), gripping takes place by simple magnetic preloading and actuation of the LCN cantilevers toward the surface of the Si wafer using an electromagnet. Upon gripping, the electromagnet is turned off and the gripper cylinder is pulled upward to lift the object. After certain length of lateral movement, the gripper approaches toward the surface of a hot stage. Finally, in a mechanism similar to gecko toes back-scrolling, the releasing is rendered by self-peeling of the adhesive patches due to the bending deformation of hybrid LCN cantilevers. The side-view and bottom-view of a single cantilever with adhesive patch in contact with a transparent heating stage confirmed that the delamination of the adhesive patch is in the peeling mode and the peeling front develops from the cantilever tip towards the center of the gripper.

In contrast, experiments were performed with non-patterned adhesive patches, showing very low gripping ability of the elastic non-patterned adhesives and very difficult releasing of the non-patterned adhesives with viscoelastic topcoats. As reported in the literature and our previous work, gecko-like patterned adhesive patches have remarkably higher adhesion coefficients ($\mu´ = F_{pull-off}/F_{preload}$) than their non-patterned counterparts, meaning that lower preloads are required to achieve higher pull-off forces, which is particularly beneficial for the gripping. On the other hand surface microstructures alleviates the debonding instabilities of the viscous topcoats to avoid the cohesive failure of the adhesive during detachment [1,57].
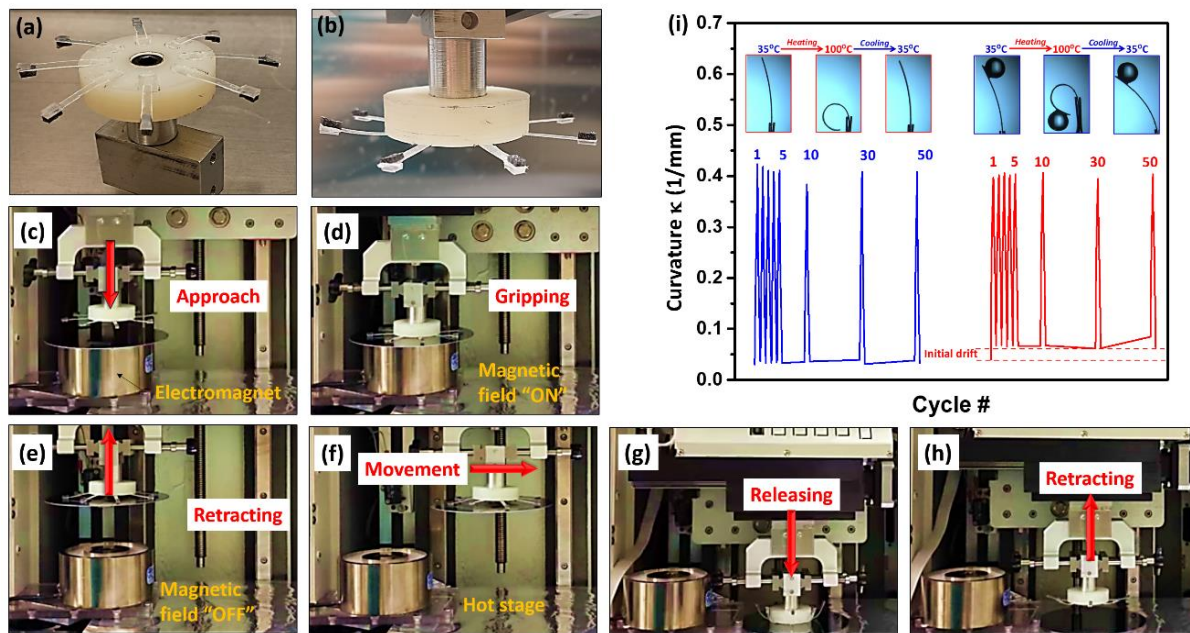
Figure 5-10. A multi-legged gripper (a-b) for pick-an-place automation, when it approaches toward the silicon wafer on an electromagnet stage (c). Normal gripping is facilitated by the magnetic field (d), and the silicon wafer is lifted when the electromagnet is in "off " state (e). Later movement (f) is followed up by approaching the silicon wafer towards the hot stage and thermal bending deformation facilitates release (f); finally the griper retracts back (h); variation of curvature with temperature after 50 cycles of heating and cooling for free and loaded cantilevers (i).

The performance of such assembly and its applicability in industrial manipulation systems crucially depends on durability of both adhesive structures and LCN cantilevers. Plastic distortion of the LCN cantilevers during repeating cycles of heating and cooling is identified as of the potential factors affecting the maximum deformation amplitude and durability. Bending deformation at two loading regimes of 1) peeling off from the substrate and 2) after peeling might cause plastic distortions. During the peeling, the load on the cantilever can be approximated by the pull-off force of the adhesion patch to be ~12.5mN for the VE-FT. After peeling, the load on LCN can be approximated by weight of the adhesive and magnetic patches to be ~0.7mN. Thermal deformations of both free and loaded LCN cantilevers were examined in tests with multiple cycles, and results are shown in Figure 5-10i. We used a glass bead with weight of 0.7 mN to simulate the loaded deformation after peeling. Apparently, the magnitude of thermal deformation for free LCN cantilevers remains constant even after 50 cycles as shown in Figure 5-10i(left-side). For LCN cantilever loaded with ~0.7mN, there is a small drift in the second cycle. Thereafter, the magnitude of thermal deformation remains almost constant even

99

after 50 cycles as shown in Figure 5-10i(right-side). Similarly, thermal cycling of the loaded cantilevers with ~12.5mN in very low deformation range showed repeatable peeling behavior and only a slight plastic distortion.

To examine the reusability of gripper, the multiple adhesion measurements on a single spot of adhesive pads (E-FT and VE-FT) samples were performed. As shown in Figure 5-11, the adhesion force of the E-FT sample was not deteriorated up to 30 repeats. Whilst, the adhesion force for the VE-FT started to decay from the beginning and reached to the 70% of its original value after 30 times repetition. Multiple gripping/releasing of a silicon wafer was also performed; they successfully repeated over 20 times with a gripper equipped with E-FT and VE-FT adhesive patches. Afterwards, the gripper with the viscoelastic topcoat (VE-FT) started to lose performance, most likely, due to the plastic deformation of the topcoat and absorbing surface contamination. Thus, potential use of fully elastic fibrillar adhesives but with better adhesion performance, e.g. mushroom shaped fibrils, can help to ensure good reusability.
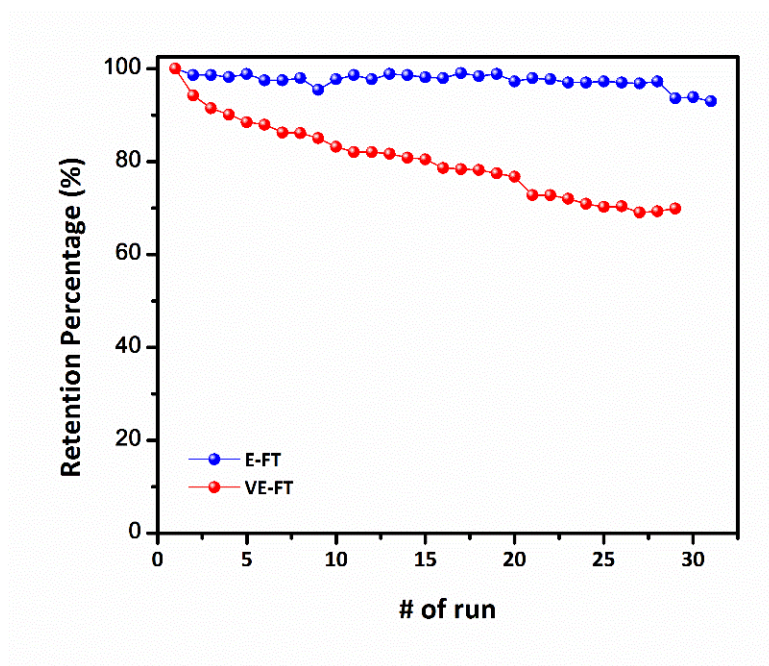
Figure 5-11. Variation of the pull-off force retention percentage vs. number of tests been ran on a single spot

Our results also show remarkable load bearing capability of the tested LCNs, which is equivalent to carrying loads up to 100 times of their own weight (0.125mN), within their range of deformation. The outstanding deformability (i.e. displacement/length) of LCNs shown in this

100

report and elsewhere [229], places them next to phase transition activated nanolayer bimorphs of Si/VO2 [218], polymer-CNT composite actuators and superior to the shape memory alloys (SMA), thermal expansion, and piezoelectric actuators [112]. Thus, the Gecko-inspired self-peeling releasing mechanism shown in this work can be implemented in development of novel micromanipulation systems without requiring sophisticated feedback control systems. Although only one type of thermoresponsive polyacrylate LCN system was tested here, variation of the molecular structure of the LCN cantilevers can create a great range of output energy densities up to 3000 kJ/m^3) [110]. The attainable adhesion forces can be modulated by altering physical and geometrical properties of the adhesive pads.

5.4 Summary

To summarize, in this work the back-scrolling and self-peeling mechanism of gecko locomotion was mimicked using a LCN cantilever topped with a film-terminated fibrillar adhesive so as to make an effective gecko gripper. Output energy density of the LCN cantilevers along with their level of deformation was investigated by varying the level of network cross-linking. It is shown that LCN with moderate level of cross-linking provides sufficient output work to detach film-terminated adhesive patches from flat and smooth surfaces. The size of the adhesive patch is estimated from the LCN output work and work of adhesion. Self-peeling mechanism of the proposed structures was employed in pick and place handling of flat and smooth 2D objects. Results in this work can be deemed as a proof-of-concept for implementation of gecko-inspired back-scrolling mechanism for development of switchable adhesives as soft grippers. Further, combination of high energy density and large deformation suggests that LCNs are good candidates for effective load bearing and large actuation. Future works will be focused on theoretical studies on the self-peeling mechanism of dry fibrillar adhesives backed with active materials and optimization of deformable materials mechanical performance using different groups of active materials.

Chapter 6
Concluding Remarks and Recommendations

6.1 Concluding Remarks

The main objective of this thesis research was to develop a remotely controlled, functional and smart adhesive system that can act in "on" and "off" states. Emulation of functional and switchable adhesive system of gecko toe pads has been proposed and utilized as a novel approach to realize this objective. It is well-documented that there are two elements central for repeatable attachment/detachment cycles of a gecko toe during its locomotion. The first key element is the multi-level hierarchical hair-like structures that cover the toe skin. Robust, flaw-tolerant and directional adhesion along with self-cleaning features of gecko adhesive toe pads are attributed to this element. The second key element is gecko toes' muscular motions by which the interaction of the toes with mating surfaces is regulated. Easy detachment through peeling and dynamic self-cleaning of the gecko adhesive system are attributed to this element. Accordingly, three research steps were carried out to fabricate a similar synthetic system. In the first step of the research, film-terminated and functional adhesive structures with enhanced cohesive properties were fabricated to mimic the gecko toes' skin topography and adhesive behavior. In the second step of the research, artificial muscles based on LCE and LCN materials were developed to mimic the muscular motions of the gecko toes. In the third step, the research findings of the previous two steps were integrated to develop a unit assembly to emulate the smart functionality of a gecko toe during an attachment/detachment cycle. Furthermore, a potential technological application of this assembly was demonstrated for the transportation of delicate and fragile objects. The concluding remarks and some scientific and practical insights acquired from each step of this research are listed below.

- A new class of biomimetic graded and functional adhesive structure is proposed and developed, showing a remarkable increment of the adhesion pull-off force, work of adhesion, and compliance.
- High adhesive strength of the newly proposed adhesive is resulted from both the viscous effect of the topcoat and crack trapping mechanism of the elastic intermediate layer, which causes drastic energy dissipation during detachment.

- High cohesive strength of the newly proposed adhesive is resulted from retrieving the elastic strain energy stored in micropillars during the loading, which facilitates crack propagation on the viscous layer during unloading.

- The significant compliance of the new structure is attributed to the effect of interfacial slippage on the bending and buckling of the fibrils underneath the viscoelastic layer.

- Integrative soft-lithography of a hybrid aligned LCE was employed to produce adhesive assemblies to enable the stimulus-responsive actuation of micro-fibrillar structures.

- Different thermal modes of deformation (bending and twisted-bending) of the LCEs can be pre-determined and obtained by adjusting the ratio between thicknesses of the LCE backing layer and the height of the micro-pillars.

- External stimulation (heating) of the micro-textured splay LCE films are exploited for the remote control of self-cleaning properties in a mechanism similar to digital hyperextension of the gecko toes.

- The output energy density and level of deformation of the LCN cantilevers crucially depend on their mechanical strength and level of cross-linking.

- Judicious selection of cross-linking level ensures sufficient output energy and strain for the LCN adhesive pad so that they can be used to make a gecko toe pad-like soft gripper.

- Due to inherent constraints in choosing material properties, the size of the adhesive patch is introduced as another design factor that should be taken into account.

- Combination of high energy density and large deformation suggests that LCNs are good candidates for effective load bearing and large actuation.

- The major drawback of this technique is the softening of the LCN materials at high temperatures which cause deterioration of the mechanical strength and drop of the output energy density. Hence, optimization of materials mechanical properties seems to be an indispensable task if this technology is to compete with other existing ones such as dielectric elastomer (DE) artificial muscles.

6.2 Challenges and Recommendations

The research results in this project demonstrated the successful integration of LCN materials to functionally graded biomimetic adhesives so as to mimic the responsive nature (i.e. the switchable adhesion property) of gecko adhesive toes. Nevertheless, it is necessary to achieve an optimal performance for the proposed assembly so it can be utilized in technological

applications. There are the challenges of combining these two class of materials as resolved in the project; there are also other challenges associated with both LCN materials and adhesives, which should be addressed. This section briefly recapitulate these challenges and suggest potential solutions that might be helpful for future studies.

The first challenge is related to the performance of the film-terminated fibrillar adhesives. It is known that elastic film-terminated fibrillar structures of a material can enhance adhesion. However, the adhesion force of film-terminated structures from such polymers as PDMS and polyurethane is not strong enough to fulfill requirements of the majority of practical applications. That was the main motivation behind addition of a viscoelastic topcoat that was reported in the chapter four. Although effective in enhancing adhesion force and energy, addition of a viscoelastic topcoat limits the extent of reusability of these adhesives. With regard to this problem, mushroom-shaped fibrillar surfaces, as the most effective dry adhesives reported in the literature [211], can be the geometry of choice. In fact, rational design of an interface embroidered with mushroom-shaped pillars can boost the adhesion force, reusability, and directionality [46,214]. Alternative dry adhesives, that are not fibrillar, can also be exploited in our assembly as the adhesive patch. Use of non-patterned but very compliant assemblies is reported as an alternative approach for manufacturing of dry adhesives with drastically enhanced adhesion force [230]. Similar strategy has been recently taken by the author of this dissertation for enhancement of the adhesion by use of film-terminated foam-based structures from PDMS [231].

The second challenge is related to LCEs/LCNs' poor mechanical properties, slow response time and limited control over the stimulation technique. On the one hand, lightly cross-linked LCEs with low T_g are very delicate and soft and generate low output work density, which limits their use in applications requiring high load bearing. On the other hand, heavily cross-linked LCNs with higher T_g are very brittle and require higher temperatures for actuation. Usual approaches to induce entropic disorder and accordingly actuation in LCEs are based on heating and exposure to solvents. These approaches suffer from long response time due to their dependency on the heat and mass transfer of the system. Also, local and remote stimulation of the LCE materials without affecting the surrounding is very difficult. Addition of dopants, chemicals and nanoparticles might mitigate these challenges [232].

Different approaches have been introduced in the literature to tackle the above-mentioned problems for the use of LCEs/LCNs. The most common technique is based upon

inducing the disorder in the network of a LCE/LCN material by photo-isomerization of photo-chromophores that are doped into the network. Derivatives of azobenzene are the most common additives which are usually in form of mesogenic and rod-like molecules. Upon exposure to 360nm UV light, they undergo *cis-trans* isomerization so the network order diminishes upon bending of the rod-like mesogens during isomerization. The intensity and extent of isomerization crucially depends on the penetration depth of light. As the exposure is usually is heterogeneous and directional, only chromophores closer to surface will experience isomerization. Thus, most dominant mode of deformation is bending. It takes longer times and more intense lights to have a uniform contraction/expansion throughout the material [15,131,233].

The other strategy is based on the use of ferroelectric mesogens, e.g. bent-core liquid crystals, as dopants of reactants. For instance, main-chain ferroelectric chiral smectic C LCEs [234] and side-chain bent-core liquid crystal elastomers [235] show remarkably short response times. However, the extremely strong electrical field required to induce a very slight strain is the shortcoming of these systems [232]. Other approaches are based on resistive heating (Joule heating) by use of surface coatings [236,237] or embedded wires [238]. Usually mechanical mismatch between the LCE material and surface coating and internal wires leads to frustration of mechanical response and eventually cracking at the interface of dissimilar materials [232].

Last but not least, addition of the nanoparticles is shown as another possible technique to manipulate the properties of the LCE/LCN matrix. Due to the higher surface to volume ratio of the nanoparticles, their impact on the whole matrix is more pronounced. They might enhance the response time and give a better control over the stimulation techniques. Similar to other polymer/nanoparticle composites, the overall mechanical properties of the matrix can be improved by judicious selection of particles and the amount used [232]. Both carbon-based and non-carbon nanoparticles are used for manipulation of LCE properties. Dispersion of carbon black below percolation threshold is used for resistive heating [239]. CNT/LCE composites are synthesized and actuated with either broad spectrum light (e.g. IR) or electrical fields [217,240]. Non-carbon particles such as Fe_3O_4 are utilized for magnetic actuation of the LCE composites [241]. Hence, addition of nanoparticles to address the above-mentioned shortcoming appears to be rational and promising.

Bibliography

1. Shahsavan, H. & Zhao, B. Bioinspired functionally graded adhesive materials: synergetic interplay of top viscous–elastic layers with base micropillars. *Macromolecules* 47, 353–364 (2014).

2. Tian, Y. *et al.* Adhesion and friction in gecko toe attachment and detachment. *Proc. Natl. Acad. Sci. U. S. A.* 103, 19320–5 (2006).

3. Ohm, C., Brehmer, M. & Zentel, R. Liquid crystalline elastomers as actuators and sensors. *Adv. Mater.* 22, 3366–87 (2010).

4. Terentjev, E. M. Liquid-crystalline elastomers. *J. Phys. Condens. Matter* 11, R239–R257 (1999).

5. Lendlein, A., Jiang, H., Jünger, O. & Langer, R. Light-induced shape-memory polymers. *Nature* 434, 695–697 (2005).

6. Xie, P. & Zhang, R. Liquid crystal elastomers, networks and gels: advanced smart materials. *J. Mater. Chem.* 15, 2529 (2005).

7. Jiang, H. Y., Kelch, S. & Lendlein, A. Polymers move in response to light. *Adv. Mater.* 18, 1471–1475 (2006).

8. Li, M.-H. & Keller, P. Artificial muscles based on liquid crystal elastomers. *Philos. Trans. A. Math. Phys. Eng. Sci.* 364, 2763–77 (2006).

9. Behl, M. & Lendlein, A. Actively moving polymers. *Soft Matter* 3, 58 (2007).

10. Ikeda, T., Mamiya, J. & Yu, Y. Photomechanics of liquid-crystalline elastomers and other polymers. *Angew. Chem. Int. Ed. Engl.* 46, 506–28 (2007).

11. Buguin, A., Li, M.-H., Silberzan, P., Ladoux, B. & Keller, P. Micro-actuators: when artificial muscles made of nematic liquid crystal elastomers meet soft lithography. *J. Am. Chem. Soc.* 128, 1088–9 (2006).

12. Yang, H. *et al.* Micron-sized main-chain liquid crystalline elastomer actuators with ultralarge amplitude contractions. *J. Am. Chem. Soc.* 131, 15000–4 (2009).

13. Yang, H., Ye, G., Wang, X. & Keller, P. Micron-sized liquid crystalline elastomer actuators. *Soft Matter* 7, 815 (2011).

14. Honglawan, A. *et al.* Topographically induced hierarchical assembly and geometrical transformation of focal conic domain arrays in smectic liquid crystals. *Proc. Natl. Acad. Sci. U. S. A.* 110, 34–9 (2013).

15. van Oosten, C. L., Bastiaansen, C. W. M. & Broer, D. J. Printed artificial cilia from liquid-crystal network actuators modularly driven by light. *Nat. Mater.* 8, 677–82 (2009).

16.   Li, C. *et al.* Light-controlled quick switch of adhesion on a micro-arrayed liquid crystal polymer superhydrophobic film. *Soft Matter* 8, 3730 (2012).

17.   Liu, D. & Broer, D. J. Liquid crystal polymer networks: switchable surface topographies. *Liq. Cryst. Rev.* 1, 20–28 (2013).

18.   Shahsavan, H., Salili, S. M., Jákli, A. & Zhao, B. Smart muscle-driven self-cleaning of biomimetic microstructures from liquid crystal elastomers. *Adv. Mater.* 27, 6828–6833 (2015).

19.   Shahsavan, H., Salili, S. M., Jákli, A. & Zhao, B. Thermally active liquid crystal network gripper mimicking the self-peeling of gecko toe pads. *Adv. Mater.* 1–7 (2016). doi:10.1002/adma.201604021

20.   Good, R. J. Contact angle, wetting, and adhesion: a critical review. *J. Adhes. Sci. Technol.* 6, 1269–1302 (1992).

21.   Berg, J. in *Adhesion Science and Engineering* (ed. Chaudhury, M. K. and Pocius, A. D.) 2, 1–73 (Elsevier B.V., 2002).

22.   D. H. Bangham and R. I. Razouk. The Swelling of Charcoal. Part V. The saturation and immersion expansions and the heat of wetting. *Proc. R. Soc. Lond. A* 166, 572 (1938).

23.   Israelachvili, J. N. *Intermolecular and Surface Forces.* (Academic Press, 1992).

24.   Wenzel, R. N. Resistance of solid surfaces to wetting by water. *Ind. Eng. Chem.* 28, 988–994 (1936).

25.   Cassie, A. & Baxter, S. Wettability of porous surfaces. *Trans. Faraday Soc.* 40, 546–551 (1944).

26.   Crick, C. R. & Parkin, I. P. Preparation and characterisation of super-hydrophobic surfaces. *Chem. A Eur. J.* 16, 3568–88 (2010).

27.   Kendall, K. *Molecular Adhesion and Its Applications The Sticky Universe.* (Kluwer Academic/Plenum Publishers, 2001).

28.   Colchero, J., Meyer, E. & Marti, O. in *Handbook of Micro/Nanotribology* (ed. Bhushan, B.) 273–334 (CRC Press LLC, 1999).

29.   Maeda, N., Chen, N., Tirrell, M. & Israelachvili, J. N. Adhesion and friction mechanisms of polymer-on-polymer surfaces. *Science (80-.).* 297, 379–82 (2002).

30.   Kendall, K. in *Adhesion Science and Engineering Volume 1* (ed. Dillard, D.A.; Pocius, A. V.) 77–110 (Elsevier, 2002).

31.   Burnham, Nancy. A and Kulik, A. A. in *Handbook of Micro/Nanotribology* (ed. Bhushan, B.) 247–272 (CRC Press LLC, 1999).

32. Shull, K. R. in *Adhesion Science and Engineering Volume 1* (ed. Dillard, D.A.; Pocius, A.V.; Chaudhury, M.) 577–604 (Elsevier, 2002).

33. Johnson, K. L., Kendall, K. & Roberts, A. D. Surface energy and the contact of elastic solids. *Proc. R. Soc. A* 324, 301–313 (1971).

34. Gent, A. N. & Kinloch, A. J. Adhesion of viscoelastic materials to rigid substrates. III. Energy criterion for failure. *J. Polym. Sci. Part A-2 Polym. Phys.* 9, 659–668 (1971).

35. Andrews, E. H. & Kinloch, A. J. Mechanics of adhesive failure. I. *Proc. R. Soc. A* 332, 385–399 (1973).

36. Andrews, E. H. & Kinloch, A. J. Mechanics of adhesive failure. Ii. *Proc. R. Soc. A* 332, 401–414 (1973).

37. Packham, D. E. Some contributions of surface analysis to the development of adhesion theories. *J. Adhes.* 84, 240–255 (2008).

38. Persson, B. N. J. Biological adhesion for locomotion: basic principles. *J. Adhes. Sci. Technol.* 21, 1145–1173 (2007).

39. Sun, W., Neuzil, P., Kustandi, T. S., Oh, S. & Samper, V. D. The nature of the gecko lizard adhesive force. *Biophys. J.* 89, L14-7 (2005).

40. Drotlef, D.-M. *et al.* Insights into the adhesive mechanisms of tree frogs using artificial mimics. *Adv. Funct. Mater.* 23, 1137–1146 (2013).

41. Persson, B. N. J. On the mechanism of adhesion in biological systems. *J. Chem. Phys.* 118, 7614 (2003).

42. Gorb, S. N., Sinha, M., Peressadko, A., Daltorio, K. a & Quinn, R. D. Insects did it first: a micropatterned adhesive tape for robotic applications. *Bioinspir. Biomim.* 2, S117-25 (2007).

43. Autumn, K. *et al.* Evidence for van der Waals adhesion in gecko setae. *Proc. Natl. Acad. Sci. U. S. A.* 99, 12252–6 (2002).

44. Shahsavan, H., Arunbabu, D. & Zhao, B. Biomimetic modification of polymeric surfaces: a promising pathway for tuning of wetting and adhesion. *Macromol. Mater. Eng.* 297, 743–760 (2012).

45. Autumn, K. *et al.* Adhesive force of a single gecko foot-hair. *Nature* 405, 681–5 (2000).

46. Murphy, M. P., Aksak, B. & Sitti, M. Gecko-inspired directional and controllable adhesion. *Small* 5, 170–5 (2009).

47. Autumn, K., Dittmore, A., Santos, D., Spenko, M. & Cutkosky, M. Frictional adhesion: A new angle on gecko attachment. *J. Exp. Biol.* 209, 3569–79 (2006).

48. Bhushan, B. Adhesion of multi-level hierarchical attachment systems in gecko feet. *J. Adhes. Sci. Technol.* 21, 1213–1258 (2007).

49. Geim, A. K. *et al.* Microfabricated adhesive mimicking gecko foot-hair. *Nat. Mater.* 2, 461–3 (2003).

50. Greiner, C., Campo, A. Del & Arzt, E. Adhesion of bioinspired micropatterned surfaces: effects of pillar radius, aspect ratio, and preload. *Langmuir* 23, 3495–502 (2007).

51. Shahsavan, H. & Zhao, B. Conformal adhesion enhancement on biomimetic microstructured surfaces. *Langmuir Acs J. Surfaces Colloids* 27, 7732–7742 (2011).

52. del Campo, A., Greiner, C., Alvarez, I. & Arzt, E. Patterned surfaces with pillars with controlled 3d tip geometry mimicking bioattachment devices. *Adv. Mater.* 19, 1973–1977 (2007).

53. Murphy, M. P., Kim, S. & Sitti, M. Enhanced adhesion by gecko-inspired hierarchical fibrillar adhesives. *ACS Appl. Mater. Interfaces* 1, 849–55 (2009).

54. Jeong, H. E., Lee, J.-K., Kim, H. N., Moon, S. H. & Suh, K. Y. A nontransferring dry adhesive with hierarchical polymer nanohairs. *Proc. Natl. Acad. Sci. U. S. A.* 106, 5639–44 (2009).

55. Glassmaker, N. J., Jagota, A., Hui, C.-Y., Noderer, W. L. & Chaudhury, M. K. Biologically inspired crack trapping for enhanced adhesion. *Proc. Natl. Acad. Sci. U. S. A.* 104, 10786–91 (2007).

56. Shahsavan, H. & Zhao, B. Biologically inspired enhancement of pressure-sensitive adhesives using a thin film-terminated fibrillar interface. *Soft Matter* 8, 8281–8284 (2012).

57. Bae, W., Kim, D. & Suh, K. Instantly switchable adhesion of bridged fibrillar adhesive via gecko-inspired detachment mechanism and its application to a transportation system. *Nanoscale* 5, 11786–11884 (2013).

58. Majumder, A., Ghatak, A. & Sharma, A. Microfluidic adhesion induced by subsurface microstructures. *Science.* 318, 258–61 (2007).

59. Arzt, E., Gorb, S. & Spolenak, R. From micro to nano contacts in biological attachment devices. *Proc. Natl. Acad. Sci. U. S. A.* 100, 10603–6 (2003).

60. Hui, C.-Y., Glassmaker, N. J. & Jagota, A. How compliance compensates for surface roughness in fibrillar adhesion. *J. Adhes.* 81, 699–721 (2005).

61. Kim, S. & Sitti, M. Biologically inspired polymer microfibers with spatulate tips as repeatable fibrillar adhesives. *Appl. Phys. Lett.* 89, 261911 (2006).

62. Autumn, K. & Peattie, A. M. Mechanisms of adhesion in geckos. *Integr. Comp. Biol.* 42, 1081–90 (2002).

63. Spolenak, R., Gorb, S., Gao, H. & Arzt, E. Effects of contact shape on the scaling of biological attachments. *Proc. R. Soc. A* 461, 305–319 (2005).

64. Bhushan, B., Peressadko, A. G. & Kim, T.-W. Adhesion analysis of two-level hierarchical morphology in natural attachment systems for 'smart adhesion'. *J. Adhes. Sci. Technol.* 20, 1475–1491 (2006).

65. Yao, H. & Gao, H. Mechanics of robust and releasable adhesion in biology: Bottom–up designed hierarchical structures of gecko. *J. Mech. Phys. Solids* 54, 1120–1146 (2006).

66. Schargott, M., Popov, V. L. & Gorb, S. Spring model of biological attachment pads. *J. Theor. Biol.* 243, 48–53 (2006).

67. Glassmaker, N. J., Himeno, T., Hui, C.-Y. & Kim, J. Design of biomimetic fibrillar interfaces: 1. Making contact. *J. R. Soc. Interface* 1, 23–33 (2004).

68. Jagota, A. & Bennison, S. J. Mechanics of adhesion through a fibrillar microstructure. *Integr. Comp. Biol.* 42, 1140–5 (2002).

69. Lamblet, M. *et al.* Adhesion enhancement through micropatterning at polydimethylsiloxane-acrylic adhesive interfaces. *Langmuir* 23, 6966–74 (2007).

70. Kendall, K. Thin-film peeling-the elastic term. *J. Phys. D. Appl. Phys.* 8, 1449 (1975).

71. Shahsavan, H. & Zhao, B. Gecko-inspired pressure sensitive adhesives: a new class of hybrid adhesives. in *33rd Annual Meeting of Adhesion Society* (2013).

72. Cheung, E. & Sitti, M. Enhancing Adhesion of Biologically Inspired Polymer Microfibers with a Viscous Oil Coating. *J. Adhes.* 87, 547–557 (2011).

73. Patil, S., Mangal, R., Malasi, A. & Sharma, A. Biomimetic wet adhesion of viscoelastic liquid films anchored on micropatterned elastic substrates. *Langmuir* 28, 14784–91 (2012).

74. Carelli, C., Déplace, F., Boissonnet, L. & Creton, C. Effect of a gradient in viscoelastic properties on the debonding mechanisms of soft adhesives. *J. Adhes.* 83, 491–505 (2007).

75. Patil, S., Malasi, A., Majumder, A., Ghatak, A. & Sharma, A. Reusable antifouling viscoelastic adhesive with an elastic skin. *Langmuir* 28, 42–6 (2012).

76. Zhou, M. *et al.* Controllable interfacial adhesion applied to transfer light and fragile objects by using gecko inspired mushroom-shaped pillar surface. *ACS Appl. Mater. Interfaces* (2013).

77. Zheng, Y., Gao, X. & Jiang, L. Directional adhesion of superhydrophobic butterfly wings. *Soft Matter* 3, 178 (2007).

78. Zheng, Y. *et al.* Directional water collection on wetted spider silk. *Nature* 463, 640–643 (2010).

79. Hancock, M. J., Sekeroglu, K. & Demirel, M. C. Bioinspired Directional Surfaces for Adhesion, Wetting, and Transport. *Adv. Funct. Mater.* 22, 2223–2234 (2012).

80. Shastry, A., Marianne, J. & Böhringer, K. Directing droplets using microstructured surfaces. *Langmuir* 6161–6167 (2006).

81. Sitti, M. *et al.* Dangling chain elastomers as repeatable fibrillar adhesives. *ACS Appl. Mater. Interfaces* 1, 2277–87 (2009).

82. Sidorenko, A., Krupenkin, T., Taylor, A., Fratzl, P. & Aizenberg, J. Reversible Switching of hyderogel-actuated nanostructures into complex micropatterns. *Science.* 315, 487–490 (2007).

83. Zarzar, L. D. *et al.* Multifunctional actuation systems responding to chemical gradients. *ACS Nano* 4, 6323–31 (2010).

84. Zarzar, L. D., Kim, P. & Aizenberg, J. Bio-inspired design of submerged hydrogel-actuated polymer microstructures operating in response to pH. *Adv. Mater.* 23, 1442–6 (2011).

85. Zarzar, L. D. *et al.* Direct writing and actuation of three-dimensionally patterned hydrogel pads on micropillar supports. *Angew. Chem. Int. Ed. Engl.* 50, 9356–60 (2011).

86. Kim, P., Zarzar, L. D., He, X., Grinthal, A. & Aizenberg, J. Hydrogel-actuated integrated responsive systems (HAIRS): Moving towards adaptive materials. *Curr. Opin. Solid State Mater. Sci.* 15, 236–245 (2011).

87. Zarzar, L. D. *et al.* Multifunctional actuation systems responding to chemical gradients. *Soft Matter* 8, 8289 (2012).

88. Reddy, S., Arzt, E. & del Campo, A. Bioinspired surfaces with switchable adhesion. *Adv. Mater.* 19, 3833–3837 (2007).

89. Cui, J. *et al.* Bioinspired actuated adhesive patterns of liquid crystalline elastomers. *Adv. Mater.* 24, 4601–4 (2012).

90. Jeong, H. E., Kwak, M. K. & Suh, K. Y. Stretchable, adhesion-tunable dry adhesive by surface wrinkling. *Langmuir* 26, 2223–6 (2010).

91. Krahn, J. & Menon, C. Electro-Dry-Adhesion. *Langmuir* 28, 5438–5443 (2012).

92. Liu, D. & Broer, D. J. Light controlled friction at a liquid crystal polymer coating with switchable patterning. *Soft Matter* 10, 7952–8 (2014).

93. Mahdavi, A. *et al.* A biodegradable and biocompatible gecko-inspired tissue adhesive. *Proc. Natl. Acad. Sci. U. S. A.* 105, 2307–12 (2008).

94. Mengüç, Y., Yang, S. Y., Kim, S., Rogers, J. A. & Sitti, M. Gecko-inspired controllable adhesive structures applied to micromanipulation. *Adv. Funct. Mater.* 22, 1246–1254

(2012).

95.   Kim, S. *et al.* Microstructured elastomeric surfaces with reversible adhesion and examples of their use in deterministic assembly by transfer printing. *Proc. Natl. Acad. Sci. U. S. A.* 107, 17095–100 (2010).

96.   Tian, Y., Wan, J., Pesika, N. & Zhou, M. Bridging nanocontacts to macroscale gecko adhesion by sliding soft lamellar skin supported setal array. *Sci. Rep.* 3, 1382 (2013).

97.   Isla, P. Y. & Kroner, E. A novel bioinspired switchable adhesive with three distinct adhesive states. *Adv. Funct. Mater.* 25, 2444-2450 (2015).

98.   Purtov, J., Frensemeier, M. & Kroner, E. Switchable Adhesion in Vacuum Using Bio-Inspired Dry Adhesives. *ACS Appl. Mater. Interfaces* 7, 24127–24135 (2015).

99.   Tao, X. & Xingcheng, X. Self-peeling reversible dry adhesive system. *Chem. Mater.* 20, 2866–2868 (2008).

100.   Guo, D.-J. *et al.* Reverse adhesion of a gecko-inspired synthetic adhesive switched by an ion-exchange polymer–metal composite actuator. *ACS Appl. Mater. Interfaces.* 7, 5480-5487 (2015).

101.   Song, S. & Sitti, M. Soft grippers using micro-fibrillar adhesives for transfer printing. *Adv. Mater.* 26, 4901–4906 (2014).

102.   Collings Peter J., M. H. *Introduction to liquid crystals: chemistry and physics.* (CRC Press, 1997).

103.   Gibbons, W. M., Shannon, P. J., Sun, S.-T. & Swetlin, B. J. Surface-mediated alignment of nematic liquid crystals with polarized laser light. *Nature* 351, 49–50 (1991).

104.   Chaudhari, P. *et al.* Atomic-beam alignment of inorganic materials for liquid-crystal displays. *Nature* 411, 56–9 (2001).

105.   Uchida, T., Ohgawara, M. & Wada, M. Liquid Crystal Orientation on the Surface of Obliquely-Evaporated Silicon Monoxide with Homeotropic Surface Treatment. *Jpn. J. Appl. Phys.* 19, 2127–2136 (1980).

106.   Berreman, D. W. Alignment of liquid crystals by grooved surfaces. *Mol. Cryst. Liq. Cryst.* 23, 215–231 (1973).

107.   Seki, T. *et al.* 'Command surfaces' of Langmuir-Blodgett films. Photoregulations of liquid crystal alignment by molecularly tailored surface azobenzene layers. *Langmuir* 9, 211–218 (1993).

108.   Ohm, C., Serra, C. & Zentel, R. A continuous flow synthesis of micrometer-sized actuators from liquid crystalline elastomers. *Adv. Mater.* 21, 4859–62 (2009).

109.   Osada, Yoshihito; Okuzaki, Hidenori; Hori, H. *Nature* 355, 242–244 (1992).

110. van Oosten, C. L. Responsive Liquid Crystal Networks. (Eindhoven University of Technology, 2009).

111. Pelrine, R., Kornbluh, R. & Kofod, G. High-strain actuator materials based on dielectric elastomers. *Adv. Mater.* 12, 1223–1225 (2000).

112. Mirfakhrai, T., Madden, J. D. W. & Baughman, R. H. Polymer artificial muscles. *Mater. Today* 10, 30–38 (2007).

113. Pelrine, R. High-Speed Electrically Actuated Elastomers with Strain Greater Than 100%. *Science.* 287, 836–839 (2000).

114. Brochu, P. & Pei, Q. Advances in dielectric elastomers for actuators and artificial muscles. *Macromol. Rapid Commun.* 31, 10–36 (2010).

115. Biggs, J. *et al.* Electroactive polymers: Developments of and perspectives for dielectric elastomers. *Angew. Chemie-Int. Ed.* 52, 9409–9421 (2013).

116. O'Halloran, A., O'Malley, F. & McHugh, P. A review on dielectric elastomer actuators, technology, applications, and challenges. *J. Appl. Phys.* 104, (2008).

117. Shian, S., Bertoldi, K. & Clarke, D. R. Dielectric elastomer based 'grippers' for soft robotics. *Adv. Mater.* 27, 6814-6819 (2015).

118. Ware, T. H., McConney, M. E., Wie, J. J., Tondiglia, V. P. & White, T. J. Voxelated liquid crystal elastomers. *Science.* 347, 982–984 (2015).

119. Verduzco, R. Shape-shifting liquid crystals. *Science.* 347, 949–950 (2015).

120. Davis, F. J. Liquid-crystalline elastomers. *J. Mater. Chem.* 3, 551 (1993).

121. Jiang, H., Li, C. & Huang, X. Actuators based on liquid crystalline elastomer materials. *Nanoscale* 5, 5225–40 (2013).

122. de Gennes, P.-G. Un muscle artificiel semi-rapide. *Comptes Rendus l'Académie des Sci. IIB-Mechanics-Physics-Chemistry-Astronomy* 324, 343–348 (1997).

123. Finkelmann, Heino, Hans-J. Kock, and G. R. Investigations on liquid crystalline polysiloxanes 3. Liquid crystalline elastomers — a new type of liquid crystalline material. *Macromol. Rapid Commun.* 2, 317–322 (1981).

124. Woltman, S. J., Jay, G. D. & Crawford, G. P. Liquid-crystal materials find a new order in biomedical applications. *Nat. Mater.* 6, 929–38 (2007).

125. Sánchez-Ferrer, A. *et al.* Photo-crosslinked side-chain liquid-crystalline elastomers for microsystems. *Macromol. Chem. Phys.* 210, 1671–1677 (2009).

126. Sánchez-Ferrer, A. *et al.* Liquid-crystalline elastomer microvalve for microfluidics. *Adv. Mater.* 23, 4526–30 (2011).

127. Camacho-Lopez, M., Finkelmann, H., Palffy-Muhoray, P. & Shelley, M. Fast liquid-crystal elastomer swims into the dark. *Nat. Mater.* 3, 307–10 (2004).

128. Yan, Z., Ji, X., Wu, W., Wei, J. & Yu, Y. Light-switchable behavior of a microarray of azobenzene liquid crystal polymer induced by photodeformation. *Macromol. Rapid Commun.* 33, 1362–7 (2012).

129. Wu, Z. L. *et al.* Microstructured Nematic Liquid Crystalline Elastomer Surfaces with Switchable Wetting Properties. *Adv. Funct. Mater.* 23, 3070–3076 (2013).

130. Wu, Z. L. *et al.* Stimuli-responsive topological change of microstructured surfaces and the resultant variations of wetting properties. *ACS Appl. Mater. Interfaces* 5, 7485–91 (2013).

131. Ikeda, T., Nakano, M., Yu, Y., Tsutsumi, O. & Kanazawa, A. Anisotropic Bending and Unbending Behavior of Azobenzene Liquid-Crystalline Gels by Light Exposure. *Adv. Mater.* 15, 201–205 (2003).

132. Kondo, M., Yu, Y. & Ikeda, T. How does the initial alignment of mesogens affect the photoinduced bending behavior of liquid-crystalline elastomers? *Angew. Chemie* 118, 1406–1410 (2006).

133. Elias, A., Brett, M., Harris, K., Bastiaansen, C. & Broer, D. Three Techniques for Micropatterning Liquid Crystalline Polymers. *Mol. Cryst. Liq. Cryst.* 477, 137–151 (2007).

134. Yang, Z. *et al.* Thermal and UV shape shifting of surface topography. *J. Am. Chem. Soc.* 128, 1074–5 (2006).

135. Cviklinski, J., Tajbakhsh, a R. & Terentjev, E. M. UV isomerisation in nematic elastomers as a route to photo-mechanical transducer. *Eur. Phys. J. E. Soft Matter* 9, 427–34 (2002).

136. Ohm, C., Haberkorn, N., Theato, P. & Zentel, R. Template-based fabrication of nanometer-scaled actuators from liquid-crystalline elastomers. *Small* 7, 194–8 (2011).

137. Elias, a. L., Harris, K. D., Bastiaansen, C. W. M., Broer, D. J. & Brett, M. J. Photopatterned liquid crystalline polymers for microactuators. *J. Mater. Chem.* 16, 2903 (2006).

138. Liu, D., Bastiaansen, C. W. M., den Toonder, J. M. J. & Broer, D. J. Photo-switchable surface topologies in chiral nematic coatings. *Angew. Chem. Int. Ed. Engl.* 51, 892–6 (2012).

139. Sousa, M. E., Broer, D. J., Bastiaansen, C. W. M., Freund, L. B. & Crawford, G. P. Isotropic 'islands' in a cholesteric 'sea': patterned thermal expansion for responsive surface topologies. *Adv. Mater.* 18, 1842–1845 (2006).

140. Jagota, A. & Hui, C.-Y. Adhesion, friction, and compliance of bio-mimetic and bio-inspired structured interfaces. *Mater. Sci. Eng. R Reports* 72, 253–292 (2011).

141. Ashurst, W., Carraro, C., Maboudian, R., Frey, W. Wafer level anti-stiction coatings for MEMS. *Sensors Actuators A Phys.* 104, 213–221 (2003).

142. Nase, J., Lindner, A. & Creton, C. Pattern formation during deformation of a confined viscoelastic layer: from a viscous liquid to a soft elastic solid. *Phys. Rev. Lett.* 101, 1–4 (2008).

143. Nadermann, N., Ning, J., Jagota, A. & Hui, C.-Y. Active switching of adhesion in a film-terminated fibrillar structure. *Langmuir* 26, 15464–71 (2010).

144. Mukherjee, R., Pangule, R. C., Sharma, A. & Banerjee, I. Contact instability of thin elastic films on patterned substrates. *J. Chem. Phys.* 127, 64703 (2007).

145. Shen, L., Hui, C.-Y. & Jagota, A. A two-dimensional model for enhanced adhesion of film-terminated fibrillar interfaces by crack trapping. *J. Appl. Phys.* 104, 123506 (2008).

146. Liu, J., Hui, C. Y. & Jagota, A. Effect of fibril arrangement on crack trapping in a film-terminated fibrillar interface. *J. Polym. Sci. Part B Polym. Phys.* 47, 2368–2384 (2009).

147. Crosby, A. & Shull, K. Adhesive failure analysis of pressure-sensitive adhesives. *J. Polym. Sci. Part B.* 37, 3455–3472 (1999).

148. Gent, A, N and Hamed, G, R. Peel mechanics of adhesive joints. *Polym. Eng. Sci.* 17, 462–466 (1977).

149. Nase, J., Ramos, O., Creton, C. & Lindner, A. Debonding energy of PDMS: A new analysis of a classic adhesion scenario. *Eur. Phys. J. E. Soft Matter* 36, 103 (2013).

150. Paiva, A., Sheller, N. & Foster, M. Microindentation and nanoindentation studies of aging in pressure-sensitive adhesives. *Macromolecules* 2269–2276 (2001).

151. Creton, C. & Leibler, L. How does tack depend on time of contact and contact pressure? *J. Polym. Sci. Part B Polym. Phys.* 34, 545–554 (1996).

152. Suresh, S. Graded materials for resistance to contact deformation and damage. *Science.* 292, 2447–51 (2001).

153. Guo, X., Jin, F. & Gao, H. Mechanics of non-slipping adhesive contact on a power-law graded elastic half-space. *Int. J. Solids Struct.* 48, 2565–2575 (2011).

154. Yao, H. & Gao, H. Mechanical principles of robust and releasable adhesion of gecko. *J. Adhes. Sci. Technol.* 21, 1185–1212 (2007).

155. Long, R. & Hui, C.-Y. The effect of preload on the pull-off force in indentation tests of microfibre arrays. *Proc. R. Soc. A* 465, 961–981 (2009).

156. Noderer, W. L. *et al.* Enhanced adhesion and compliance of film-terminated fibrillar surfaces. *Proc. R. Soc. A Math. Phys. Eng. Sci.* 463, 2631–2654 (2007).

157. Liu, J., Hui, C.-Y., Shen, L. & Jagota, A. Compliance of a microfibril subjected to shear and normal loads. *J. R. Soc. Interface* 5, 1087–97 (2008).

158. Greenwood, J. & Johnson, K. The mechanics of adhesion of viscoelastic solids. *Philos. Mag. A* 37–41 (1981).

159. Falsafi, A. Direct measurement of adhesion between viscoelastic polymers: A contact mechanical approach. *J. Rheol. (N. Y. N. Y).* 41, 1349 (1997).

160. Hui, C., Baney, J. M. & Kramer, E. J. Contact Mechanics and Adhesion of Viscoelastic Spheres. *Langmuir* 14, 6570–6578 (1998).

161. Oliver, W. C. & Pharr, G. M. An improved technique for determining hardness and elastic modulus using load and displacement sensing indentation experiments. *J. Mater. Res.* 7, 1564–1583 (1992).

162. Herbert, E. & Oliver, W. Measuring the constitutive behavior of viscoelastic solids in the time and frequency domain using flat punch nanoindentation. *J. Mater. Res.* 24, 626–637 (2009).

163. Tawfick, S. *et al.* Engineering of micro- and nanostructured surfaces with anisotropic geometries and properties. *Adv. Mater.* 24, 1628–1674 (2012).

164. Dahlquist, C. A. An investigation into the nature of tack. *Adhes. Age* 2, 25–29 (1959).

165. Brochard, F. & De Gennes, P. G. Shear-dependent slippage at a polymer/solid interface. *Langmuir* 8, 3033–3037 (1992).

166. Newby, B. M., Chaudhury, M. K. & Brown, H. R. Macroscopic evidence of the effect of interfacial slippage on adhesion. *Science.* 269, 1407–9 (1995).

167. Zhang Newby, B. & Chaudhury, M. K. Effect of Interfacial Slippage on Viscoelastic Adhesion. *Langmuir* 13, 1805–1809 (1997).

168. Zhang Newby, B. & Chaudhury, M. K. Friction in Adhesion. *Langmuir* 14, 4865–4872 (1998).

169. Brown, H. Chain pullout and mobility effects in friction and lubrication. *Science.* 263, 1411–1413 (1994).

170. Miserez, A., Schneberk, T., Sun, C., Zok, F. W. & Waite, J. H. The transition from stiff to compliant materials in squid beaks. *Science.* 319, 1816–9 (2008).

171. Guler, M. a. & Erdogan, F. Contact mechanics of two deformable elastic solids with graded coatings. *Mech. Mater.* 38, 633–647 (2006).

172. Chen, S., Yan, C., Zhang, P. & Gao, H. Mechanics of adhesive contact on a power-law graded elastic half-space. *J. Mech. Phys. Solids* 57, 1437–1448 (2009).

173. Gu, Y., Nakamura, T. & Prchlik, L. Micro-indentation and inverse analysis to characterize elastic–plastic graded materials. *Mater. Sci. Eng. A* A345, 223–233 (2003).

174. Nakamura, T., Wang, T. & Sampath, S. Determination of properties of graded materials by inverse analysis and instrumented indentation. *Acta Mater.* 48, 4293–4306 (2000).

175. Gao, H. & Yao, H. Shape insensitive optimal adhesion of nanoscale fibrillar structures. *Proc. Natl. Acad. Sci. U. S. A.* 101, 7851–7856 (2004).

176. Autumn, K. & Hansen, W. Ultrahydrophobicity indicates a non-adhesive default state in gecko setae. *J. Comp. Physiol. A. Neuroethol. Sens. Neural. Behav. Physiol.* 192, 1205–12 (2006).

177. Barthlott, W. & Neinhuis, C. Purity of the sacred lotus, or escape from contamination in biological surfaces. *Planta* 202, 1–8 (1997).

178. Guo, C. *et al.* Biomechanism of adhesion in gecko setae. *Sci. China Life Sci.* 55, 181–187 (2012).

179. Hu, S., Lopez, S., Niewiarowski, P. H. & Xia, Z. Dynamic self-cleaning in gecko setae via digital hyperextension. *J. R. Soc. Interface* 9, 2781–2790 (2012).

180. Autumn, K. & Peattie, A. M. Mechanisms of adhesion in geckos. *Integr. Comp. Biol.* 42, 1081–1090 (2002).

181. Zhao, Y. *et al.* Interfacial energy and strength of multiwalled-carbon-nanotube-based dry adhesive. *J. Vac. Sci. Technol. B Microelectron. Nanom. Struct.* 24, 331 (2006).

182. Northen, M. T., Greiner, C., Arzt, E. & Turner, K. L. A gecko-inspired reversible adhesive. *Adv. Mater.* 20, 3905–3909 (2008).

183. Reddy, S., Arzt, E. & del Campo, a. Bioinspired Surfaces with Switchable Adhesion. *Adv. Mater.* 19, 3833–3837 (2007).

184. Kim, S., Sitti, M., Xie, T. & Xiao, X. Reversible dry micro-fibrillar adhesives with thermally controllable adhesion. *Soft Matter* 5, 3689 (2009).

185. Frensemeier, M. *et al.* Temperature-Induced Switchable Adhesion using Nickel-Titanium-Polydimethylsiloxane Hybrid Surfaces. *Adv. Funct. Mater.* 25, 3013–3021 (2015).

186. Drotlef, D. M., Blümler, P. & Del Campo, A. Magnetically actuated patterns for bioinspired reversible adhesion (dry and wet). *Adv. Mater.* 26, 775–779 (2014).

187. Cui, J. *et al.* Bioinspired actuated adhesive patterns of liquid crystalline elastomers. *Adv. Mater.* 24, 4601–4 (2012).

188. Liu, D. & Broer, D. J. Self-assembled dynamic 3d fingerprints in liquid-crystal coatings towards controllable friction and adhesion. *Angew. Chemie* 126, 4630–4634 (2014).

189. Wu, D. *et al.* Curvature-driven reversible in situ switching between pinned and roll-down superhydrophobic states for water droplet transportation. *Adv. Mater.* 23, 545–549 (2011).

190. Guo, D.-J. *et al.* Reverse adhesion of a gecko-inspired synthetic adhesive switched by an ion-exchange polymer–metal composite actuator. *ACS Appl. Mater. Interfaces* 7, 5480–5487 (2015).

191. Li, M.-H. & Keller, P. Artificial muscles based on liquid crystal elastomers. *Philos. Trans. A. Math. Phys. Eng. Sci.* 364, 2763–2777 (2006).

192. Jürgen Küpfer & Inkelmann, H. Nematic liquid single crystal elastomers. *Die Makromol. Chemie, Rapid Commun.* 12, 717–726 (1991).

193. Hikmet, R. A. M. & Broer, D. J. Dynamic mechanical properties of anisotropic networks formed by liquid crystalline acrylates. *Polymer (Guildf).* 32, 1627–1632 (1991).

194. Mol, G. N., Harris, K. D., Bastiaansen, C. W. M. & Broer, D. J. Thermo-mechanical responses of liquid-crystal networks with a splayed molecular organization. *Adv. Funct. Mater.* 15, 1155–1159 (2005).

195. De Haan, L. T. *et al.* Accordion-like actuators of multiple 3D patterned liquid crystal polymer films. *Adv. Funct. Mater.* 24, 1251–1258 (2014).

196. Liu, D. & Broer, D. J. Liquid crystal polymer networks: preparation, properties, and applications of films with patterned molecular alignment. *Langmuir* 30, 13499–13509 (2014).

197. Sawa, Y. *et al.* Shape selection of twist-nematic-elastomer ribbons. *Proc. Natl. Acad. Sci. U. S. A.* 108, 6364–6368 (2011).

198. Sawa, Y., Urayama, K., Takigawa, T., Desimone, A. & Teresi, L. Thermally driven giant bending of liquid crystal elastomer films with hybrid alignment. *Macromolecules* 43, 4362–4369 (2010).

199. Warner, M., Modes, C. D. & Corbett, D. Suppression of curvature in nematic elastica. *Proc. R. Soc. A Math. Phys. Eng. Sci.* 466, 3561–3578 (2010).

200. Chen, Z., Majidi, C., Srolovitz, D. J. & Haataja, M. P. Continuum Elasticity Theory Approach for Spontaneous Bending and Twisting of Ribbons Induced by Mechanical Anisotropy. *arXive*, 1209.3321v1 (2012).

201. Harden, J., Teeling, R., Gleeson, J. T., Sprunt, S. & Jákli, a. Converse flexoelectric effect in a bent-core nematic liquid crystal. *Phys. Rev. E* 78, 31702 (2008).

202.   Xia, F. & Jiang, L. Bio-inspired, smart, multiscale interfacial materials. *Adv. Mater.* 20, 2842–2858 (2008).

203.   Lafuma, A. & Quéré, D. Superhydrophobic states. *Nat. Mater.* 2, 457–460 (2003).

204.   Kim, S., Cheung, E. & Sitti, M. Wet self-cleaning of biologically inspired elastomer mushroom shaped microfibrillar adhesives. *Langmuir* 25, 7196–9 (2009).

205.   Kemp, J. C. Piezo-optical birefringence modulators: new use for a long-known effect. *J. Opt. Soc. Am.* 59, 950–953 (1969).

206.   Ostapenko, T., Zhang, C., Sprunt, S. N., Jákli, A. & Gleeson, J. T. Magneto-optical technique for detecting the biaxial nematic phase. *Phys. Rev. E - Stat. Nonlinear, Soft Matter Phys.* 84, 1–5 (2011).

207.   Iglesias, W., Abbott, N. L., Mann, E. K. & Jakli, A. Improving liquid crystal-based biosensing in aqueous phases. *ACS Appl. Mater. Interfaces* 2, 4–10 (2012).

208.   Pesika, N. *et al.* Peel-zone model of tape peeling based on the gecko adhesive system. *J. Adhes.* 83, 383–401 (2007).

209.   Autumn, K. *et al.* Dynamics of geckos running vertically. *J. Exp. Biol.* 209, 260–72 (2006).

210.   del Campo, A. & Arzt, E. Fabrication approaches for generating complex micro- and nanopatterns on polymeric surfaces. *Chem. Rev.* 108, 911–45 (2008).

211.   Sameoto, D. & Menon, C. Recent advances in the fabrication and adhesion testing of biomimetic dry adhesives. *Smart Mater. Struct.* 19, 103001 (2010).

212.   del Campo, A., Greiner, C. & Arzt, E. Contact shape controls adhesion of bioinspired fibrillar surfaces. *Langmuir* 23, 10235–43 (2007).

213.   Noderer, W. L. *et al.* Enhanced adhesion and compliance of film-terminated fibrillar surfaces. *Proc. R. Soc. A* 463, 2631–2654 (2007).

214.   Zhou, M. *et al.* Controllable interfacial adhesion applied to transfer light and fragile objects by using gecko inspired mushroom-shaped pillar surface. *ACS Appl. Mater. Interfaces* 5, 10137–10144 (2013).

215.   Kim, S. *et al.* Whole body adhesion: Hierarchical, directional and distributed control of adhesive forces for a climbing robot. *Proc. - IEEE Int. Conf. Robot. Autom.* 1268–1273 (2007).

216.   Xu, Q. *et al.* Robust self-cleaning and micromanipulation capabilities of gecko spatulae and their bio-mimics. *Nat. Commun.* 6, 8949 (2015).

217.   Kohlmeyer, R. R. & Chen, J. Wavelength-selective, IR light-driven hinges based on liquid crystalline elastomer composites. *Angew. Chemie-Int. Ed.* 52, 9234–9237 (2013).

218. Liu, K. *et al.* Giant-amplitude, high-work density microactuators with phase transition activated nanolayer bimorphs. *Nano Lett.* 12, 6302–6308 (2012).

219. Yun, G., Kim, H. S. & Kim, J. Blocked force measurement of an electro-active paper actuator using a cantilevered force transducer. *Smart Mater. Struct.* 17, 25021 (2008).

220. Kim, J., Kang, Y. & Yun, S. Blocked force measurement of electro-active paper actuator by micro-balance. *Sensors Actuators, A Phys.* 133, 401–406 (2007).

221. Clarke, E., Kroening, D. & Lerda, F. A Tool for Checking ANSI-C Programs. *Tools Algorithms Constr. Anal. Syst.* 2988, 168–176 (2004).

222. Wood, R. J., Steltz, E. & Fearing, R. S. Optimal energy density piezoelectric bending actuators. *Sensors Actuators A Phys.* 119, 476–488 (2005).

223. van Oosten, Casper L., *et al.* Bending dynamics and directionality reversal in liquid crystal network photoactuators. *Macromolecules* 41, 8592-8596. (2008) .

224. Liu, J., Hui, C. Y. & Jagota, A. Effect of fibril arrangement on crack trapping in a film-terminated fibrillar interface. *J. Polym. Sci. Part B Polym. Phys.* 47, 2368–2384 (2009).

225. Feng, X. *et al.* Competing fracture in kinetically controlled transfer printing. *Langmuir* 23, 12555–12560 (2007).

226. Vajpayee, S., Long, R., Shen, L., Jagota, A. & Hui, C.-Y. Effect of rate on adhesion and static friction of a film-terminated fibrillar interface. *Langmuir* 25, 2765–71 (2009).

227. Abusomwan, U. & Sitti, M. Effect of retraction speed on adhesion of elastomer fibrillar structures. *Appl. Phys. Lett.* 101, 211907 (2012).

228. Labonte, D. & Federle, W. Rate-dependence of 'wet' biological adhesives and the function of the pad secretion in insects. *Soft Matter* 11, 8661–8673 (2015).

229. White, T. J. & Broer, D. J. Programmable and adaptive mechanics with liquid crystal polymer networks and elastomers. *Nat. Mater.* 14, 1087–98 (2015).

230. Bartlett, M. D., Croll, A. B. & Crosby, A. J. Designing bio-inspired adhesives for shear loading: From simple structures to complex patterns. *Adv. Funct. Mater.* 22, 4985–4992 (2012).

231. Liew, K., Shahsavan, H. & Zhao, B. Functionally graded dry adhesives based on film-terminated silicone foam. *Int. J. Adhes. Adhes.* in-press, (2017). (doi.org/10.1016/j.ijadhadh.2017.02.009)

232. Ji, Y., Marshall, J. E. & Terentjev, E. M. Nanoparticle-liquid crystalline elastomer composites. *Polymers (Basel).* 4, 316–340 (2012).

233. Yamada, M. *et al.* Photomobile polymer materials: towards light-driven plastic motors. *Angew. Chem. Int. Ed. Engl.* 47, 4986–8 (2008).

234. Heinze, P. & Finkelmann, H. Shear deformation and ferroelectricity in chiral SmC* main-chain elastomers. *Macromolecules* 43, 6655–6665 (2010).

235. Verduzco, R. *et al.* Bent-core liquid crystal elastomers. *J. Mater. Chem.* 20, 8488 (2010).

236. Chambers, M. *et al.* Investigations on an integrated conducting nanoparticle–liquid crystal elastomer layer. *Nanotechnology* 18, 415706 (2007).

237. Chambers, M. *et al.* Liquid crystal elastomer–nanoparticle systems for actuation. *J. Mater. Chem.* 19, 1524–1531 (2009).

238. Huang, Y. Y., Biggins, J., Ji, Y. & Terentjev, E. M. Mechanical bistability in liquid crystal elastomer-wire composite actuators. *J. Appl. Phys.* 107, (2010).

239. Kim, H. *et al.* Preparation of Monodomain liquid crystal elastomers and liquid crystal elastomer nanocomposites. *ACS Macro Lett.* 5, 1386-1390 (2016).

240. Courty, S., Mine, J., Tajbakhsh, A. R. & Terentjev, E. M. Nematic elastomers with aligned carbon nanotubes: New electromechanical actuators. *Europhys. Lett.* 64, 654–660 (2003).

241. Kaiser, A., Winkler, M., Krause, S., Finkelmann, H. & Schmidt, A. M. Magnetoactive liquid crystal elastomer nanocomposites. *J. Mater. Chem.* 19, 538 (2009).

Appendix
Birefringence experiments and measurement of alignment and pretilt angle of mesogens in PDMS-LCE confined systems

Birefringence experiments

The phase differences of the planar and splayed LCE film, $\varphi = 2\pi\Delta n_{eff}d/\lambda$, ($\Delta n_{eff}$ is the effective birefringence of the sample) were measured by a technique described in [205,206]. As can be seen in Figure A-1, Δn_{eff} of the planar-alignment cell is more than twice of a hybrid-alignment cell.
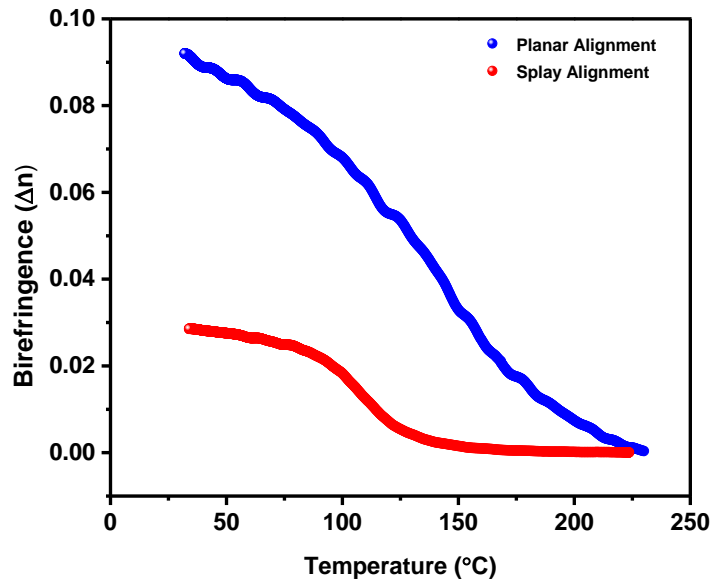

Figure A-1. Variation of birefringence of a planar and a splayed LCE film against temperature.

Measurement of alignment and pretilt angle of mesogens in PDMS-LCE confined systems

The alignments in the intermediate layer and in the pillars were measured by a polarized optical microscope (POM) equipped with a photodetector and a PolScope. For this, LCE precursor was injected into three different cells of 10μm gap, corresponding to the actual thickness of the intermediate layer. The first cell made up of two glass slides, one coated with a thin layer of PDMS and the other coated with a homeotropic alignment agent, SE-1211 (Nissan Chemical Industries, Ltd), was used to determine the anchoring energy of the PDMS. To determine the anchoring energy of the homeotropic LCE, a second cell was made by two glass

slides, one coated with a homeotropic LCE and the other with SE-1211 (Nissan Chemical Industries, Ltd). To show the actual director orientation across the intermediate layer, a third cell was made of two glass slides, one coated with a homeotropic LCE, and the other with a thin PDMS layer.

Polarized optical microscopic studies showed that PDMS promotes homeotropic alignment with no pretilt with respect to the substrate normal. However, we found that the homeotropic side of the backing LCE film has a pretilt angle. This leads to a pretilt at the bottom of the intermediate LCE film, which continuously decreased until the homeotropic alignment was achieved at the PDMS surface. The tilt angle θ_{center} in the center ($h_i/2$) of the third cell was calculated from the known ordinary and extraordinary refractive indices of the material [207], and from the effective birefringence Δn_{eff}. This was obtained from the transmitted intensity of light (I) under monochromatic (λ = 660 nm) illumination with the optical axis of the sample positioned 45° from the two crossed polarizers, using the following equations:

$$I = I_0 \sin^2\left(\frac{\pi \Delta n_{eff} h_i}{\lambda}\right)$$

$$\cos^2 \theta_{center} = \frac{n_0^2}{n_e^2 - n_0^2}\left[\frac{n_e^2}{\left(\Delta n_{eff} + n_0\right)^2} - 1\right]$$

It was found that $\theta_{center} = 8°$. Assuming a linear change of the pretilt angle starting from $0°$ at the PDMS surface, the pretilt angle at the other side of the intermediate LCE film is estimated to be $\theta_{pretilt} = 16°$. To determine the alignment inside the PDMS pillars, we injected the LCE precursor at its nematic temperature into a cell composed of an array PDMS microholes on one side and a homeotropic treated glass on the other side. POM and PoleScope studies showed zero pretilt at the PDMS surface inside and around the holes (Figure A-2). However, the alignment of the mesogens varies when we moved along the radius of the holes to their center. This behavior was consistent with an "escape to the third dimension" configuration [102]. Such a configuration is illustrated in Figure A-3.
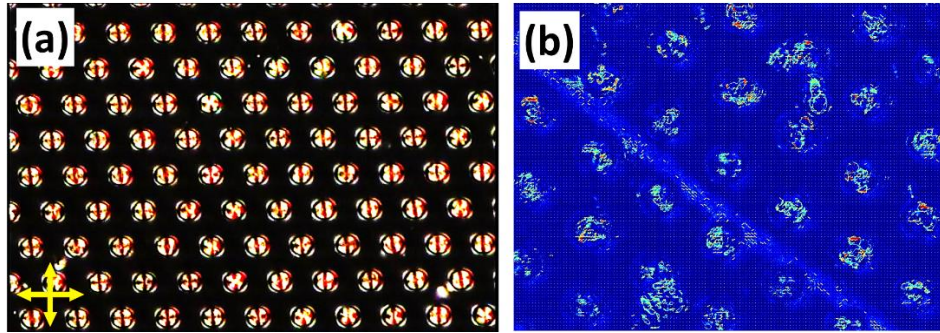
Figure A-2. (a) crossed polarized optical microscopic image of the LCE precursor squeezed between an array of PDMS micro-holes and a homeotropic treated glass; (b) pole-scope image showing homeotropic alignment of mesogens around and on the holes' walls and non-homeotropic alignment inside the holes.
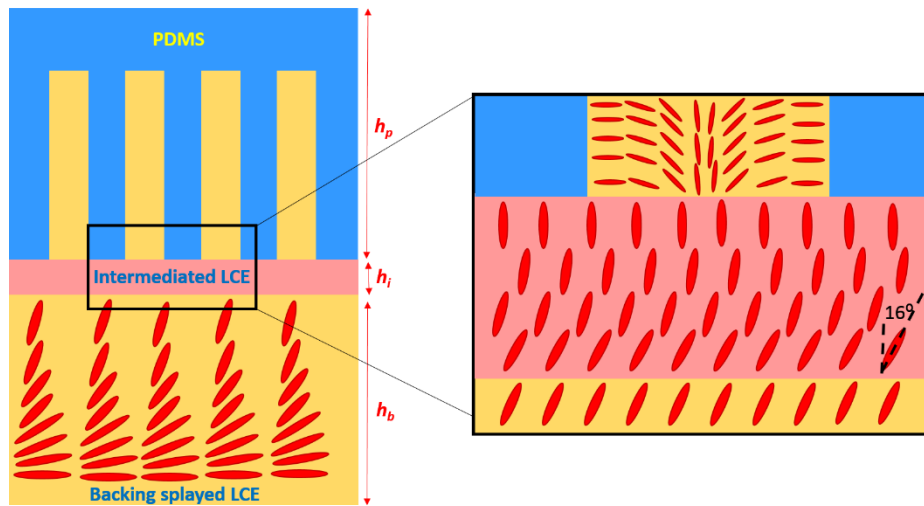

Figure A-3. Sketch of proposed LC director orientation along the thickness of the fabricated structure.